Free Space Optics for Ground-to-Train Communications

Nithin Mohan

A thesis submitted in partial fulfilment of the requirements of Northumbria University,
for the award of Doctor of Philosophy

Research undertaken in the faculty of Engineering and Environment

2022

Declaration

I declare that the work contained in this thesis has not been submitted for any other award. I also confirm that this work fully acknowledges opinions, ideas and contributions from the work of others. Any ethical clearance for the research presented in this commentary has been approved. Approval has been sought and granted through the Researcher's submission to Northumbria University's Ethics Online System on 31/01/2019.

I declare that the Word Count of this Thesis is **32,683** words.

Nithin Mohan

Date: 4/11/2022

Abstract

Development of a high-speed railway network such as High Speed 2 in the UK aims to connect the country and is expected to ferry around 300,000 passengers per day. The ubiquitous use of hand-held devices such as smart-phones and laptops would lead to increased demand in the network bandwidth on board high-speed trains (HSTs). Around 66% of young people consider the availability of high-quality internet services on trains to be very important, and close to a third of them would prefer to travel by train if onboard internet services are improved. In today's hyper-digital era, onboard internet services via WiFi have become less of a handy convenience and more of a necessity for rail passengers at the global level. It is estimated that an 8-carriage train carrying close to 800 passengers in the UK would require 1.2 Gb/s of bandwidth, taking into consideration a monthly mobile data consumption of 20 GB per person. In the UK, CrossCountry and London North-Eastern Railways companies amongst others provide on-board Wi-Fi services, albeit, discouraging consumers from streaming and large file transfers. Additionally, the Wi-Fi user's access is restricted on CrossCountry trains if their data usage exceeds 70 MB and 100 MB in the standard and first-class cabins, respectively. Furthermore, as more and more passengers access WiFi on trains, operators are struggling to provide quality services that are up to the task, thus discouraging people to use trains. To improve the connectivity for rail passengers, network providers need to make fundamental improvements to the infrastructure that serves the areas along each route.

It is widely understood that RF technologies, with their limited spectrum availability, would fail to handle a high volume of information. Therefore, adopting the complementary optical wireless communication, mostly free space optical systems, has been considered for high-speed trains due to its wide spectrum, higher data rates. However, in outdoor environments, one of the key issues in the intensity modulated/direct detection free space optical communication system is the degradation of the links' performance due to the atmospheric conditions such as fog, snow, smoke, and turbulence. Another key challenge in implementation of FSO for ground-to-train communications is providing a large coverage area, which reduces the deployment costs of establishing a base station and provides uninterrupted internet service with negligible handover delay. Handover management is another key challenge faced by ground to train communications. conventional mobility protocols do not guarantee the quality of service during handovers, but rather focus on maintaining IP session connectivity.

To address the challenges mentioned above, this work proposes, firstly, a coverage model for ground-to-train communication we developed the concept of sectorised base station for ground to train communication spanning a coverage length of 210m and provide an architecture for relayed FSO communication between base stations to minimise handover latency. Secondly, we analysed the performance of polar codes under the effect of weak turbulence to determine the optimum code-rate to achieve a bit error rate (BER) of 10-9. Considering the successive cancellation decoder for scintillation

indices of 0.12, 02 and 0.33 the optimum code rate was found to be 0.6, 0.33 and 0.2 respectively, for a confidence limit of 95% using Monte-Carlo simulations. Lastly, a dedicated software-defined-network (SDN)-based mobility architecture has been developed for handover management in ground-to-train (G2T) communication. An FSO experimental testbed was designed using off-the-shelf components which includes Raspberry-Pis to test the performance of the protocol. The results showed that the proposed scheme offered seamless handover with an average data transfer and throughput of 256 Mbps, respectively dropping down to 196 Mbps during the handover time.

Acknowledgements

This research was carried out in the Optical Communications Research Group (OCRG) at Northumbria University. This work is supported by Intensive Industrial Innovation Program Northeast UK (IIIP UK) and is part funded by the European Regional Development Fund (ERDF) of which both are gratefully acknowledged.

I would like to thank the head of OCRG, Prof. Ghassemlooy for providing constant support and guidance during my PhD studies. I am fortunate to have been given the opportunity to perform research at OCRG for which I am forever indebted to Prof. Ghassemlooy. I would also take this opportunity to thank my good friend and colleague Fary Ghassemlooy for his constant care and support during the pandemic. During my most vulnerable time Fary was a source of encouragement, enthusiasm, and positivity. Thank you for being there, Fary.

I would like to extend my eternal gratitude towards Dr Mojitaba Mansour Abadi for his help and advice throughout my studies, without whom FSO would mean Flax Seed Oil instead of Free Space Optics to me. Special thanks to Dr Eamon Scullion and Dr Robert Wickes to whom I am eternally grateful as I find myself in this truly extraordinary position. I would like to thank the technical and academic staff at Northumbria University for lending a helping hand from time to time.

I am grateful to Dr Sujan Rajbhandari and Dr Bo Tan for encouraging me to pursue doctoral studies.

I would like to thank my colleagues past and present at OCRG whose esteemed company made my time at Newcastle wonderfully less miserable. We have been through chaotic times and your company made it more bearable.

Thank you to my friends in Newcastle. I am lucky to have met you crazy lot. Your wisdom has no bounds, and your stupidity is infinite which made your company elite.

Special thanks to my parents who have had faith in me more than myself. Without you, I wouldn't be here. Without you, I am nothing.

Finally, I would like to pat myself on the back to have come this far. Thank you for never giving up. It's a bittersweet moment as my time as a student has come to an end.

Newcastle holds a special place in my heart. Thank you for the memories, Newcastle.

Table of contents

List of figures

List of tables

Glossary of Abbreviations

DCMS	Department of Digital, Culture, Media and Sport
mmW	Millimetre Wave
RF	Radio Frequency
WLANs	Wireless Local Area Networks
OWC	Optical Wireless Communication
FSO	Free Space Optics
BER	Bit Error Rate
NEP	Noise Equivalent Power
G2T	Ground-to-Train
Tx	Transmitter
FEC	Forward Error Correction
CSI	Channel State Information
QoS	Quality of Service
Rx	Receiver
OOK	On-Off Keying
LLR	Log-Likelihood Ratio
NEC	Nippon Electric Company
MLCD	Mars Laser Communication Demonstration
SILEX	Semiconductor Laser intersatellite link experiment
LOS	Line of Sight
WPAN	Wireless Personal Area Network
HDTV	High-definition television
IM	Intensity modulation
VCSEL	Vertical Cavity Surface Emitting Laser
FP	Fabry-Perot
DFB	Distributed Feedback Lasers
EDFA	Erbium doped fibre amplifier
CDRH	Centre for Devices and Radiological Health
FDA	Food and Drug Administration
IEC	International Electrotechnical Commission
ANSI	American National Standards Institute
CENELEC	European Committee for Electrotechnical Standardization

LIA	Laser Institute of America
AEL	Accessible Emission Limit
Si	Silicon
APD	Avalanche Photodetector
WDM	Wavelength-division multiplexing
LD	Laser Diode
InP	Indium Phosphide
GaAs	Gallium Arsenide
Ge	Germanium
OBPF	Optical Bandpass Filter
FOV	Field of View
PSD	Power Spectral Density
RIN	Relative Intensity Noise
sCI	Specific Climate Impact
BIA	Broadband Internet Access
VoIP	Voice over Internet Protocol
LCX	Leaky Coaxial Cable
TAT	Train Access Terminal
MHN	Mobile Hot-Spot Network
MTE	Mobile Terminal Equipment
RoF	Radio Over Fibre
BS	Base Station
ATP	Acquisition Tracking and Pointing
PD	Photodetector
T2G	Train to Ground
MMF	Multimode Fibre
EGC	Equal Gain Combining
NA	Numerical Aperture
LDPC	Low Density Parity Check
GG	Gamma-Gamma
CV-MDCA	Vision-Based Multi-Domain Adjustment
CQI	Channel Quality Index
MIMO	Multiple Input Multiple Output
SC	Successive Cancellation
SCL	Successive Cancellation List
BEC	Binary Erasure Channel

SDR	Software Defined Radio
USRP	Universal Software Radio Peripheral
IP	Internet Protocol
QPD	Quadrant Photodetector
MR	Mobile Router
HA	Home Agent
FA	Foreign Agent
OF	Openflow
FE	Flow Entry
SDNC	Software Defined Network Controller
OvS	Open vSwitch
SFP	Small Form Factor
API	Application Programming Interface
AOAF	All-Optical Amplify and Forward
OEO	Optical-Electrical-Optical
NBI	Northbound Interface
CDPI	Control to Data-Plane Interface

Glossary of Symbols

$\tau(\lambda, L)$	Transmittance of the atmosphere
$\Upsilon_T(\lambda)$	attenuation extinction coefficient (m^{-1})
$\alpha_m(\lambda)$	Molecular absorption
$\beta_m(\lambda)$	Molecular Scattering
$\alpha_a(\lambda)$	aerosol absorption
$\beta_a(\lambda)$	aerosol scattering
x_0	Size parameter
N_p	Number of particles per unit volume along the propagation path
A_p	cross-sectional area of scattering
Q_d	Mie scattering efficiency
ń	real part of the complex refractive index
V	Visibility in km
λ	Wavelength in nm
n_{as}	Refractive index of atmosphere
T_e	Atmospheric temperature in K
P_{as}	Pressure in millibar
n_0	Refractive index under no turbulence
n_1	Refractive index under turbulence
C_n^2	Refractive index structure parameter
C_T^2	Temperature structure parameter
$\vec{E}$.	Electric field
k	Wave number
Ψ(r)	Gaussian complex variable
Φ	Phase of the electric field.
χ	Gaussian distributed amplitude fluctuation
S	Gaussian distributed phase fluctuation
σ_χ^2	Log filed amplitude variance
σ_l^2	Log amplitude variance
σ_N^2	Normalised variance of fluctuation
R_F	Fresnel zone
$K_n(\cdot)$	Bessel function of the 2nd kind and of order *n*
α_t	Effective number of large-scale eddies

β_t	Effective number of small-scale eddies
M	APD responsivity
R	Photodetector responsivity
P_r	Average power on detector
η_{qe}	Quantum efficiency
q	Electron charge in coloumb
h	Plank's Constant
c	Speed of light in m/s
$P(t)$	Instantaneous incident power on photodetector
$I(t)$	Instantaneous photodetector current.
$\sigma^2_{q-\mathrm{pin}}$	Photon fluctuation noise for PIN
$\sigma^2_{q-\mathrm{apd}}$	Photon fluctuation noise for APD
$\langle g^2 \rangle$	Mean square current gain
σ^2_{db}	Dark current bulk
σ^2_{ds}	Surface leakage dark current
Ω	Radiating solid angle of the optical source
$N(\lambda)$	Spectral radiance of sky
$W(\lambda)$	Spectral radiance of sun.
σ^2_{bg}	Noise variance due to background radiation
κ	Boltzmann Constant
$\sigma^2_{\mathrm{th-D}}$	Thermal noise for direct detection systems
σ^2_{in}	Intensity noise variance
σ_I^2	Scintillation Index
P_e	Average BER for log-normal turbulence
$\mathbf{G_N}$	Transformation matrix
PM_{i_l}	Path metric for L-codeword
α	Log likelihood ratio
P_{rx}	Received Power
L_{atm}	Atmospheric losses in dB
h_g	Geometric loss in dB
L_{misc}	Miscellaneous losses in dB
Φ	Offset Angle
δ	Tilt Angle
θ_L	Incident angle of light from the receiver lens onto the fibre

Δq	Vertical offset of lens focal point
β	Hard decision estimates
N_{bits}	Number of bits transmitted for a given confidence level
d_{rx}	Tx Aperture diameter
d_{tx}	Rx Aperture diameter
L_M	Link margin
$B_{\text{rx-t\_i+j}}$	Received bits at time $t_{\text{i+j}}$

Chapter 1: Introduction

1.1 Introduction

At present, 63% of the population worldwide, which translates to 5 billion people consume the internet of which 4.56 billion are social media users. It is estimated that this number would reach 5.3 billion by 2023. According to the Cisco annual internet report, video streaming services, ultra-high-definition virtual reality among other applications would result in a considerable increase in the bandwidth demand in the near future [1]. The pervasive use of hand-held devices such as smartphones and tablets means that the end-users expect to be provided with high-speed internet services everywhere, especially while travelling. A poll carried out by evo-rail a UK-based rail technology company, found that 65% of the people between the ages 18 to 34 considered having good quality internet on trains important and a third of young people would potentially consider travelling in trains if the internet connectivity were improved [105].

In the UK, CrossCountry and London North-Eastern Railways companies amongst others provide on-board Wi-Fi services, albeit, discouraging consumers from streaming and large file transfers. Additionally, the Wi-Fi user's access is restricted on CrossCountry trains if their data usage exceeds 70 MB and 100 MB in the standard and first-class cabins, respectively [2]. The Office of Communications, UK's Communication Regulator, published a report that advised the Department of Digital, Culture, Media and Sport (DCMS) on the options for delivering mobile connectivity by developing trackside infrastructure which DCMS recognised as the most effective solution for offering high quality internet service within UK's mainline railways. The Ofcom report projected a 1.2 Gbit/s of bandwidth requirement taking into consideration a monthly mobile data consumption of 20 GB per person and 2.4 Gbit/s considering 40 Gb monthly data consumption for 2025 [3]. Ofcom identified the millimeter Wave (mmW) technology, particularly the 26 GHz band to be able to provide the gigabit capacity. Although, this band could be used for 5G mobile applications and might coexist with the rail connectivity solutions. However, the rail connectivity solutions would have a high degree of directionality and the rail corridors are geographically separate and would, therefore have a limited impact with other 5G applications [3].

There is a growing demand for the access to the high-speed wireless network by the end users when they are on the move i.e., when using trains, buses, ships, etc. At present, the limited Radio Frequency (RF)-based wireless network is provided by the train operator is at low data rates when the train is on the move. Although RF-based communication is a promising technology for fixed wireless local area networks (WLANs), its effectiveness is limited when used in trains thus offering very limited connection capabilities. Differing life cycles between communication technology (3-5 years) and railways infrastructure (15-20 years) make it infeasible to replace the communication infrastructure frequently. It is widely understood that RF technologies, with their limited spectrum availability, would

fail to handle a high volume of information [4]. Therefore, adopting optical wireless communication (OWC) as complementary to RF, and more specifically free space optic (FSO) systems, has been considered in this work for high-speed trains due to its wide spectrum, higher data rates, and lower energy usage (i.e., a green technology). For a truly office-to-office network capabilities offered to commuters while travelling by trains, the system can benefit from a combination of FSO and visible light communication that would be linked to the existing mobile base station (BS) or to the optical fibre backbone network.

This work proposes, firstly, a coverage model for ground-to-train communication we developed the concept of sectorised base station for ground to train communication spanning a coverage length of 210m and provide an architecture for relayed FSO communication between base stations to minimise handover latency. Secondly, we analysed the performance of polar codes under the effect of weak turbulence to determine the optimum code-rate to achieve a bit error rate (BER) of 10^{-9}. Considering the successive cancellation decoder for scintillation indices of 0.12, 02 and 0.33 the optimum code rate was found to be 0.6, 0.33 and 0.2 respectively, for a confidence limit of 95% using Monte-Carlo simulations. Lastly, a dedicated software-defined-network (SDN)-based mobility architecture has been developed for handover management in ground-to-train (G2T) communication. An FSO experimental testbed was designed using off-the-shelf components which includes Raspberry-Pis to test the performance of the protocol. The results showed that the proposed scheme offered seamless handover with an average data transfer and throughput of 256 Mbps, respectively dropping down to 196 Mbps during the handover time.

1.2 Problem Statement

1.2.1 Base Station Coverage Planning

The key challenge in developing trackside infrastructure to enable train-trackside communication is to plan the placement of BSs along to maximise the coverage area of each BS thereby minimising their installation, which is costly. Consider a case where the BS's coverage area is small, i.e., coverage a short section of the train track, and to cover a larger area more BSs would be required to be deployed, which will lead to increased installation costs [4]. Analytical models presented in [5-7] employed a single-beam laser system with larger divergence angle to cover a long distance up to 500m. Note that, larger divergence angles results in higher geometric losses, thus leading to non-reliable communication link between the train and BSs or even worse, may lose connectivity during handing over between BSs and the train.

This research work, addresses the shortcomings of the previous analytical model and has proposed a FSO communication architecture for G2T communications, see the details in Chapter 3.

1.2.2 Turbulence Mitigation using Forward Error Correction

Optical beams propagating through free space experience absorption, scattering caused by smoke, fog, aerosols and dust, and scintillation caused by turbulence-induced fading thus resulting in increased BER, shorter link range, temporary, and complete link degradation. Scintillation causes random fluctuations in both the phase and intensity of irradiance of the optical beam and is a critical factor in ascertaining the performance of an OWC system. Several mitigation techniques such as aperture averaging [8–10], spatial diversity [11, 12], relay-assisted communication [13, 14], adaptive optics [15], and coding [16] have been proposed and investigated in the literature. However, these schemes have issues such as synchronisation, processing complexity, and high implementation costs.

The free space channel can be considered as quasi-static, where the transmitter (Tx) parameters such as the power and code-rate of forward error correction (FEC) codes could be changed in accordance with the channel state information (CSI), thus improving the quality of the FSO link. This presents an opportunity for adaptive coding schemes to be employed in FSO systems. In this work, an in-depth literature review is carried out to understand turbulence models, encoding and decoding algorithms for polar codes. Optimum code rates under turbulence are determined, which can be used to adaptively switch between different code rates to maintain the quality of service (QoS) of the link. In this research the optimum code rates for polar codes are determined under weak turbulence regime, which is outlined in detailed in Chapter 4.

1.2.3 Handover Mechanism

The train-to-trackside architecture envisages a network architecture as shown in Fig. 1-1 (a), where the signal is tapped from the backbone network via an access router serving a group of base stations on the ground connected to it. The network configuration inside the train consists of a mobile router connected to the transceiver. The mobile router serves the passengers through one of the several Wi-fi access points distributed throughout the train. A high-speed train travelling from BS 2 to BS 3 experiences a link-layer handover and while travelling from BS 3 to BS 4 the train experiences the network layer handover [17].

During link-layer handover the train attempts to establish a physical link to the succeeding base station. Once the link is established, the mobile router sends a router solicitation message to the base station and the base station replies with a router advertisement message signifying the end of link layer handover as portrayed in Fig. 1-1(b). In the case of network layer handover, the MR sends a binding

update message to the home agent, which in turn returns a binding acknowledgement message signifying the network layer handover. These exchange of solicitation and acknowledgement messages adds to the latency of the overall system. Eliminating these messages could result in a seamless handover between base stations by reducing the handover delay in the network layer. A handover scheme based on software-defined network is designed and implemented to provide seamless handover as outlined in Chapter 5.

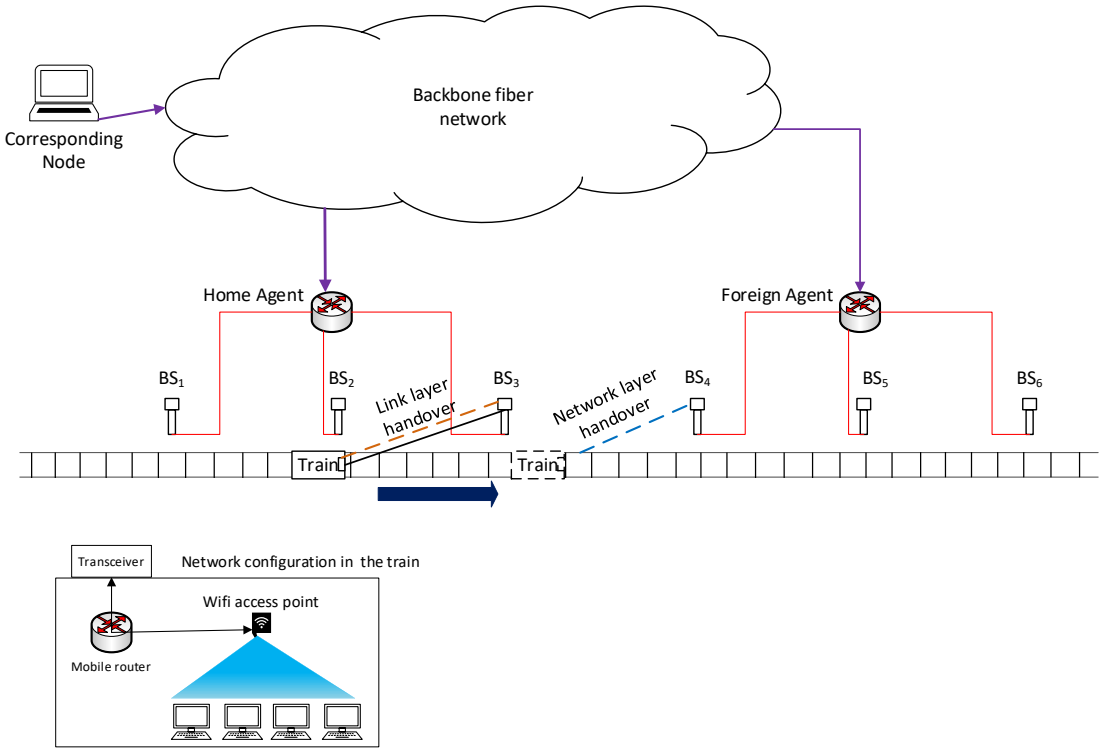

(a)

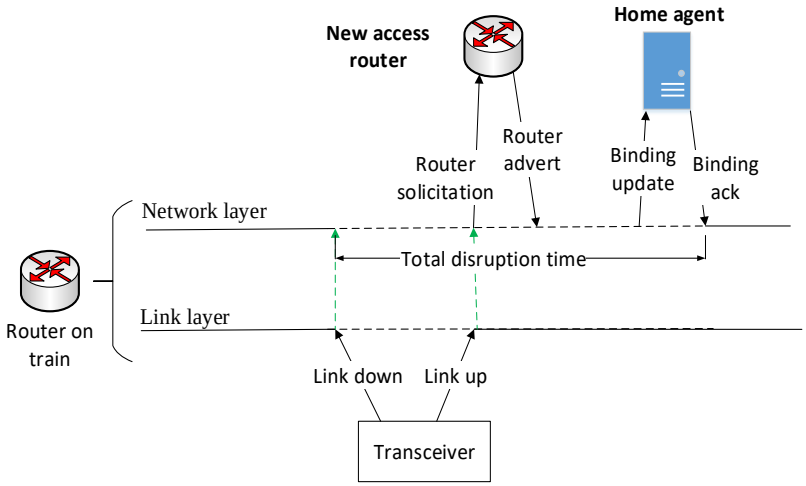

(b)

Fig. 1-1 Network architecture depicting: (a) train-trackside commnunication, and (b) handover procedure

.

1.3 Aim and Objectives

This research aims to propose a physical and network layer architecture for train-to-ground T2G) communication.

The objectives of the research are outlined below:

- To carry out in-depth literature review of FSO communication, relayed FSO, and network protocols and design coverage models for G2T communications to enable seamless handovers between base stations using numerical simulations.
- In-depth literature review of forward error correcting codes with particular focus on polar codes. Evaluating the performance of polar codes in weak turbulence scheme using Monte-Carlo simulation.
- Given that the train takes a pre-determined route to reach its destination, it would be prudent to design a network protocol to minimise the handover latency. To design and implement a protocol for reducing the handover delay in the network layer. This includes design of testbed using off-the-shelf components to validate the protocol design.

1.4 Thesis Contributions

The contribution of this thesis is summarised below:

- Chapter 3 proposes a sectorised multi-beam coverage model with a smaller divergence angle to reduce the impact of geometric losses in the system and proposes two receiver (Rx) architectures for the deployment on the train. In addition to geometric losses, the atmospheric attenuation is taken into consideration for the FSO link. The performance of the G2T communication system in terms of the BER is evaluated under weak turbulence conditions via numerical simulation. The results of this chapter have been published in IET Optoelectronics journal, [J1]
- Chapter 4 investigates the FSO system with polar codes and analyses its performance by determining the optimum code-rate required to achieve a BER of 10^{-9} under weak turbulence using Monte-Carlo simulations for the scintillation indices of 0.12, 0.2, and 0.31. The results of this chapter have been published in IET Optoelectronics journal, [J2].
- Chapter 5 proposes a SDN-based mobility architecture for the handover management in train-trackside communications. A dedicated experimental SDN-based FSO testbed using the off-the-shelf components is designed and implemented to evaluate the system performance in terms

of the data throughput and the packet loss while handover is performed. The results of this Chapter have been submitted to IET Networks journal [J3].

1.5 List of publications

[J1] N. Mohan, M. Abadi, Z. Ghassemlooy, S. Zvanovec, R. Hudson and M. Bhatnagar, "Sectorised base stations for FSO ground-to-train communications", IET Optoelectronics, vol. 14, no. 5, pp. 312-318, 2020. Available: 10.1049/iet-opt.2019.0155.

[J2] Z. Htay, Z. Ghassemlooy, M. M. Abadi, A. Burton, N. Mohan and S. Zvanovec, "Performance Analysis and Software-Defined Implementation of Real-Time MIMO FSO With Adaptive Switching in GNU Radio Platform," in IEEE Access, vol. 9, pp. 92168-92177, 2021, doi: 10.1109/ACCESS.2021.3092968.

[J3] N. Mohan, Z. Ghassemlooy, E. Li, M. M. Abadi, S. Zvanovec, R. Hudson, and Z. Htay, "The BER performance of a FSO system with polar codes under weak turbulence," IET Optoelectronics, vol. 16, no. 2, pp. 72–80, 2021.

[J4] N. Mohan, Z. Ghassemlooy, S. Zvanovec, and M.A. Khalighi, T. Kamalakis "SDN-based Mobility Architecture for the FSO Train-Trackside Communication", submitted to IET Networks on 29th July 2022

[C1] M. M. Abadi, Z. Ghassemlooy, N. Mohan, S. Zvanovec, M. R. Bhatnagar and R. Hudson, "Implementation and Evaluation of a Gigabit Ethernet FSO Link for 'The Last Metre and Last Mile Access Network'," 2019 IEEE International Conference on Communications Workshops (ICC Workshops), 2019, pp. 1-6, doi: 10.1109/ICCW.2019.8757150.

[C2] Z. Htay, N. Mohan, M. M. Abadi, Z. Ghassemlooy, A. Burton and S. Zvanovec, "Implementation and Evaluation of a 10 Gbps Real-time FSO Link," 2020 3rd West Asian Symposium on Optical and Millimeter-wave Wireless Communication (WASOWC), 2020, pp. 1-7, doi: 10.1109/WASOWC49739.2020.9410045.

[C3] N. Mohan, Z. Ghassemlooy, H. A. Rahman and M. A. Khalighi, "Software-Defined Networking for Free Space Optical Communications," 2022 13th International Symposium on Communication Systems, Networks and Digital Signal Processing (CSNDSP), 2022, pp. 235-239, doi: 10.1109/CSNDSP54353.2022.9908018.

[C4] N. Mohan, Z. Ghassemlooy, S. Zvanovec, M. M. Abadi, R. Hudson and M. R. Bhatnagar, "Relayed FSO Links for Ground-to-Train Communications," 2020 12th International Symposium on Communication Systems, Networks and Digital Signal Processing (CSNDSP), 2020, pp. 1-6, doi: 10.1109/CSNDSP49049.2020.9249640.

1.6 Organisation of the Thesis

The thesis is composed of six chapters as outlined below:

1. Chapter 1 introduces the rising demand for internet on trains, restrictions imposed on the consumption of data onboard trains in the UK, and the challenges faced by RF technologies. Section 1.2 outlines the challenges of providing high-speed ground to train communication, whereas Section 1.3 provides the aims of the research. Sections 1.4 and 1.5 outline the list of publications and the contributions made to the areas area, respectively.

2. Chapter 2 provides and overview of free space optical communications describing the fundamentals of optical wireless communications which includes the Tx, atmospheric channel, and the receiver in the context of FSO.

3. Chapter 3 describes sectorised BS coverage model for G2T communication. Section 3.1 provides a brief introduction to coverage models employed in the literature, Section 3.2 describes the system model and the power budget analysis, Section 3.3 describes duplex communication between the BS and the train, and Section 3.4 describes the results of the performance evaluation of the system by numerical simulations. The results of this chapter have been published in IET Optoelectronics journal.

4. Chapter 4 determines the optimum code rate for polar codes in weak turbulence. Sections 4.3 and 4.4 explain polar encoding and decoding schemes, respectively. Section 4.4 derives and approximates the log-likelihood ratio for the on-off keying (OOK) modulation scheme, and lastly, Sections 4.5 and 4.6 describe the system model and the results, respectively. The results of this chapter have been published in IET Optoelectronics journal.

5. Chapter 5 proposes a mobility architecture using the SDN concept to reduce the handover delay in the network layer. Sections 5.2 and 5.3 describe the physical and network layer architecture, respectively. Section 5.4 describes the experimental SDN testbed and the results in terms of the packet loss and the link throughput. The results of this chapter have been submitted to IET Networks journal.
6. Chapter 6 provides the conclusion of the thesis and recommendation for future directions of this research.

Chapter 2: Fundamentals of Free Space Optical Communications

2.1 Introduction to Optical Wireless Communication

OWC is the transmission of optical carriers between visible to ultraviolet spectral band in outdoor or indoor environment. Historically, the Greeks and Romans used fire torches as beacons to signal ships around 800 BC. Smoke was used by native Americans for signalling purposes around 150 BC. The semaphore telegraphy invented by the French in the 18th century was used to signal ships via flags or lights [5]. Although the aforementioned examples employed light as a form of visual communication, optical communication in its true sense was demonstrated by Alexander Graham Bell in 1880 through his photophone experiment. In the experiment Bell modulated sunlight with voice signal, transmitted it at 200m, and received the incoming signal using a parabolic mirror with a selenium cell at its focus. The experiment wasn't successful due sporadic intensity of sunlight and the crudity of the device [6].

MIT Lincoln labs in 1962 developed an OWC link using light emitting GaAs diode or LEDs which transmitted television signals over 30 miles. The most notable development in OWC was carried out by Nippon electric company (NEC) in 1970 established a full-duplex 0.632 μm wavelength He-Ne laser FSO connection from Yokohama till Tamagawa (14 km) which handled commercial traffic [7]. Further developments in OWC lead to deep space communication deployment in ESA and NASA programmes such as Mars laser communication demonstration (MLCD) and semiconductor Laser intersatellite link experiment (SILEX). Recently, NASA launched the Laser communication relay demonstration (LCRD) which aims to act as a relay node for future missions which would send data to Earth via the LCRD. The LCRD aims to provide 1.2 Gpbs downlink data speed over optical links [8]. Although OWC being technologically mature, was experiencing slow penetration in the commercial market due to the following reasons [5]:

- The existing communication systems fulfilled the demands of the consumer.
- Atmospheric effects on OWC would hamper the reliability of the system.
- Pointing, tracking and acquisition systems needed more maturity to be employed in space communication sector.

Increased consumption of data has prompted a demand for high-speed internet services. RF technology could potentially use the 17 GHz and 60 GHz band to satisfy the demand for high-speed data at the cost of installing more expensive components. Also, at higher frequencies, the RF propagation becomes

more line-of-sight (LOS) mimicking the properties of OWC. The RF spectrum below 10 GHz consisting of favourable communication properties suffers from congestion as it is licensed to cellular phone operators, television broadcasts and other commercial companies [9]. Research and development in OWC resulting in successful field trials have witnessed a renewed commercial interest. A 10 Gbps OWC system was made available commercially in 2008 making it the fastest commercially available system at the time [1.12fary]. At present, many companies are devloping commercial OWC solutions with Canon (Japan), Cassidian (Germany), fSONA (Canada), GeoDesy (Hungary), Laser ITC (Russia), LightPointe Communications (USA), MRV (USA), Northern Hi-Tec (UK), Novasol (USA), Omnitek (Turkey), Plaintree Systems (Canada), and Wireless Excellence (UK) to mention a few [10].

OWC can be adopted to serve diverse applications including but not limited to optical interconnects, inter-building links and satellite communication. OWC can be categorised as [10]:

- Ultra-short range which includes communication between chips in stacked, multi-chip packages [11-14].
- Short range OWC of which underwater communication [15,16], wireless personal area network (WPAN) and wireless body area network are some of the examples.
- Medium range OWC would consist of vehicle-vehicle, vehicle to infrastructure and WLANs.
- Long range OWC for example inter-building connections.
- Ultra-long OWC of which deep space links and inter-satellite links are some examples.

In this work we have considered long range OWC operating in the near infrared to infrared region of the electromagnetic spectrum also known as FSO. FSO systems are predominantly LOS which operate above the 300 GHz frequency range providing security, high bandwidth, and robustness to electromagnetic interference. Some potential applications of FSO include [10]:

- **Enterprise connectivity:** FSO's ability to interconnect buildings on campuses having disparate network traffic encompassing voice, fax, digital media amongst other network traffic, providing high speed data is considered as an alternative to typical RF connections.
- **Surveillance:** Video surveillance is widely deployed in many commercial sectors involving public safety requires high throughput to support high quality video transmission. FSO technology is considered an alternative to conventional wireless technologies.
- **Cellular backhaul:** Links from mobile switching centres to the base stations were established either by microwave links or wireline connections could implement FSO keeping in view the explosive growth bandwidth-intensive hand-held devices.
- **Disaster recovery:** Emergency situations demand flexibility and quick response. Temporary FSO links can be deployed in cases where conventional technology fails to operate during an emergency. FSO links were set for commercial businesses during 9/11 disaster in the US which left them with no landlines.

- **Security:** Quantum cryptography provides encryption promising a secure system in the case of cryptosystems against the brute-forcing capability of quantum computers. Such systems are employed with the help of FSO links in scenarios where fibre optics is considered infeasible.
- **Broadcasting:** Live events attracting huge viewership that are broadcast from multiple cameras are transmitted to the satellite via the central office from the broadcast vehicle can be facilitated by FSO. High-definition television (HDTV) broadcasts demand high throughput. BBC during the 2010 FIFA world cup had set-up FSO links for ethernet based transport of HDTV between temporary studio locations in Cape town, South Africa.

A typical FSO communication system as depicted in Fig 2-1 comprises of the Tx, the free space channel, and the receiver modules. The description of each module is provided the following sections.

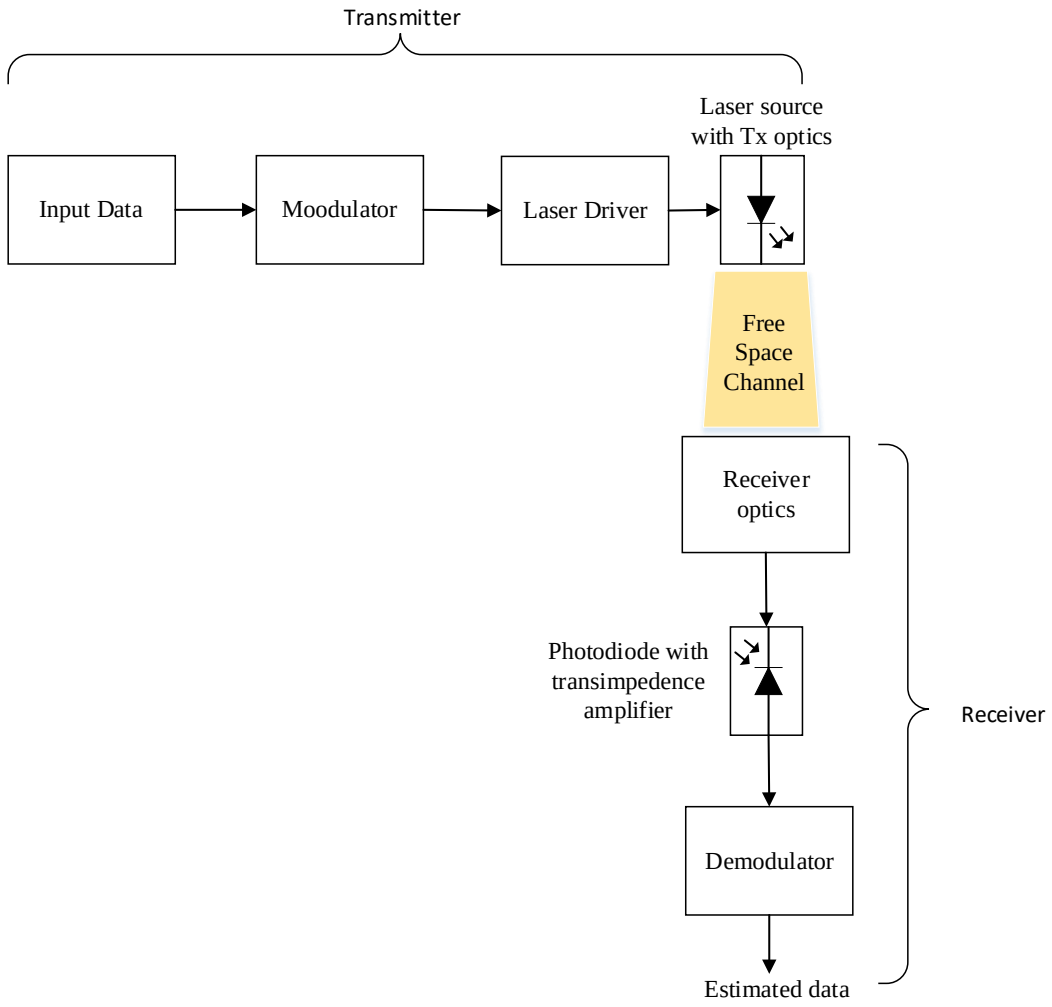

Fig. 2-1 FSO block diagram.

2.2 Transmitter

The key function of the Tx is to modulate the incoming data onto the optical carrier and transmit it through the free space channel. Intensity modulation (IM) is the most common technique used for modulation of the data with respect to the optical irradiance. This is accomplished by either varying the current supplied to the laser by using a laser driver circuit according to the input data which is referred to as direct modulation or by using an external modulator like Mach-Zehnder interferometers which imposes the modulation onto the laser signal after the light has been generated [2.[2]]. The Tx optics collimates the light incoming from the laser in case of direct detection or from the external modulator launching it into the free space channel aiming towards the receiver. Some commonly used laser sources are briefly mentioned in Table 2-1 [17].

Table 2-1 Laser sources

Wavelength	Type	Remarks
850 nm	Vertical Cavity Surface Emitting Laser (VCSEL).	• Low price as compared to many of its alternatives. • High efficiency and low power dissipation. Cooling is not required. • Beam pattern is circular improving coupling efficiency. • Direct modulation ~10 Gbps
~1550 nm	Fabry-Perot (FP) and Distributed Feedback Lasers (DFB)	• High modulation speed. • Compatible with Erbium doped fibre amplifier (EDFA). • High reliability and long-life span.

2.2.1 Average and Peak Output Power

The maximum allowable output power from the laser source is defined as peak power. For most FSO systems, the rating would refer to the transmit power of '1' which is almost twice the average power. Average power is a significant parameter in determining the link margin and for eye-safety classification. FSO communication systems normally employ 8b/10b

coding scheme to approximately maintain equal number of '1s' and '0s' that are transmitted ensuring a 50% duty cycle. Average power is half of the peak power [17].

2.2.2 Beam Propagation Models

An optical beam propagating through the FSO channel diverges with the amount of divergence and the beam footprint playing a key role in the link margin of the system. Majority of the lasers produce a Gaussian beam which is a consequence of the laser resonant cavity. For the case of a diverging beam where the radius of curvature $F_0 > 0$ specifying the beam formation, the irradiance of a Gaussian beam propagating in the z direction with a beam spot radius of W_0 which is measured as the distance between the maximum optical intensity and $1/e^2$ the optical intensity along the radial axis at a distance L along a radial distance r is given as [18]:

$$I^0(r, L) = I_0 \left[\frac{W_0}{W(L)}\right]^2 \exp\left[-\frac{2r^2}{W^2(L)}\right], \tag{2.1}$$

where, $I_0 = I^0(0,0)$ is the Tx output radiance at the centre line of the beam and the ^{0} denotes the irradiance in free space, W_0 is the beam spot radius, $W(L)$ is the beam waist at a distance of L as shown in Fig 2-2.

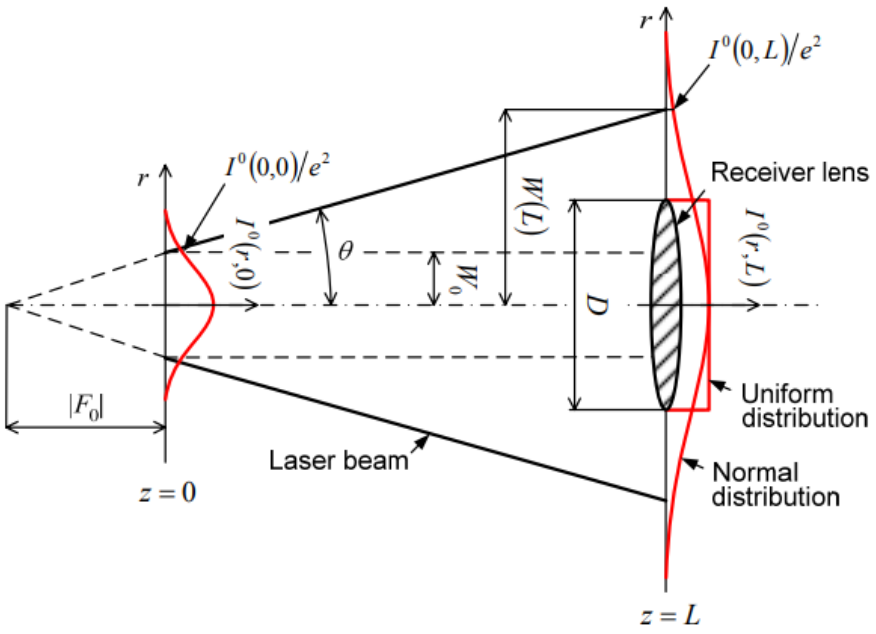

Fig. 2-2 Gaussian beam parameters [18]

Power incident on a circular aperture with diameter *D* placed at a distance *L* from the Tx is given by [18]:

$$P(D,L) = P_0\left[1 - \exp\left(-\frac{D^2}{2W^2(L)}\right)\right]. \quad (2.2)$$

Single mode lasers or lasers coupled with single mode fibre would produce Gaussian beam profile as these sources exhibit point-source spatial qualities.

2.2.3 Laser safety

The topic of laser safety is essential. The potential exposure of the eye or skin to the beam is the main cause of concern for safety. High-powered laser beams can harm skin, but eye injuries are more dangerous due to the eye's capacity to concentrate optical energy by focusing light. Generally speaking, any laser that is deemed "eye-safe" is likewise deemed "skin-safe." Similar to sunlight, laser light travels in parallel rays, which the eye concentrates to a point on the retina, the layer of cells that respond to light, depending on the wavelength. A laser beam with enough power can harm the eyes, just as looking at the Sun can impair vision.

The wavelength is a significant parameter to be taken into consideration for eye safety because only certain wavelengths—roughly 0.4 to 1.4 m—are focused by the eye onto the retina. Other wavelengths are absorbed by the cornea (the front part of the eye) before the energy is concentrated onto the retina. As shown in Fig. 2-3 the wavelength affects the absorption of the eye. The absorption coefficient of the cornea for IR radiation is much higher for longer wavelengths (>1.4 m) than for shorter wavelengths. As a result, damage from UV and visible radiation from sunlight is more likely than damage from longer wavelengths in the IR spectrum [5].

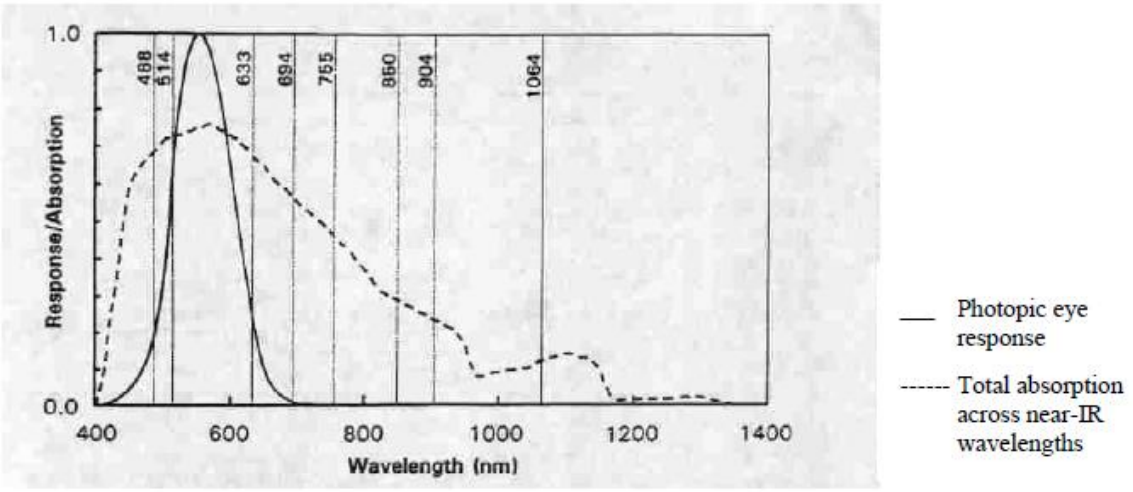

Fig. 2-3 Absorbtion of the human eye at various wavelengths[5].

2.2.4 Laser Safety Standards

Many countries have created or adopted laser safety regulations that apply to all laser products sold within their borders. These safety standards are divided into two categories: those targeting the safety of laser equipment and those targeting the safe use of lasers. Furthermore, some entities have the authority to create legal standards, whereas others establish laser safety standards and guidelines that are not legally enforceable. Laser safety standards, in general, include provisions for automatic or manual safety controls, warning labels and signs, training for operation, maintenance, and service, and the use of protective equipment. The following is a list of the major laser safety standards organisations [5].

Center for Devices and Radiological Health (CDRH): CDRH is an agency within the United States (U.S.) Food and Drug Administration (FDA). It establishes regulatory standards for lasers and laser equipment that are enforceable by law (21 CFR 1040).

International Electrotechnical Commission (IEC): IEC publishes international standards related to all electrical equipment, including lasers and laser equipment (IEC60825-1). These standards are not automatically enforceable by law, and the decision to adopt and enforce IEC standards is at the discretion of individual countries.

American National Standards Institute (ANSI): ANSI is a U.S. organization that publishes standards for laser use (ANSI Z136.1). ANSI standards are not enforceable by law but do form the basis for the U.S. Occupational Safety and Health Administration (OSHA) legal standards, as well as comparable legal standards that have been adopted by various state regulatory agencies.

European Committee for Electrotechnical Standardization (CENELEC): CENELEC is an organization that establishes electrotechnical standards based on recommendations made by 19 European member nations. CENELEC standards are not directly enforceable by law but, as with IEC standards, are often integrated into the legal requirements developed by individual countries.

Laser Institute of America (LIA): LIA is an organization that promotes the safe use of lasers, provides laser safety information, and sponsors laser conferences, symposia, publications, and training courses.

We have considered the IEC standards to classify lasers depending upon their Accessible Emission Limit (AEL) [5] depicted in table 2-2. AEL is defined as the maximum output laser radiation which a laser emits after its manufacture. The AEL depends on the wavelength, exposure duration and the viewing conditions and specifies the maximum output within each laser class [17].

Table 2-2 Laser Classification

Laser Class	Description
Class 1	Lasers that are safe under reasonably foreseeable conditions of operation, including the use of optical instruments for intra-beam viewing.
Class 1M	Lasers emitting in the wavelength range from 302.5 nm to 4000 nm which are safe under reasonably foreseeable conditions of operation but may be hazardous if the user employs optics within the beam. Two conditions apply: a) for diverging beams if the user places optical components within 100 mm from the source to concentrate (collimate) the beam; or b) for a collimated beam with a diameter larger than 3.5 mm for an exposure time > 10s.
Class 2	• Lasers that emit visible radiation in the wavelength range from 400 nm to 700 nm where eye protection is normally afforded by aversion responses, including the blink reflex. This reaction may be expected to provide adequate protection under reasonably foreseeable conditions of operation including the use of optical instruments for intra-beam viewing.

	• For wavelengths outside the visible spectrum, the AEL of class 2 lasers should be less than class 1 lasers.
Class 2M	• Lasers that emit visible radiation in the wavelength range from 400 nm to 700 nm where eye protection is normally afforded by aversion responses including the blink reflex. However, viewing of the output may be more hazardous if the user employs optics within the beam. Two conditions apply: a) for diverging beams, if the user places optical components within 100 mm from the source to concentrate (collimate) the beam, or b) for diverging beams if the user places optical components within 100 mm from the source to concentrate (collimate) the beam; or b) for a collimated beam with a diameter larger than 3.5 mm for an exposure time > 10s. • For wavelengths outside the visible spectrum, the AEL of class 2 lasers should be less than class 1M lasers.
Class 3R	Lasers that emit in the wavelength range from 302,5 nm to 106 nm where direct intra-beam viewing is potentially hazardous, but the risk is lower than for Class 3B lasers, and fewer manufacturing requirements and control measures for the user apply than for Class 3B lasers. The accessible emission limit is within five times the AEL of Class 2 in the wavelength range from 400 nm to 700 nm and within five times the AEL of Class 1 for other wavelengths.
Class 3B	Lasers that are normally hazardous when direct intra-beam exposure occurs.
Class 4	Lasers that are also capable of producing hazardous diffuse reflections. They may cause skin injuries and could also constitute a fire hazard. Their use requires extreme caution.

2.2.5 Atmospheric Transmission Windows

Only a few experimental systems functions at an IR wavelength of 10,000 nm [17], while the vast majority of commercially accessible FSO systems now operate in the near-IR wavelength range of approximately 750 to 1600 nm. While the physics and transmission qualities of optical energy in the atmosphere remain constant across the visible and near-IR wavelength range, there are a number of considerations that can affect whatever wavelength a design team ultimately settles on [17].

Despite the fact that the atmosphere is regarded to be highly transparent at visible and near-infrared wavelengths, particular wavelengths (or wavelength bands) can undergo intense absorption. In the near-infrared wavelength, absorption occurs predominantly in response to water particles (i.e., moisture), which are present in the atmosphere even during clear weather conditions. The contribution of gas absorption (e.g., COx or NOx) to the overall absorption coefficient is not examined here because gas-specific absorption coefficients are fairly minor compared to water absorption coefficients. However, in the longer IR wavelength range (>2000 nm), the absorption properties of the atmosphere can be dominated by gas absorption. Fig. 2-4 illustrates the absorption of the atmosphere under clear weather conditions (visibility >16 km) for various transmission wavelengths in the near-IR spectral range (between 0.7 and 1.6 m) and was generated using MODTRAN, a programme designed to facilitate the study of the transmission properties of the atmosphere. Within the 700–10,000 nm wavelength range, a number of transmission windows are nearly transparent (i.e., having an attenuation of 0.2 dB/km). The bulk of FSO systems are designed to function in the 780–850 nm and 1520–1600 nm operating windows, which are centred on certain centre wavelengths.

780–850 nm: These wavelengths are suited for FSO operation, and a number of suppliers offer laser sources with greater output in this range. Around 850 nm, components for Txs and detectors that are dependable, affordable, and high performing are easily available and widely utilised in network and transmission equipment. For operation at this wavelength, highly sensitive silicon (Si) avalanche photodiode (APD) detector technology and advanced VCSEL technology can be utilised [17].

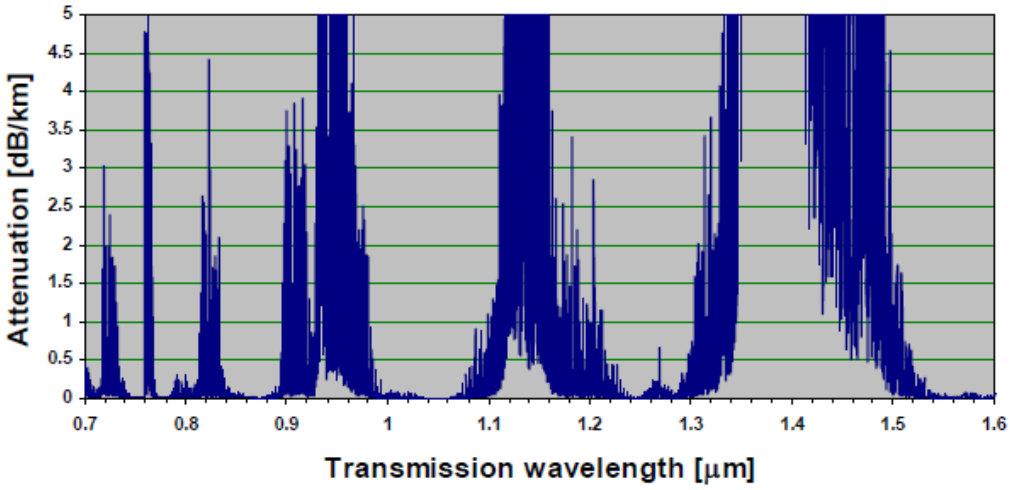

Fig. 2-4 MODTRAN transmission calculation under clear weather conditions [17].

1520–1600 nm: These wavelengths are optimal for free-space transmission, and components for Txs and detectors of the highest quality are widely available. The combination of low attenuation and high component availability at this wavelength makes it possible to create wavelength-division multiplexing (WDM) FSO systems. Nevertheless, components are normally more expensive, and detectors are typically less sensitive and have a smaller reception surface area than Si APD detectors that operate at 850 nm wavelength. However, these wavelengths are also utilised in long-haul fibre systems, and numerous businesses are attempting to reduce the cost and enhance the performance of 1520–1600 nm components. Moreover, these wavelengths are compatible with EDFA technology, which is essential for high-power (>500 mW) and high-data rate (>2.5 Gbit/s) systems. 50–65 times as much power can be transferred at 1520–1600 nm than can be transmitted at 780–850 nm for the same eye safety classification [17].

2.3 Atmospheric Channel

The atmosphere channel is random in nature which impacts the characteristics of the propagating optical beam (laser in the majority of cases), resulting in optical losses and turbulence-induced amplitude and phase fluctuations. Due the random nature of the atmospheric channel's characteristics, its effects can be described statistically. The statistical nature of the atmospheric channel is characterised by a number of models in the literature; these will be examined in this section. Depending on the type of model and its precision, it is possible to estimate the optical irradiance received at the receiver [5].

2.3.1 Atmospheric Channel Loss

Because of absorption and scattering, the optical field that goes through the atmospheric channel gets weaker. Attenuation of the optical signal is caused by the concentrations of matter in the atmosphere, which change over time and space and depend on the weather at the time. For a terrestrial FSO link launches an optical signal through the atmosphere, Beer-law Lambert's says that the irradiance received at a distance *L* from theTx is related to the irradiance is given as [5]:

$$\tau(\lambda, L) = \frac{P_{\mathrm{T}}}{P_{\mathrm{R}}} = \exp[-\Upsilon_T(\lambda)L], \tag{2.3}$$

where $\Upsilon_T(\lambda)$ represents attenuation extinction coefficient (m-^{1}), and $\tau(\lambda, L)$ represents the transmittance of the atmosphere at wavelength λ. $\Upsilon_T(\lambda)$ is dependent on the molecular constituents such as gases and aerosols. The attenuation coefficient is the sum of absorption and scattering coefficients from these molecular constituents which is given as [5]:

$$\Upsilon_{\mathrm{T}}(\lambda) = \alpha_{\mathrm{m}}(\lambda) + \alpha_{\mathrm{a}}(\lambda) + \beta_{\mathrm{m}}(\lambda) + \beta_{\mathrm{a}}(\lambda), \tag{2.4}$$

where $\alpha_{\mathrm{m}}(\lambda)$ and $\beta_{\mathrm{m}}(\lambda)$ represent molecular absorption and scattering respectively and $\alpha_{\mathrm{a}}(\lambda)$ and $\beta_{\mathrm{a}}(\lambda)$ represent aerosol absorption and scattering respectively. Absorption takes place when photons interact with molecules/aerosols present in the atmosphere. In some cases, after the interaction the photons are extinguished generating heat in the process. Absorption is dependent on type of molecules and is wavelength selective [19].

Scattering takes place when photons interact with atmospheric particles such as fog or aerosols which causes a reorganisation of the optical field's angular distribution with or without wavelength modification. Depending on the size parameter $x_0 = \frac{\text{circumference of the particle}}{\lambda}$, scattering is further classified as Rayleigh scattering (for $x_0 << 1$) and Mie scattering (for $x_0 \approx 1$).

2.3.1.1 Rayleigh Scattering

Rayleigh scattering is given by [5]:

$$\beta_{\mathrm{Rayleigh}}(\lambda) = 0.827 N_p A_p^3 \lambda^{-4}, \tag{2.5}$$

where N_p is the number of particles per unit volume along the propagation path and A_p represents the cross-sectional area of scattering.

2.3.1.2 Mie Scattering

Assuming that the scattered light maintains its wavelength as the incident light with multiple scattering effects neglected and the size of the particle is spherical with a complex refractive index, the Mie scattering expression is derived as [5]:

$$\Upsilon_T(\lambda) \approx \beta_a(\lambda) = 10^5 \int_0^\infty Q_d\left(\frac{2\pi r}{\lambda}, ń\right)\pi r^2 n(r)dr, \tag{2.6}$$

where r is the particle (fog, aerosol etc.) radius in centimetres, Q_d is the Mie scattering efficiency, ń is real part of the complex refractive index and $n(r)$ is the volume concentration that is the number of fog particles per unit volume per unit increment in radius. Here, is the specific attenuation $\beta_a(\lambda)$ is measured in dB/km and is calculated by summing up the attenuation effect of all the individual fog droplets present per unit volume per unit increase in radius.

The particles encountered in the atmosphere have various shapes and orientations, making it extremely difficult to apply the theory of Mie scattering to them. The attenuation caused by scattering will henceforth be described using empirical formulas. Frequently, these empirical equations are represented in terms of the vision range V in kilometres. Visibility range is the distance a parallel bright beam must travel through the atmosphere before its intensity falls to 2% of its initial value [135]. It is measured with a device called a transmissiometer, and a prevalent empirical model for Mie scattering is provided by [5]:

$$\beta_a(\lambda) = \frac{3.91}{V}\left(\frac{\lambda}{550}\right)^{-\delta}, \tag{2.6}$$

Where the parameter δ is depends on the scattering particles' size distribution. The parameter δ is calculated by applying the theory proposed by Kruse and Kim, as expressed in equations (2.7) and (2.8) which are derived by fitting the experimental results. In the case of large attenuation values, Kim model is preferred and is given by [5].

$$\delta = \begin{cases} 1.6 & V > 50 \text{ km} \\ 1.3 & 6 \text{ km} < V < 50 \text{ km} \\ 0.16V + 34 & 1 \text{ km} < V < 6 \text{ km} \\ V - 0.5 & 0.5 \text{ km} < V < 1 \text{ km} \\ 0 & V < 0.5 \text{ km} \end{cases} \quad (2.7)$$

Kruse's model is given by:

$$\delta = \begin{cases} 1.6 & V > 50 \text{ km} \\ 1.3 & 6 \text{ km} < V < 50 \text{ km} \\ 0.585V^{1/3} & V < 6 \text{ km} \end{cases} \quad (2.8)$$

Table 2-3 provides the international visibility codes. It can be used as a reference for fog and haze situations FSO system behaviour investigation [20].

Table 2-3 International Visibility Code and Weather Conditions [20]

Weather Conditions	Precipitation (mm/h)		Visibility (m)	Attenuation (dB/km)
Dense Fog			50	315
Thick Fog			200	75
Moderate Fog			500	28.9
Light Fog				
	Storm	100	770	18.3
Very Light Fog			1000	13.8
	Heavy rain	25	1900	6.9
Light Mist			2000	6.6
	Average rain	12.5	2800	4.6
			4000	3.1
Very Light Mist	Light Rain	2.5	5900	2
			10000	1.1

Clear Air	Drizzle	0.25	18100	0.6
Very Clear Air			20000	0.54
			23000	0.47
			50000	0.19

2.4 Atmospheric Turbulence

Because the Earth's surface soaks up solar radiation, the air near the surface is warmer than the air higher up. This layer of warmer air gets less dense and rises, mixing erratically with the cooler air around it. This makes the temperature of the air change randomly [21]. Inhomogeneities caused by turbulence can be seen as discrete cells or eddies of different temperatures that act like refractive prisms of different sizes and indices of refraction. The interaction between the laser beam and the turbulent medium causes random changes in the phase and amplitude of the information-carrying optical beam. This is called "scintillation," and it causes the received optical power to fade, which lowers the system's performance. Turbulence in the atmosphere is divided into regimes based on how much index of refraction variation and inhomogeneities these regimes are weak, moderate, strong, and saturation.

The random fluctuation of the atmospheric refractive index, n, that is caused by turbulence in the atmosphere occurs along the course of the optical field or radiation that is travelling through the atmosphere. This fluctuation in the refractive index is the direct consequence of random differences in the temperature of the atmosphere from one point to another [21]. These seemingly arbitrary shifts in temperature are brought about by changes in the pressure, altitude, and wind speed of the surrounding atmosphere. The smallest of the turbulence eddies are referred to as the inner scale, or l_0, of turbulence, while the largest of the turbulence eddies are referred to as the outer scale, or L_0. l_0 is normally measured in millimetres, while L_0 is typically measured in metres [22, 23]. l_0 is typically measured in the micrometre range. These weak lens-like eddies, which are graphically represented in Fig. 2-5, are the cause of a randomised interference effect that occurs between various parts of the beam that is being propagated, which, in turn, causes the wavefront to become deformed.

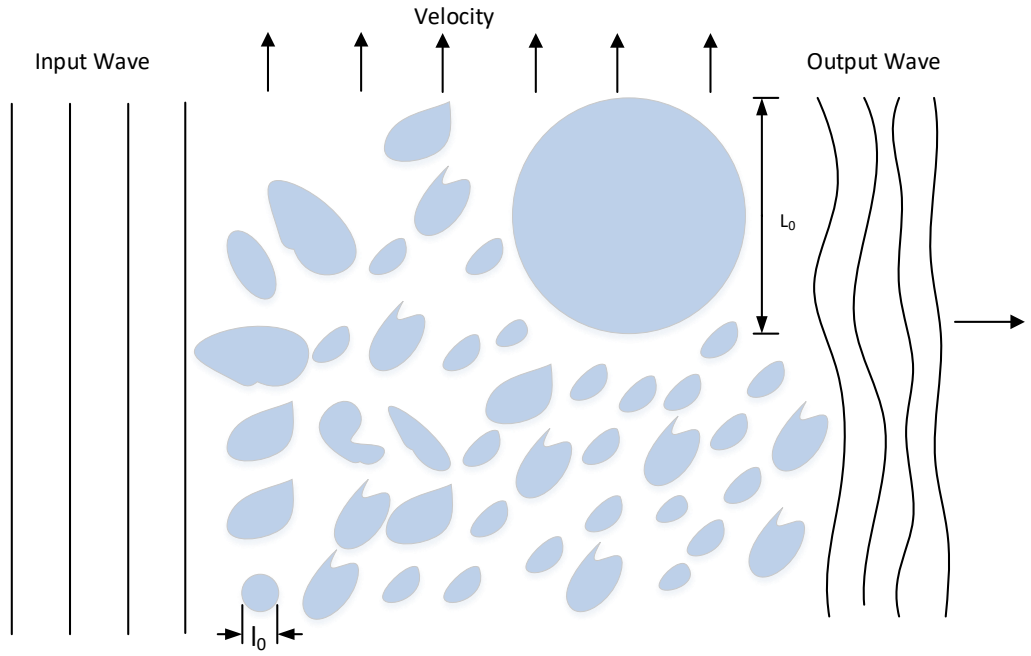

Fig. 2-5 Turbulent eddies in atmospheric channel.

The "Taylor hypothesis" [80], states that the turbulent eddies are fixed or frozen and can only move in their frozen form with the transverse component of the mean local wind, will be followed. This hypothesis states that the turbulent eddies can only move in their frozen form with the mean local wind. [24] According to this idea, the temporal fluctuations in the beam pattern or the statistical features of the beam are brought on by the component of the local wind that is perpendicular to the direction in which the beam is propagating. In addition to this, it has been stated that the temporal coherence time of atmospheric turbulence is of the order of milliseconds [25]. This value is relatively big in comparison to the period of a typical data symbol; hence, the turbulent atmospheric channel can be regarded as a "slow fading channel" because it remains constant during the duration of a data symbol due to the fact that it does not fade.

The relationship between temperature of the atmosphere and its refractive index is given as [26]:

$$n_{\mathrm{as}} = 1 + 77.6(1 + 7.52 \times 10^{-3}\lambda^{-2})\frac{P_{\mathrm{as}}}{T_{\mathrm{e}}} \times 10^{-6}, \qquad (2.9)$$

where n_{as} is the refractive index, T_{e} is temperature in kelvin, P_{as} is pressure in millibar.

The rate of change of the refractive index with respect to channel temperature is represented by [26]:

$$\frac{-\mathrm{d}n_{as}}{\mathrm{d}T_{\mathrm{e}}} = 7.8 \times 10^{-5}\frac{P_{\mathrm{as}}}{T_{\mathrm{e}}^2}. \qquad (2.10)$$

The position and time dependent index of refraction denoted by $n(r,t)$ can be expressed as the sum of its free-space (no turbulence) value n_0, and a turbulence induced random fluctuation component $n_1(r,t)$. Thus [5]:

$$n(r,t) = n_0 + n_1(r,t). \tag{2.11}$$

According to Taylor's 'frozen-flow' hypothesis, the transverse component of the atmospheric wind contributes to the temporal variations of the index of refraction of the channel, therefore, the randomly fluctuating part of equation (2.11) can then be written as [5]:

$$n_1(r,t) = n_1(r - vt) \ , \tag{2.12}$$

where v is the local wind velocity perpendicular to the field direction of travel. The refractive structure parameter C_n^2 is an important parameter in atmospheric turbulence. The value of C_n^2 varies with altitude and a commonly used model to describe it is the Hufnagel-Valley (H-V) model given below as [23]:

$$C_n^2(h) = 0.00594(v/27)^2(10^{-5}h)^{10}\exp(-h/1000) + 2.7 \times 10^{-16}\exp\left(-\frac{h}{1500}\right) + \hat{A}\exp(-h/100), \tag{2.13}$$

where $\hat{A}$ is taken as the nominal value of C_n^2 (0) at the ground in $m^{-2/3}$ and h is the altitude in metres. The value of the index of refraction structure parameter varies with altitude, but for a horizontally propagating field it is usually assumed constant. C_n^2 typically ranges from 10^{-12} $m^{-2/3}$ for strong turbulence to 10^{-17} $m^{-2/3}$ for weak turbulence with a typical average value being 10^{-15} $m^{-2/3}$ [5].

A similar parameter for temperature variations is the temperature structure parameter and it is related to C_n^2 by:

$$C_n^2 = \left(\frac{dn_{as}}{dT_e}\right)^2 C_T^2. \tag{2.14}$$

According to [25], the presence of non-linear mixing of observable quantities, which is fundamental to the process, is the primary cause of the difficulty in mathematically describing turbulent media. This difficulty is primarily due to the fact that turbulent media are by their very nature extremely difficult to

describe. In order to derive formulas for the statistical properties of an optical beam as it travels through a turbulent atmosphere, specifically the pdf and variance, the following simplifying but reasonable assumptions will be employed to reduce the amount of mathematics to a level that is more manageable [25]:

1. The atmosphere acts as a tunnel for the wave that does not dissipate energy as it travels through it. This assumption can be described as follows: in the case that the atmosphere absorbs the wave that is being propagated or the radiation, the amount of heat that is generated is negligible in comparison to the contributions made during the day.

2. The beam's total amount of energy is not diminished as a consequence of the process of dispersion caused by turbulent eddies. Because of this, it is assumed that the mean energy even when there is turbulence present is the same as the mean energy even when there is no turbulence present. This assumption is correct when it comes to both plane and spherical waves. The plane wave is a type of wave that can be applied to laser beams that are travelling over a significant distance [25, 26].

2.4.1 Log Normal Turbulence

An optical beam propagating through turbulent media can be expressed by its electric field $\vec{E}$. The following expression is derived by applying Maxwell's electromagnetic equations to the case of a spatially varying dielectric, such as the atmosphere [5]

$$\nabla^2\vec{E} + k^2 n_{\mathrm{as}}^2\vec{E} + 2\nabla\left[\vec{E}\cdot\vec{\nabla}\ln(n_{\mathrm{as}})\right] = 0, \tag{2.15}$$

where, *k* is the wave number and $\vec{\nabla}$ is the vector gradient operator. $2\nabla\left[\vec{E}\cdot\vec{\nabla}\ln(n_{\mathrm{as}})\right]$ represents wave depolarisation. Under any turbulence regime, the depolarisation term is negligible which is shown experimentally in [27-29]. Therefore, 2.15 reduces to

$$\nabla^2\vec{E} + k^2 n_{as}^2\vec{E} = 0. \tag{2.16}$$

For convenience the position vector shall be depicted as r and $\vec{E}$ is represented as E(r). Tartaski [30] employed Ψ(r), a gaussian complex variable to solve 2.16. Ψ(r) is the natural logarithm of E(r) and is denoted as the Rytov transformation.

$$\Psi(r) = \ln[E(r)]. \tag{2.17}$$

The Rytov method is based on the approximation that the turbulence is weak which is defined as a single scattering process. Using 2.16 and substituting n_0 as 1, 2.17 transforms to [5]:

$$\nabla^2 \Psi + (\nabla\Psi)^2 + k^2\left(1 + n_{as_1}\right)^2 = 0, \tag{2.18}$$

Using the smooth perturbing model from [25], we substitute for $\Psi(r)$ as $\Psi(r) = \Psi_0(r) + \Psi_1(r)$ where, $\Psi_0(r)$ is the free space counterpart and $\Psi_1(r)$ is the turbulence-induced form, in 2.18 to yield:

$$\Psi_1(r) = \ln[E(r)] - \ln[E_0(r)] = \ln\left[\frac{E(r)}{E_0(r)}\right], \tag{2.19}$$

where, $E_0(r)$ and $E(r)$ are given by [5]:

$$E(r) = A(r)\exp(i\Phi(r)), \tag{2.20}$$

$$E_0(r) = A_0(r)\exp(i\Phi_0(r)), \tag{2.21}$$

where, $A_0(r)$, $A(r)$ and Φ, Φ_0 represent the amplitude and phase respectively. The behaviour of the field in weak turbulence can be determined by solving 2.15 using the transformations obtained in 2.17 – 2.21. The turbulence induced field amplitude fluctuation is given by []:

$$\Psi_1(r) = \ln\left[\frac{A(r)}{A_0(r)}\right] + i[\Phi(r) + \Phi_0(r)] = \chi + iS\,. \tag{2.22}$$

Given that $\Psi_1(r)$ is Gaussian, it follows that χ is Gaussian distributed amplitude fluctuation and S is Gaussain distributed phase fluctuations. The probability distribution function of χ is given by:

$$p(\chi) = \frac{1}{\sqrt{2\pi\sigma_\chi^2}} \exp\left\{-\frac{(\chi - E[\chi])^2}{2\sigma_\chi^2}\right\}, \tag{2.23}$$

where, $E[.]$ is the expectation of χ and σ_χ^2 is the log amplitude field variance. σ_χ^2 is related to the refractive structure parameter C_n^2 and the distance L_P the optical wave travels, for a plane wave and is given by [26]:

$$\sigma_\chi^2 = 0.56k^{7/6} \int_0^{L_P} C_n^2(x)(L_P - x)^{5/6}\, dx, \tag{2.24}$$

For a spherical wave, the expression turns to:

$$\sigma_\chi^2 = 0.56k^{7/6} \int_0^{L_P} C_n^2(x)(x/L)^{5/6}(L_P - x)^{5/6}\, dx, \tag{2.25}$$

For a wave propagating in turbulent medium in terrestrial conditions, the C_n^2 is constant. Therefore, the log amplitude variance or the Rytov variance turns to:

$$\sigma_l^2 = 1.23C_n^2 k^{7/6} L_P^{11/6}, \tag{2.27}$$

The optical intensity under turbulent medium is $I = |A(r)|^2$ and under clear medium is $I_0 = |A_0(r)|^2$, therefore the log intensity is given by:

$$l = \log_e \left|\frac{A(r)}{A_0(r)}\right|^2 = 2\chi, \tag{2.28}$$

$$I = I_0 \exp(l), \tag{2.29}$$

The probability density function for the optical irradiance is given by [5]:

$$p(I) = \frac{1}{\sqrt{2\pi\sigma_l^2}}\frac{1}{I}\exp\left\{-\frac{(\ln(I/I_0) - E[l])^2}{2\sigma_l^2}\right\}, I \geq 0, \quad (2.30)$$

Weak turbulence intensity obeys the log-normal statistics. From 2.25 and 2.26 $\sigma_l^2 = 4\sigma_\chi^2$, and given that there is no loss of energy during the scattering process $E[\exp(l)] = \mathrm{E}[I/I_0] = I_0$. Expectation of any real-valued Gaussian random variable z, is given by:

$$E[\exp(az)] = \exp(a\mathrm{E}[z] + 0.5a^2\sigma_z^2), \quad (2.31)$$

Therefore, using 2.31 $E[\exp(l)]$ is expressed as:

$$E[\exp(l)] = \exp(\mathrm{E}[l] + 0.5\sigma_l^2), \quad (2.32)$$

$$1 = \exp(\mathrm{E}[l] + 0.5\sigma_l^2), \quad (2.33)$$

$$\mathrm{E}[l] = -0.5\sigma_l^2). \quad (2.34)$$

The log-normal probability density function for normalised irradiance is shown in Fig. 2-6. As the σ_l^2 is increased the plot shifts to the left with longer tails tending towards infinity.

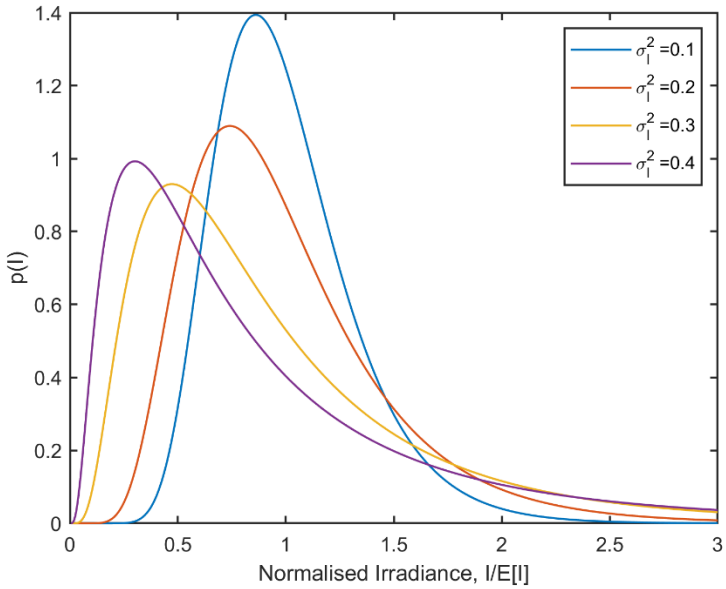

Fig. 2-6 Log-normal probability density function vs normalised irradiance.

The intensity of the turbulence fluctuation σ_I^2 can be determined by the following expressions [31, 5]:

$$\sigma_I^2 = E[I^2] - E[I]^2 = I_0^2\{E[\exp(2l)] - E[\exp(l)]^2\}, \tag{2.35}$$

$$\sigma_I^2 = I_0^2[\exp(\sigma_l^2) - 1], \tag{2.36}$$

$$\sigma_N^2 = \frac{\sigma_I^2}{I_0^2} = \exp(\sigma_l^2) - 1, \tag{2.37}$$

σ_N^2 is the normalised variance of fluctuation intensity also known as scintillation index.

2.4.2 Limit to the Log-Normal Turbulence

The Rytov approximation has been utilised thus far in order to represent the turbulence that occurs in the atmosphere, and the log-normal turbulence model has been derived. According to the Rytov approximation, the Rytov parameter should increase with the index of refraction structural parameter and/or the path length limitlessly. On the other hand, based on the results of experiments that were reported in references [23, 26], this prediction is only accurate in the weak turbulence domain when $\sigma_\chi^2 \leq 0.3$. As the turbulence strength increases beyond the weak regime, due to a combination of

increased path length and/or increased C_n^2, the turbulent eddies cause multiple scatterings that Rytov's approximation does not account for [23, 26]. This is because Rytov's approximation is based on an assumption that the path length and/or C_n^2 remains constant. On the basis of experiments that are reported in References [23, 26], the *S.I.* goes up in a linear fashion with the Rytov parameter when the system is in the weak regime and keeps going up until it reaches a maximum value that is higher than unity. The condition in which S.I. reaches its highest possible value is indicative of the regime with the greatest degree of inhomogeneity or random focusing. The S.I. then begins to diminish as a result of self-interference as a direct result of repeated scattering and gets closer and closer to one as the Rytov parameter gets higher [84]. In contrary to what the Rytov approximation beyond the weak atmospheric domain predicted, this observation came to the opposite conclusion. Multiple scattering effects need to be taken into account when the intensity of air turbulence rises, and log-normal statistics show considerable differences when compared to the experimental data [23, 32].

2.4.3 Gamma-Gamma Turbulence Model

This model was proposed by Andrews et al [23], and it is based on the modulation process. According to this process, the fluctuation of light radiation as it travels through a turbulent atmosphere is comprises of both small-scale (scattering) and large-scale (refraction) effects. The first category takes into account the contributions made by eddies and cells that are smaller than the Fresnel zone $R_F = (L_P/k)^{1/2}$ or the coherence radius ρ_0, whichever value is lower. Large-scale fluctuations, on the other hand, are produced by turbulent eddies with a size greater than that of the first Fresnel zone or the scattering disc $L_P/k\rho_0$, whichever is larger. Large-scale fluctuations are caused by the interaction of turbulence at different scales. It is assumed that the large-scale eddies have some influence on the small-scale eddies. As a consequence of this, the normalised received irradiance, denoted by the letter *I*, is understood to be the product of two statistically distinct random processes, denoted by the I_x and I_y .

$$I = I_X I_Y \,, \tag{2.38}$$

I_x and I_y denote large scale and small eddies respectively. I_x and I_y follow the gamma distribution and their probability density functions are given by [23]:

$$p(I_X) = \frac{\alpha_t(\alpha_t I_X)^{\alpha_t - 1}}{\Gamma(\alpha_t)} exp(-\alpha_t I_X) \quad I_X, \alpha_t > 0, \tag{2.39}$$

$$p(I_Y) = \frac{\beta_t(\beta_t I_Y)^{\beta-1}}{\Gamma(\beta_t)} \exp(-\beta_t I_X) \quad I_Y, \beta_t > 0, \tag{2.40}$$

By fixing I_X and using change of variable, $I_Y = I/I_X$ the conditional probability density function becomes:

$$p(I/I_X) = \frac{\beta_t(\beta_t I/I_X)^{\beta_t-1}}{\Gamma(\beta_t)} \exp(-\beta_t I/I_X) \quad I > 0\,. \tag{2.41}$$

To obtain unconditional probability distribution $p(I_X)$ and $p(I/I_X)$ are averaged over the statistical distribution of I_X.

$$\begin{aligned} p(I) &= \int_0^\infty p\left(I/I_X\right) p(I_X) \mathrm{d}I_X, \\ &= \frac{2\left(\alpha_t\beta_t\right)^{(\alpha+\beta)/2}}{\Gamma\left(\beta_t\right)\Gamma(\alpha_t)} I^{\left(\frac{\alpha_t+\beta_t}{2}-1\right)} \mathrm{K}_{\alpha-\beta_t}\left(2\sqrt{\alpha_t\beta_t I}\right) \quad I > 0, \end{aligned} \tag{2.42}$$

where, α_t and β_t are the effective number of large scale and small scale eddies of the scattering process, $K_n(\cdot)$ is the Bessel function of the 2nd kind and of order n and $\Gamma(\cdot)$ represents the Gamma function. α and β can be expresses as [33]:

$$\alpha_t = \left[\exp\left(\frac{0.49\sigma_l^2}{\left(1+1.11\sigma_l^{12/5}\right)^{7/6}}\right) - 1\right]^{-1}, \tag{2.43}$$

$$\beta_t = \left[\exp\left(\frac{0.51\sigma_l^2}{\left(1+0.69\sigma_l^{12/5}\right)^{5/6}}\right) - 1\right]^{-1}. \tag{2.44}$$

The scintillation index is given by [33]:

$$\sigma_N = \exp\left[\left(\frac{0.49\sigma_l^2}{\left(1+1.11\sigma_l^{12/5}\right)^{7/6}}\right) + \left(\frac{0.51\sigma_l^2}{\left(1+0.69\sigma_l^{12/5}\right)^{5/6}}\right)\right] - 1. \tag{2.45}$$

When $\alpha_t \gg 1$ and $\beta_t \gg 1$ as shown in Fig. 2-7, indicates that there are very large effective numbers of both small and large-scale eddies in the very mild turbulence domain. However, as the irradiance variations rise ($\sigma_l^2 > 0.2$) and the moderate to strong regime is approached, where α_t and β_t then fall significantly as seen in Fig. 2-7, the focusing regime is near. Past the moderate to strong regime and approaching the saturation regime is where $\beta_t \rightarrow 1$. As a consequence of this, the effective number of small-scale cells or eddies will eventually decrease to a value that is specified by the transverse spatial coherence radius of the optical wave. On the other hand, the effective number of discrete refractive scatterers increases once more with an increase in turbulence, and it continues to increase until it eventually becomes unbounded in the saturation regime, as illustrated in Fig. 2-7. Under these circumstances, the gamma–gamma distribution is approaching the negative exponential distribution [5].

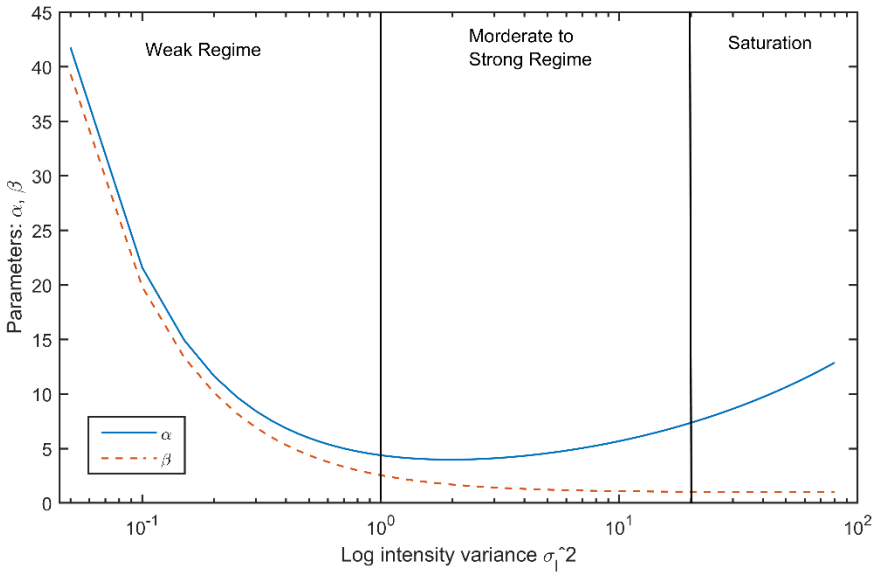

Fig. 2-7 Turbulence regimes for varying α and β values.

2.5 Receiver

The receiver helps in recovering the transmitted signal distorted by atmospheric effects described in the previous sections. The receiver encompasses:

Receiver optics: Collects and focuses the incoming light onto to photodetector. A wider aperture would help in collecting more light but would also pick up more background radiation or noise.

Bandpass Optical Filter: The filter reduces background radiation/noise.

Photodetector: Converts incoming optical signal into an electrical signal.

The electrical signal thus obtained from the photodetector undergoes signal processing to recover the signal with high fidelity.

2.5.1 Photodetector

Photodetection is a technique which converts optical signal into electrical signal that is used to recover the transmitted signal. The information can be encoded on the frequency, phase, or intensity of the radiation coming from an optical source at the Tx. The receiver will then receive this encoded radiation, which will have been sent to it via the free-space channel or the optical fibre. The filtered radiation is focused onto the detector surface that is located in the focal plane by the receiver front-end components, which are the telescope and the optical filter. In the field of optical communications, there are two primary detection strategies that are commonly used: IM-DD and coherent detection. IM-DD is the most straightforward and common detection scheme which would be discussed in forthcoming sections. There are four types of photodetectors that could be used in optical receivers: (i) PIN photodiodes (with no internal gain, which is compensated by a larger bandwidth), (ii) APDs, (iii) photoconductors and (iv) metal–semiconductor metal photodiodes. The last three have internal gain Both PIN and APD are the most popular and widely used detectors for OWC systems, meeting all the requirements mentioned above [5].

2.5.1.1 PIN Photodetector

The PIN photodetector consists of p- and n-type semiconductor materials separated by a very lightly n-doped intrinsic region [34]. In normal operating conditions, a sufficiently large reverse bias voltage is applied across the device. The reverse bias ensures that the intrinsic region is depleted of any charge carriers. For the device to convert an incident photon into an electron/electric current, the energy of the incoming photon must not be less than the band-gap energy of the semiconductor material The incident photon uses its energy to excite an electron from the valence band to the conduction band, thereby generating a free electron–hole pair in the process Normally, the incident light is concentrated on the depleted intrinsic region The high electric field present in this depleted region causes the generated charge carriers to separate and be collected across the reverse biased junction. This gives rise to a current flow in an external circuit. The responsivity of a PIN photodetector is always less than unity but are capable to provide high bandwidth supporting high data rates to the order of 100 Gbps [5].

2.5.1.2 APD Photodetector

The APD is different from the PIN photodetector in that it provides an inherent current gain through the process called repeated electron ionization This culminates in increased sensitivity since the photocurrent is now multiplied before encountering the thermal noise associated with the receiver circuit Hence, the expression for the responsivity of an APD includes a multiplication (or gain) factor given by [5]:

$$M = \frac{I_{\mathrm{T}}}{I_{\mathrm{p}}}, \tag{2.46}$$

where, I_{T} is average current and $I_{\mathrm{p}} = RP_{\mathrm{r}}$. P_r is the average power impinging on the detector for a period T. R is the responsivity which is defined as photocurrent generated per unit incident optical power and is given by:

$$R = \frac{\eta_{\mathrm{qe}} q\lambda}{hc}, \tag{2.47}$$

where, h is the Planck's constant, c is the speed of light in m/s, η_{qe} is quantum efficiency of the photodetector. Typical gain values lie in the range 50–300 [26]; thus, the responsivity value of an APD can be greater than unity The APD offers a higher sensitivity than the PIN detector but the statistical nature of the ionization/avalanche process means that there is always a multiplication noise associated with the APD [35] The avalanche process is also very temperature sensitive.

2.5.2 Direct Detection

In intensity-modulation direct detection, the information is sent using only one degree of freedom, which is the intensity of the light coming from a laser diode (LD) or an light emitting diode (LED). In a direct detection scheme, there is no local oscillator. For this type of receiver to be able to read the coded information, the information that was sent must be linked to the change in intensity of the field that was sent [26]. So, this kind of detection is also called "envelope detection." For an instantaneous incident power $P(t)$, $i(t)$ is the instantaneous photodetector current.

$$i(t) = \frac{\eta_{\mathrm{qe}} q\lambda}{hc} MP(t), \tag{2.48}$$

where M is the photodetector gain factor and η_{qe} is quantum efficiency of the photodetector.

2.5.3 Photodetection Noise

The performance of a wireless optical link is determined by the noise sources, frequency, and distortion performance. Consistent with practically all communication systems, it is crucial to identify the noise sources at the receiver front end, where the incoming signal has the least amount of power. Shot noise from the received photocurrent and noise from the receiver electronics are the two principal sources of noise at the receiver input. Photogenerated shot noise is a key source of optical wireless connection noise. It is fundamentally caused by the discrete character of the photodiode's energy and charge. Due to the resistive element, thermal noise is generated independently of the optical signal received and has a Gaussian distribution. Thermal noise is formed by the receiver's transfer function (i.e, the topology of the preamplifier). Thus, the noise in the circuit is also modelled as having a Gaussian distribution [5].

2.5.3.1 Photon Fluctuation Noise

Most of the noise contribution in an ideal photodetector is due to the quantum nature of light. Number of photons emitted by a coherent source is not constant at all times, although the mean number of photons emitted per second is constant, but the instantaneous emission of photons follows the Poisson distribution resulting in photon fluctuation or quantum noise. Quantum noise is shot noise due to the random arrival rate of photons onto the detector by the optical signal and background radiation. The significance of the quantum fluctuation noise is that it dominates the thermal fluctuations in the photodetector. since $hf > \kappa T_e$ where h and f are the Planck's constant and the radiation frequency, respectively, while κ and T_e represent the Boltzmann's constant and temperature, respectively. The quantum noise is a shot noise with variance [5]:

$$\sigma_{q-\mathrm{pin}}^2 = 2q\langle i\rangle B, \tag{2.49}$$

$$\sigma_{q-\mathrm{apd}}^2 = 2q\langle i\rangle BFM^2, \tag{2.50}$$

$$\langle i\rangle = \frac{\eta_{\mathrm{qe}} q\lambda}{hc} P_r, \tag{2.51}$$

where, *B* represents bandwidth in Hz, and *q* represents the electron charge in coulombs. *F* is the ratio of mean-square current gain $\langle g^2 \rangle$ and mean gain *g*.

2.5.3.2 Dark Current and Excess Noise

Since the photocurrent is proportional to the amount of light impinging it, the photon shot noise goes up as the amount of light hitting it goes up. The noise from the dark current, which flows even when there is no light coming in, defines the lower limit of this relationship. It happens when electrons move from the valence band to the conduction band for reasons other than photon-induced excitation. Its size is closely related to the photodetector material's energy band gap (s) Materials with a large band gap, like silicon (Si), indium phosphide (InP), and gallium arsenide (GaAs), have very low values of mean dark current, id, but germanium (Ge) could have a significant value when it is used at room temperature [36]. The dark current is a mix of bulk and surface leakage currents. It doesn't tell us anything useful, so it's called "shot noise," and its variations are shown below.

$$\sigma_{\mathrm{db}}^2 = 2qI_{\mathrm{d}}FBM^2, \tag{2.52}$$

$$\sigma_{\mathrm{ds}}^2 = 2qI_{\mathrm{l}}B, \tag{2.53}$$

I_{d} is the primary unmultiplied dark current and I_{l} is the surface leakage current.

The dark current consists of diffusion, tunnel, leakage, and generation–recombination occurring in the space–charge area and is proportional to the depletion region's volume [36]. Photodetectors that use an internal avalanche gain mechanism to raise the signal above the thermal noise of the receiver's amplifier stages are characterised by what is known as excess noise [25]. According to [25], the extra noise in an APD is the result of a multiplication process in the high-field area of the detector, where each main electron hole can generate an additional electron via impact ionisation of bound electrons. In a process of cascading, these extra carriers can subsequently generate even more carriers. The surplus noise grows as the gain increases. Since the gain is wavelength-dependent, the extra noise varies with the wavelength of the incident light. Similarly, the signal-generated photocurrent is similarly magnified by the gain, demonstrating that optimal SNR is achieved at a specific gain. If all main carriers were multiplied evenly in an APD, the mean-square current gain $\langle g^2 \rangle$ would equal the mean gain g, and the surplus noise, as described by $F = \langle g^2 \rangle / g$, would equal 1. This describes PIN photodetectors [25]. Due to the statistical nature of the avalanche process, *F* in an APD and other avalanche devices is always greater than 1.

2.5.3.3 Background Radiation

This sort of noise is caused by the detection of environmental photons. Localized point sources (such as the Sun) and extended sources also contribute to background radiation (ambient light) noise (e.g, the sky) It is anticipated that background radiation from other celestial bodies, such as stars and reflected background radiation, is too weak to be considered for a terrestrial FSO link; however, they contribute significantly to background noise in deep space FSO. The following expressions describe the irradiance (power per unit area) from background sources.

$$I_{\text{sky}} = N(\lambda)\Delta\lambda\pi\Omega^2/4, \tag{2.54}$$

$$I_{\text{sun}} = W(\lambda)\Delta\lambda, \tag{2.55}$$

where $N(\lambda)$ and $W(\lambda)$ are the spectral radiance of the sky and spectral radiant emittance of the sun, is the bandwidth of the optical bandpass filter (OBPF) that precedes the photodetector, and is the field of view angle of the photodetector in radians. By carefully selecting a receiver with a very narrow field of view (FOV) and, background noise can be drastically reduced. OBPF coatings on the receiver optics/telescope with 1 nm are now commercially available. There are additional empirical values of $N(\lambda)$ and $W(\lambda)$ for various observation situations in the literature [21, 26]. Background radiation consists of a shot noise with variance:

$$\sigma_{\text{bg}}^2 = 2qBR(I_{\text{sky}} + I_{\text{sun}}). \tag{2.56}$$

2.5.3.4 Thermal Noise

Thermal noise, also known as Johnson noise, is present in all conducting substances. It is brought about by the thermal fluctuation of electrons in any receiver circuit with equivalent resistance R_{L} and temperature T_{e}. Electrons are in constant motion, but they regularly clash with the atoms or molecules of the material. Every electron in free flight generates a minute current. Obviously, the aggregate of all these currents measured over a period must equal zero. Thermal noise is considered white noise because the power spectral density (PSD) is frequency independent. Moreover, the thermal noise follows a Gaussian distribution with zero mean and variance for IM-DD is described below [5]:

$$\sigma_{\text{th}-\text{D}}^2 = \frac{4\kappa T_{\text{e}} B}{R_L}, \tag{2.57}$$

where, $\sigma_{\text{th}-\text{D}}^2$ is the thermal noise, κ is the Boltzmann's constant.

2.5.3.5 Noise Equivalent power

The amount of optical power incident on the surface of a photodetector that produces a signal at the output of the detector, which is just equal to the noise generated internally by the photodetector, is defined as the NEP The NEP is roughly the minimum detectable input power of a photodiode Another equivalent way of stating NEP is to take the ratio of the total noise current to the responsivity at a particular wavelength. For a photodetector in which the dark current is the dominant noise source, the expression for NEP is given by [5]:

$$i(t) = \frac{hc(2qi_{\text{d}})^{0.5}}{\eta_{\text{qe}} q\lambda}, \tag{2.58}$$

Note that, the NEP parameter specified by the manufacturer has the units W/Hz. The Newport 818-BB-35A photodetector [37] has an NEP of 25 pW/Hz. This means that the receiver is thermal noise limited [38] and to get the total noise the NEP has to be scaled to the bandwidth of the optical communication system.

2.5.3.6 Intensity Noise

This is generated by the amplitude fluctuation of the optical signal, and is usually expressed in terms of relative intensity noise (RIN) given by [5]:

$$\sigma_{\text{in}}^2 = \eta_{\text{RIN}} (RMP_{\text{r}})^2 B. \tag{2.59}$$

For a typical laser diode, η_{RIN} is about -160 to -150 dB/Hz.

2.5.3.7 Signal to Noise Ratio

The signal to noise ratio for IM/DD receivers is described as [5]:

$$\mathrm{SNR}_{\mathrm{IM-DD}} = \frac{I_{\mathrm{p}}^2}{N_{\mathrm{T}}} = \frac{(RMP_{\mathrm{r}})^2}{\sigma_q^2 + \sigma_d^2 + \sigma_{\mathrm{bg}}^2 + \sigma_{\mathrm{th}}^2 + \sigma_{\mathrm{in}}^2}, \tag{2.60}$$

where, $\sigma_q^2, \sigma_d^2, \sigma_{\mathrm{bg}}^2, \sigma_{\mathrm{th}}^2, \sigma_{\mathrm{in}}^2$ are the quantum fluctuation noise, dark noise, background noise, thermal noise, and intensity noise.

2.6 Optical Link Budget Calculations: Considerations

Contrary to classical belief that light waves travel in straight lines, light bends around or spreads out while travelling around or through an object, respectively. This spreading or bending of light waves is termed as diffraction [23]. The extent of spreading depends on the λ of the laser used and shape of the wavefront. The idea of effective isotropic radiated power (EIRP) for calculating RF link budgets is originated from considering the power transfer between the Tx and Rx. The receiver collects a portion of the transmitted wave field which could be approximated to a spherical wave. Advancements in antenna configurations led to modification of shape of wavefronts of transmitted waves. RF link budgets of such systems were evaluated using the concept of EIRP and some correction factors. However, in the optical case the communication between the Tx and Rx is anything but isotropic in nature. Diffraction is a characteristic of all electromagnetic waves and RF is no different. In case of RF, the wavefronts can be treated as spherical at the Rx locations as the diffraction effects occur close to the Tx. Then again in optical case with laser beam propagating through an aperture experiences spatial broadening due to diffraction. As a result, the phase front characteristics change at very large distances from the transmitter aperture and should be considered for power transfer calculations [126].

2.6.1 Link Budget for Satellite Links

Using the Helmholtz wave equation [23], the beam intensity at a distance *L* from the transmitter for a collimated beam is given as [126]:

$$I(L,\rho) = A_0^2 \frac{R_T^2}{R^2(L)} e^{-\rho^2/R^2(L)}, \tag{2.61}$$

where, A_0^2 is the squared amplitude of the radiation at the output of the aperture, $R(L)$ is the radius of the collimated beam at L and R_T is the radius of the aperture. $R(L)$ can be further expressed as:

$$R^2(L) = R_T^2(1 + \alpha_d^2 L^2), \tag{2.62}$$

where, the diffraction parameter α_d is given by:

$$\alpha_d^2 = \frac{1}{kR_T^2}, \tag{2.63}$$

The power transferred to the receiver $P_R(L)$ with an aperture of R_R at a distance of L from the transmitter is calculated as:

$$P_R(L) = 2\pi \int_0^{R_R} I(L,\rho)\rho d\rho = \pi A_0^2 R_T^2 (1 - e^{-R_R^2/R^2(L)}) \tag{2.64}$$

The transmitted power P_T is given as:

$$P_T = \pi R_T^2 A_0^2 \tag{2.65}$$

Re-writing (2.64) using (2.62), (2.63) and (2.65) we obtain the power transfer equation given as:

$$P_R(L) = P_T \left(1 - e^{-R_R^2 R_T^2 k^2/(k^2 R_T^4 + L^2)}\right) \tag{2.66}$$

(2.66) is valid when the receiver is in the near-field region of the transmitter. The first Fresnel zone is determined by approximating the distance L in the exponent of (2.66) given by the inequality,

$$L^2 \gg k^2 R_T^4 \text{ or } L > kR_T^2\,, \tag{2.67}$$

Which simplifies (2.66) to:

$$P_R(L) \approx P_T \left(1 - e^{-R_R^2 R_T^2 k^2/L^2}\right), L > kR_T^2 \tag{2.68}$$

To illustrate the concept, assume $\lambda = 1550$ nm and $R_T = R_R = 0.1$ m, the first Fresnel zone is located at $L_{Fresnel}$ = 40.5 km.

Consider the exponent in (2.68) for distances L for which

$$R_R^2 R_T^2 k^2/L^2 \gg 1 \text{ or } L > kR_T R_R \tag{2.69}$$

This condition determines the far-field of the transmitter in which (2.68) is approximated to:

$$P_R(L) \approx P_T \left(\frac{R_R^2 R_T^2 k^2}{L^2}\right), \qquad L > kR_T R_R \tag{2.68}$$

To give an idea of the far-field distance assume $\lambda = 1550$ nm and $R_T = 0.1$ m and R_R = 0.25 m, L_{Far} = 101 km. It means that an optical receiver has t be placed at a distance of 101 km to be in the far-field of the transmitter.

To draw a connection between RF and optical link budgets, lets define the Transmitter G_T and Receiver gain G_R as:

$$G_T = R_T^2 k^2 \tag{2.69}$$

$$G_T = R_T^2 k^2 \tag{2.70}$$

The exponent in (2.66) turns to:

$$\frac{R_R^2 R_T^2 k^2}{k^2 R_T^4 + L^2} = \frac{G_T L_{FS} G_R}{1 + G_T^2 L_{FS}}, \tag{2.71}$$

where, L_{FS} is the free space path loss given by:

$$L_{FS} = \left(\frac{1}{kL}\right)^2, \tag{2.72}$$

The equations for the received power at near-field, the first Fresnel zone and the far-field can be re-written using (2.69-2.72) as:

$$P_R(L) \approx P_T \left(1 - e^{-\frac{G_T L_{FS} G_R}{1 + G_T^2 L_{FS}}}\right), \quad \text{near-field case} \tag{2.73}$$

$$P_R(L_{Fresnel}) \approx P_T \left(1 - e^{-\frac{G_T L_{FS} G_R}{1 + G_T^2 L_{FS}}}\right), \text{ first Fresnel zone} \tag{2.74}$$

$$P_R(L_{Far}) \approx P_T G_T L_{FS} G_R, \quad \text{far-field case} \tag{2.75}$$

As per the **ITU-R S.1590 – Technical and Operational characteristics of satellites operating in the range of 20-375 THz,** the link budget for satellite links is given by [127]:

$$P_R = P_T + G_T - L_{FS} + G_R - T_a - T_r - T_t, \tag{2.76}$$

where, T_t is the transmitter which includes absorption, scattering or reflection losses typically taken as 0.5 dB, T_r are the receiver losses including the same losses as T_t, and T_a is the atmospheric loss in the case of space to ground links. Typical value is up-to 0.03 dB. For space-to-space links T_a is assumed to be 0 dB.

2.6.2 Link Budget for Terrestrial Links

As per **ITU-R P.1814 – Prediction methods required for the design of terrestrial free-space optical links**, the link budget for terrestrial links is given by the following expression [128]:

$$M_{link} = P_T - S_r - L_{geo} - L_{atm} - L_{Scintillation} - L_{System}, \tag{2.76}$$

where:

S_r (dBm)	Sensitivity of the receiver dependent on the data-rate
L_{geo}(dB)	Geometrical loss due to beam spreading

L_{atm}(dB)	Attenuation due to atmospheric absorption and scattering
$L_{Scintillation}$(dB)	Attenuation due to atmospheric turbulence
L_{System}(dB)	Losses accounting for misalignment, transmitter and receiver optics and background radiation
M_{link}(dB)	Link margin of the communication system.

The standard recommends that the effects of scintillation can be reduced by employing multiple transmit beams (spatial diversity), avoiding installation near hot surfaces and possibly installing the setup at altitudes > 1m. Although, turbulence introduces power penalties to the communications system [128] assumes that this penalty is compensated by M_{link}. It is noted that increasing the transmit power to overcome turbulence is effective only in very weak turbulence[115]. This technique fails for other turbulence regime. Hence, $L_{Scintillation}$ is not considered while performing link budgets for terrestrial links.

2.7 Summary

This chapter provided a comprehensive review about the fundamentals of FSO communications. This included a description of Tx, the atmospheric channel and the receiver. The Tx section gave an overview of the beam propagation models, laser safety and safety standards, and atmospheric transmission windows. The atmospheric channel section dealt with molecular scattering and absorption and aerosol scattering and absorption. Depending on the size parameter Rayleigh and Mie scattering were discussed along with the turbulence models for different turbulence regimes. The receiver section described the PIN and APD photodetectors, the direct detection process and photodetection noise. Finally, the link budget section discussed about link budget considerations and diffraction effects. This section brought about the connections between EIRP and RF link budgets. Furthermore, this section derived the power transfer equation for near-field, the first Fresnel zone and the far-field using the Helmholtz wave equation. Under far-field conditions for optical communications the power transfer equation is similar to RF link budget equation. Far-field condition for λ = 1550 nm is achieved if the distance between the transmitter and receiver is more than 101 km. Following that link budgets for space links and terrestrial links were described.

Chapter 3: Coverage Models for Ground to Train Communications

3.1 Introduction

With the increasing concerns regarding global warming, governments and researchers are paying greater attention to reducing greenhouse gas emission reduction, thus the Kyoto Protocol of 1997 [39]. Transport is one of the key contributors to past and future climate change. For global emissions, it has been shown that air travel has the highest specific climate impact (sCI), while rail and coaches have the lowest sCI [40]. Travelling by trains is the most environment-friendly, where the greenhouse effect of gas emissions per kilometre is 80% less than cars and they can carry more people and offer reduced noise pollution [41]. For rail transport to be even more attractive the passengers will demand access to broadband Internet access (BIA) for a range of applications including messaging, video on demand, voice over Internet protocol (VoIP), TV, streaming, videoconferencing, etc., where the train journey will be seen as the extension of working at home or office (i.e., the concept of home-to-office-to-home). In addition, broadband links between trains and infrastructure are essential for trains' safety and communication related information (i.e., trackside equipment, trains, signalling system, and people), which are needed by the network managers and railway operators.

In the past few years, we have seen a renewed interest in Internet connectivity on-board the trains, which are predominantly based on RF technologies. These are leaky coaxial cable (LCX), Wi-Fi and WiMAX with a maximum bandwidth of 2 Mbps, 54 Mbps and 40 Mbps, respectively, trackside and satellite [42]. The latter is better suited to certain types of traffic such as broadcast TV, where the bandwidth is shared across all the fleet and can improve the overall link performance by, for example, complementing the coverage offered by cellular systems. Alternatively, passengers could directly connect their smart devices via their cellular service provider to have BIA [43], 44], which requires sufficient radio coverage along the lines and suffers from RF signal attenuation (14 – 30 dB) due to Faraday cage [45]. One possible option to overcome this is to adopt relay-based systems at the cost of increased installation and maintenance costs. A train access terminal (TAT) or “mobile router” is another option to optimize performance and throughputs [46], which can support several many different technologies. In TAT, the incoming signal from the antenna positioned outside the train is fed to the access points in carriages, which overcome transmission losses and reduce the handover for all passengers into a single terminal with the aggregated traffic. The average throughput for the aforementioned RF systems is at most 1.4 Mbps [42], which is unsatisfactory in terms of bandwidth required for web-conferencing (Skype call) and accessing video sharing sites (Netflix). This is mainly due to the availability of RF spectrum (i.e., the bandwidth) and multi-path propagation characteristics

of the environment [47]. In accordance with UK Crosscountry Wi-Fi terms and conditions, any usage of service exceeding 70 Mb in standard class and 100 Mb in the first-class coaches is classified as excessive usage and access to the Wi-Fi is reduced [48].

In [49], a mobile hot-spot network (MHN) was designed for subway trains using the millimetre-wave technology with a carrier frequency of 25.5 GHz. Two antennas or a mobile terminal equipment (MTE), which emit narrow beams, are installed at either end of the train. MTEs attempt to connect to MHN radio units deployed along the trackside and perform handover when the train crosses edges of the cells' coverage. The practical demonstration of MHN system yielded throughputs of 1.25 Gbps and 110 Mbps for the downlink and uplink, respectively [49]. In [50], a throughput of 1.5 Gbps using a 97 GHz millimetre wave radio access system connected via a bidirectional radio over fibre network for a train with a speed of up 240 km/h was experimentally demonstrated. The millimetre-wave distributed radio access units deployed on the ground were connected to the bidirectional analogue RoF (Radio over fibre) network for establishing a high-speed link with the on-board transceiver. In [51], a 20 Gbps wavelength division multiplexed fibre-RF wireless system (at 90 GHz) between the central station and the BS was investigated within an indoor environment. The work in [51] is based on the moving BS concept where the high-speed train communicates with the same BS in order to prevent frequent handovers.

However, in the railway environment there are a number of issues that will affect wireless BIA on board the trains including: (*i*) Faraday cage – due to the metallic structure of the train, which results in power losses of transmitted signals; (*ii*) high vibration, which require isolation of communication devices; (*iii*) ground infrastructures; (*iv*) pylons, tunnels and overhead cables, which can result in loss of synchronization, disconnections, and packet losses; (*v*) adding/removing train carriages, where the communication networks need to detect this automatically; and (*vi*) the bandwidth bottleneck. The latter can be solved by employing FSO wireless technologies. FSO offers a few features including (*i*) huge unregulated license-free spectrum (i.e., bandwidth order of magnitude higher the RF technologies); (*ii*) excellent transmission security at the physical layer; (*iii*) robustness to the RF-induced electromagnetic interference; and (*iv*) compatibility with the backbone optical fibre networks [52].

Implementation of FSO for G2T communication in this chapter focuses on providing a large coverage area for the BS, which reduces the deployment costs and provides uninterrupted internet service with negligible handover delay. Previous works on FSO systems have provided a comprehensive theoretical study and experimental validation on G2T communications. A high data rate (1 Gbps) G2T communication was proposed in [53], where an acquisition, tracking and pointing (ATP) mechanism based on the beaconing system was used to provide stable tracking and fast handover (i.e., 100 ms) in FSO links for high-speed trains. In [54], a high-speed image sensor-based ATP mechanism

was used in place of a 2-quadrant photodetector (PD) to detect the beacon signal from the adjacent BS. Using a new image processing algorithm for recognition and labelling beacon signals and a feedback control to control the direction of the mirror by employing a mirror angle sensor, the handover delay was reduced to 21 ms. In [55], rotating transceivers located on the ground and the train was employed to increase the coverage area. The rotating transceiver on the train switches from the source BS to a target BS, while the other Tx on the train maintains a continuous link from the source BS thereby mitigating the impact of handover. In [56], a dual transceiver scheme with a wide beam was proposed, which is deployed on both the ground and on the train, as opposed to a single rotating transceiver on the ground in [55], to increase the coverage area, reliability, and the complexity of the FSO system. In [57], two FSO coverage models namely single wavelength and dual wavelengths were proposed for seamless handovers and high bandwidth communications.

The proposed system in [56] employs wide optical beams covering 250 m per transceiver with a divergence angle of 10 mrad to extend the trackside coverage, thereby reducing the number of FSO BSs. FSO links using wide divergence angle laser sources suffer from high geometric losses [17], which in case of wide beam systems may result in frequent link outages during handover between BS or result in frequent outages within the BS. In this chapter, we propose a sectorised BS model for G2T communication, which provides a stable high-speed link between the train and the ground BSs under harsh weather conditions and mitigates the effect of geometric loss.

The rest of the chapter is organized as follows: Section 3.2 describes ground-train communications which include G2T communications using sectorised BSs and train-to-ground (T2G) communications. Section 3.3 describes the system model. Results and discussion using numerical simulations pertaining to G2T communication are presented in section 3.4.

3.2 System Model

The system block diagrams for the intensity modulation/direct detection (IM/DD) FSO links for G2T and T2G communications are shown in Fig. 3-1. For G2T communication, see Fig. 1(a), the optical beam from the laser source is launched into a single mode fibre (SMF) the output of which is amplified using EDFA prior to being applied to a 1×10 fibre array. Lights from the fibre array are launched into a free space channel using diverging optics positioned at the end of each fibre. For T2G communication, see Fig. 1(b), 3 Txs (i.e., laser sources) with divergence angles of 60 mrad are used to illuminate the BSs. Optical beams propagating through the free space channel will experience both intensity and phase fluctuation due to atmospheric fog and turbulence, which will degrade the link performance.
For G2T and T2G communications, the received electrical signal is given by:

$$y = h(t) * x(t) + n(t), \tag{3.1}$$

where x is the transmitted signal, n is additive white Gaussian noise with variance σ_n^2, and h is the channel gain, which is given by:

$$h = h_a h_t h_g, \tag{3.2}$$

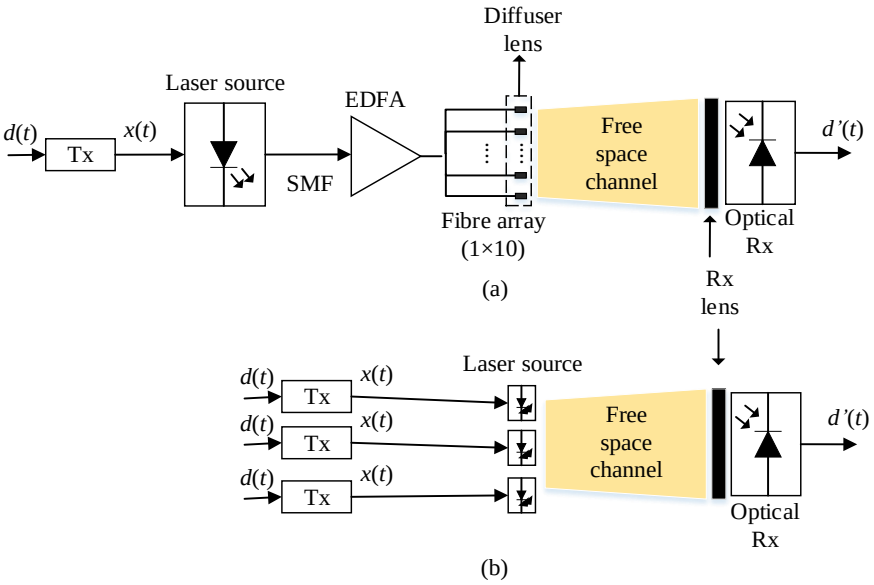

Fig. 3-1 A block diagram of line-of-sight FSO transmission for: (a) from ground-BS to the train and (b) from train to the ground-BS.

h_a and h_t are attenuation constants due to the atmospheric channel and turbulence, respectively. For an FSO link, h_a is given by Beer's law as [58]:

$$h_a = e^{-\varepsilon l}, \tag{3.3}$$

where l is the link length in m, and ε is the attenuation coefficient in m^{-1}.

The spreading of the propagating beam results in a spot size greater than the Rx's aperture, which leads to the geometric loss as given by [59]:

$$h_g = 10 \log_{10} \left[\frac{d_{\mathrm{rx}}}{d_{\mathrm{tx}} + l_{\mathrm{link}} \theta_{\mathrm{div}}} \right]^2, \tag{3.4}$$

where d_{tx} and d_{rx} are the Tx and Rx's apertures, respectively, and l_{link} is the link range.

The optical intensity I of a wave propagating in a turbulence channel undergoes random fading effect with the normalized variance or the scintillation index given as [60]:

$$\sigma_I^2 = \frac{\langle I^2 \rangle - \langle I \rangle^2}{\langle I \rangle^2}, \tag{3.5}$$

where $\langle . \rangle$ denotes the ensemble average equivalent to long-time averaging with the assumption of an ergodic process.

Based on (5), the strength of turbulence can be classified as weak ($\sigma_I^2 < 1$), moderate ($\sigma_I^2 \cong 1$) and strong ($\sigma_I^2 > 1$) [61]. Assuming plane wave propagation, σ_I^2 is given by [62]:

$$\sigma_I^2(D) = \exp\left[\frac{0.49\,\sigma_R^2}{\left(1 + 0.653d^2 + 1.11\sigma_R^{\frac{12}{5}}\right)^{\frac{7}{6}}} + \frac{0.51\,\sigma_R^2\left(1 + 0.69\,\sigma_R^{\frac{12}{5}}\right)^{-\frac{5}{6}}}{(1 + 0.9d^2 + 0.621\,d^2\sigma_R^2)^{\frac{12}{5}}}\right] - 1, \tag{3.6}$$

where $d = \frac{D}{2}\sqrt{\frac{k}{l}}$ is the circular aperture scaled by Fresnel zone provided, k is the wavenumber, and D is the Rx's aperture diameter. σ_R^2 is Rytov variance given by:

$$\sigma_R^2 = 1.23 C_n^2 k^{7/6} l^{11/6}, \tag{3.7}$$

where C_n^2 is the refractive index structure constant with typical values of 10^{-17} $m^{-2/3}$ and 10^{-13} $m^{-2/3}$ for weak and strong turbulence regimes, respectively [59].

Log-normal distribution serves as a good approximation for turbulence regimes where $\sigma_I^2 < 0.3$ [60] and the average BER for log-normal turbulence is approximately given by [62]:

$$P_e \approx \frac{1}{\sqrt{\pi}} \sum_{i=1}^{g} w_i Q\left(\frac{\eta I_0 e^{-2\sigma_x^2 + z_i\sqrt{8\sigma_x^2}}}{\sqrt{2N_0}}\right), \tag{3.8}$$

where g is the order of approximation, z_i, $i = 1,\ldots, g$ is the zero of the g^{th} order Hermite polynomial, w_i is the weight factor for the g^{th}-order approximation, I_0 is the signal light intensity without turbulence, $\sigma_x^2 \approx \sigma_l^2/4$ is the variance of log-amplitude fluctuations, η is the optical-to-electrical conversion coefficient, and N_0 is the noise power spectral density.

3.2.1 Power budget analysis

The received power can be expressed as a function of the transmit power P_{tx} and the system losses is given by:

$$\mathrm{P_{rx}}(l) = 10^{\frac{(L_{\mathrm{atm}} l)}{10}} \times 10^{\left(\frac{h_g}{10}\right)} \times 10^{\left(\frac{L_{\mathrm{Misc}}}{10}\right)} P_{\mathrm{tx}}, \tag{3.9}$$

where L_{atm} is given by [58]:

$$L_{\mathrm{atm}} = \frac{17}{V}\left(\frac{\lambda}{550}\right)^{-q}, \tag{3.10}$$

where V is the meteorological visibility in km, λ is the wavelength in nm, and q is the size distribution of scattering particles, which follows Kruse [63] model and is expressed as:

$$q = \begin{cases} 1.6 & V > 50 \text{ km} \\ 1.3 & 6 \text{ km} < V < 50 \text{ km} \\ 0.16V + 34 & 1 \text{ km} < V < 6 \text{ km} \\ V - 0.5 & 0.5 \text{ km} < V < 1 \text{ km} \\ 0 & V < 0.5 \text{ km} \end{cases}, \tag{3.11}$$

L_{Misc} is the coupling losses due to optics to fibre and fibre to coupling. Fig. 3-2 depicts the beam footprint onto the receivers placed on the train carriages. Note that the receivers are aligned with the field of view of the transmit beams. For a Gaussian beam, the received optical power at any point along the rail track is given by the beam offset r and its radius w_R as shown in Fig. 3-2 [58], is given as [56, 58]:

$$\frac{P_{\mathrm{rx}}(r,l)}{P_{\mathrm{rx}}(l)} = e^{-\frac{2r^2}{w_R^2}}. \tag{3.12}$$

Combining (9) and (12), the received power can be expressed as:

$$P_{\mathrm{rx}}(r,l) = P_{\mathrm{tx}} \times 10^{\frac{(L_{\mathrm{atm}} l)}{10}} \times 10^{\left(\frac{h_g}{10}\right)} \times 10^{\left(\frac{L_{\mathrm{Misc}}}{10}\right)} \times e^{-\frac{2r^2}{w_R^2}}. \tag{3.13}$$

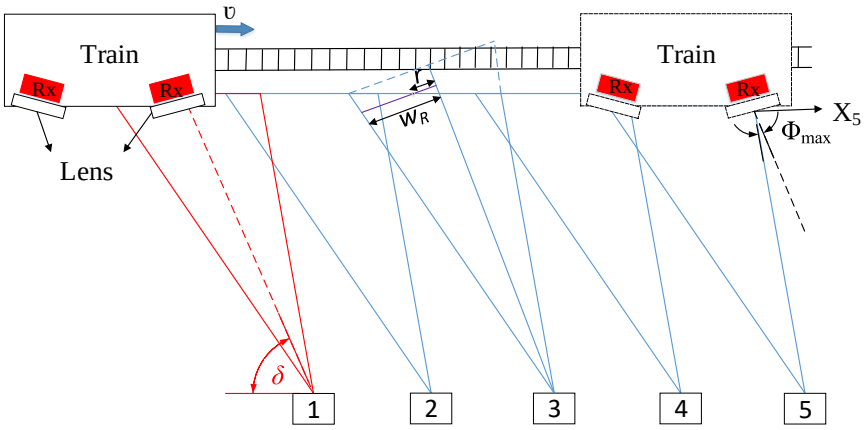

Fig. 3-2 The Rx's alignment offset angle with respect to the transmit beam (1-5) direction.

3.3 G2T Duplex Communication

A G2T duplex communication system is analysed based on the parameters provided in Table 3-1.

Table 3-1 Key System Parameters

COMMON PARAMETERS	
PARAMETER	**VALUE**
Wavelength	1550 nm
Train speed	300 km/hr.
Tx and Rx apertures	1 and 20 cm
Track-BS distance	2 m
Rx power @17 dB	86.6 µW
Photodetector	PIN
Rx wavelength range	500-1630 nm
Rx 3 dB Bandwidth	10 kHz – 12 GHz
Noise equivalent power	24 pW/$\sqrt{Hz}$
Responsivity at 1550 nm	0.85 A/W

G2T COMMUNICATIONS				
Fiber number	Tilt angle (δ) (mrad)	Transmit power (mW)	Beam divergence (mrad)	Coverage length (m)
1, 10	24	43.0	5	20
2, 9	31	57.2	8	20
3, 8	45	62.7	15	20
4, 7	66.5	68.6	24	15
5, 6	100	72.0	37.5	10

RECEIVER LENS G2T COMMUNICATIONS	
Diameter	200 mm
Effective focal length	400 mm
Wavelength	350-2200 nm

EDFA	
Operating wavelength	1528-1564 nm
Output power	18 dBm to 26dBm
Noise figure	< 5 dB
Input power	-12 dBm to +7dBm
Laser class	3B
RECEIVER LENS T2G COMMUNICATIONS	
Diameter	250 mm
Effective focal length	400 mm
Wavelength	350-2200 nm

The parameters shown in Table 3-1 were obtained based on the signal model presented in section II and the following criteria of (*i*) h_g limited to 15 dB per beam; and (*ii*) a minimum train (i.e., track) coverage length of 10 m per beam. Fig. 3-3 shows the schematic block diagram of G2T system based on a sectorised BS, which uses a laser/fibre array for illumination of the train (i.e., trackside) in order to provide a data communications link. A single laser source is used the output of which is amplified using an EDFA prior to being split into 10 fibre based Txs. Beam expanding optics are used to expand the light emerging from the fibre-array for illuminating moving train. Note, the spacings between the beam expanders are 7 cm, and the overlapping areas of the optical beams on the track are 2 m to provide seamless connectivity throughout the coverage length of 210 m (i.e., the spacing between BSs). As illustrated in Fig. 3-2 the effective coverage length along the track is 170 m (i.e., 2×85 m) and there is a dead zone of 40 m, where there is no need for optical illumination. Note, in FSO links a single beam with a large divergence angle can effectively cover a wide area but at the cost of increased hg, which ultimately limits the transmission range and thus the maximum achievable transmission data rates. Though the hg can be mitigated by increasing the transmit power, however, the eye and skin safety regulation will set the maximum transmit optical power level. In this work, we have adopted the sectorised BS topology with reduced the divergence angle per optical Tx.

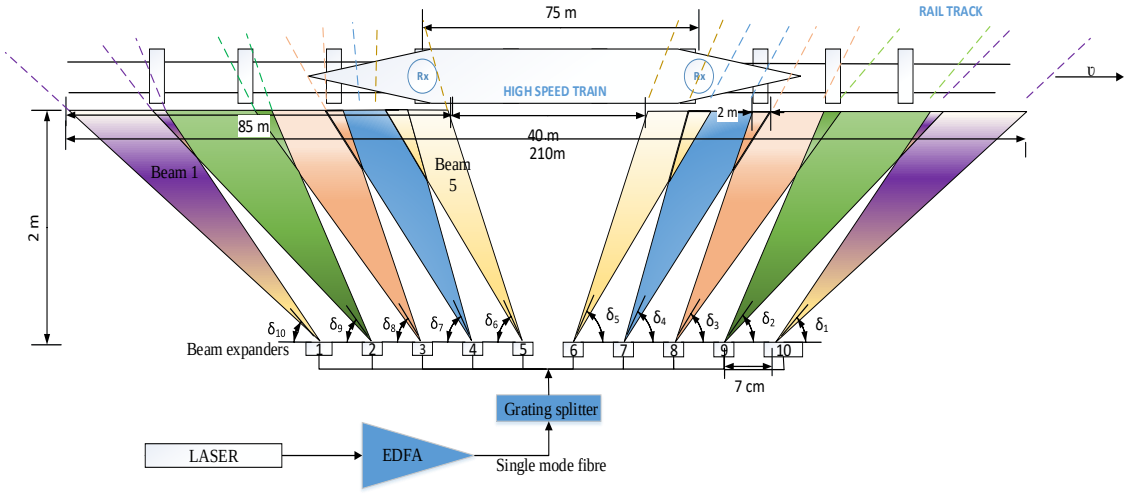

Fig. 3-3 The laser/fibre array covers 170 m (85 m on either side). The distance between the two BSs is 210 m.

Based on the experimental work conducted on a commuter train travelling at a speed of 130 km/h the physical layer handover delay was reported to be 120 ms [64]. Using a handover delay time of 120 ms as the benchmark, the separation between the two Rxs on the train should be 75 m, see Fig. 3-3. This allows allocation of a delay time of 210 ms for the inter-BS and intra-BS handover for each Rx for a train travelling at a speed of 300 km/hr while the other Rx is still in communications with the ground BS to ensure seamless connectivity. In [64], a tracking scheme was proposed where the delay in the physical layer was contributed due to the physical mirror handover time. The Rxs on the train are composed of a lens and an optical Rx (i.e., a PD and a trans-impedance amplifier). The regenerated electrical signal is applied to a matched filter and then to a threshold detector (slicer) to recover the transmitted data stream.

As shown in Fig. 3-3, the Rx's are aligned with beam 1, where δ is the tilt angle of the beam 1. With the train travelling from left to right, the Rx will have an offset angle Φ_{max} with respect to the beam directions, see Fig. 3.2, which is given by:

$$\Phi_{\max} = \tan^{-1}\left(\frac{x_{\text{track}}}{y_d}\right) - \delta. \tag{3.14}$$

For the T2G link, three Txs are located on the roof of the train one at each end with a spacing of d pointing to the BSs as depicted in Fig. 3-4, which provides a seamless handover between the BSs. The transmitted beams with the divergence angle of θ illuminate the track side (i.e., the BSs) with coverage length of *x* and with some beam overlapping. For the train to establish a connection with the next BSs prior to dropping the connection with current BS, the coverage length is made to be larger than the spacing between two BSs, see Fig. 3-4.

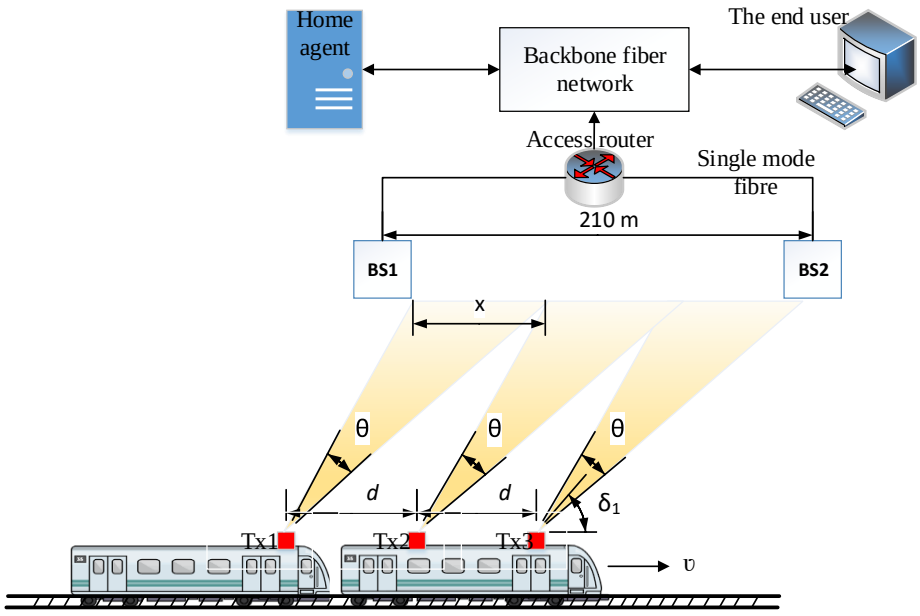

Fig. 3-4 Train to ground communication where the coverage area of each transceiver is 75m. The transceivers are spaced 75m apart from each other.

Note, at the Rx a lens is used to focus the beam onto a small area PD or an optical fibre pigtailed optical Rx. However, for a moving train, the lens focal point position is no longer stationary and is moving away from the centre position (i.e., when the train is stationary), see Fig. 3-5, which results in the loss of beam being coupling to the optical Rx (i.e., link failure). Therefore, the vertical offset of the lens focal point is given as:

$$\Delta q = f \times \tan \Phi, \tag{3.15}$$

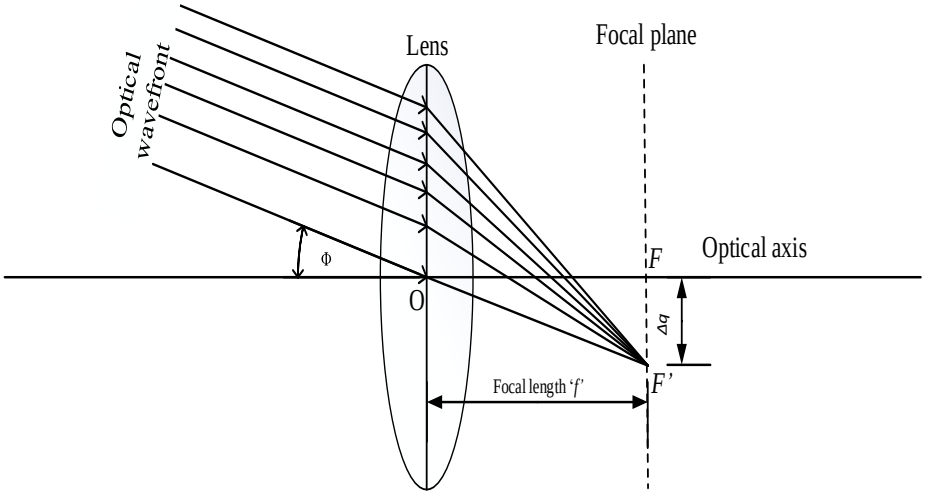

Fig. 3-5 Oblique beam through a perfect lens

where f is the focal length. For Φ and f of 4.431° and 40 cm, respectively the maximum Δq is 3 cm**,** which is orders of magnitude larger than the surface area of a high-speed PD (e.g., 60 μm). To overcome this problem and ensure light coupling there are several possible solutions including (*i*) Rx diversity, which is highly costly and complex; (*ii*) tracking Rx; (*iii*) fibre-based coupling; and (*iv*) cascading lenses. In this work, (*iii*) and (*iv*), which are simpler to implement, are adopted. Fig. 3-6 shows an Rx arrangement based on the cascading lenses, where the incoming light following propagation through lenses is coupled into a multimode fibre (MMF) array, which is positioned at the radial gradient (curve) of the cascading lenses focal points. The emerging light beams from the MMF array is coupled into a series of PDs using a collimator and a photonic lantern. By using equal gain combining (EGC), all the PD's currents can be summed and processed as whole. The equivalent focal length f_{eq} for n lenses is given by:

$$\frac{1}{f_{\mathrm{eq}}} = \frac{1}{f_1} + \frac{1}{f_2} + \cdots . + \frac{1}{f_n}, \tag{3.16}$$

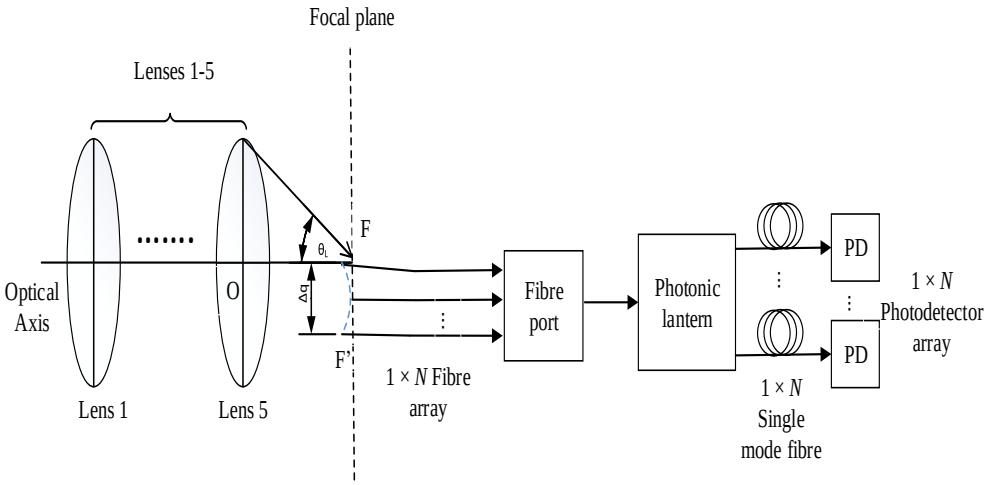

Fig. 3-6 The Rx configuration based on series of cascading lenses

Fig. 3-7 depicts the vertical displacement with respect to Φ for f of 40 cm, which represents a single lens setup and 8 cm, for five cascaded lens setups. The variation of Δq is in orders of millimetres for reduced f. Note that, light passing through an uncoated glass substrate undergoes Fresnel reflection, thus resulting in ~ 8% light reflection at each interface. Due to this effect, only 92% of the incoming light is transmitted through each lens, thus only 65% of the incident light is emerging from lens 5. One possible solution would be to apply anti-reflection coating on each lens thereby increasing the optical transmission. For light coupling into a fibre, the incident angle of the light from the lens should be less than the numerical aperture (NA) of MMF, which is given by:

$$\theta_L = \tan^{-1}\left(\frac{0.5D_L}{f}\right), \tag{3.17}$$

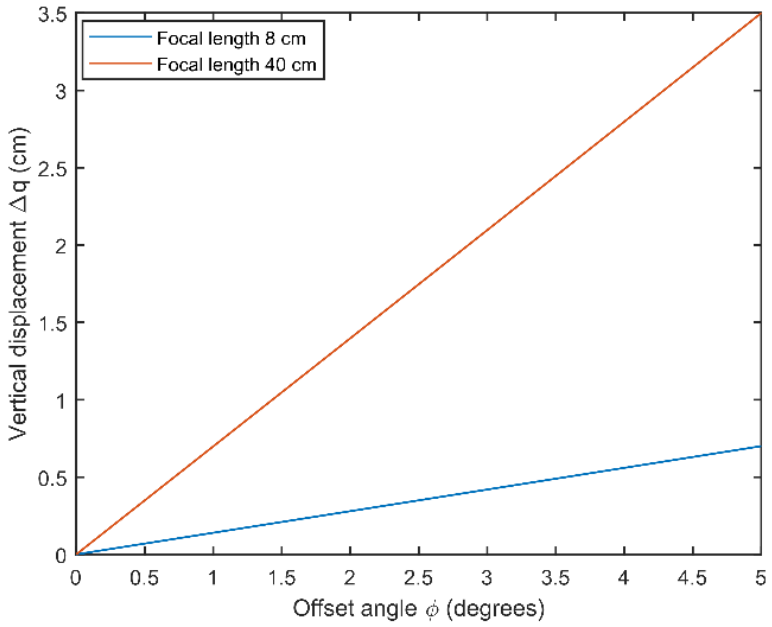

Fig. 3-7 Vertical displacement as a function of the offset angle for f of 8 and 40 cm.

where D_L is the lens diameter. For f of 8 cm and a lens diameter of 20 cm, θ_L will be 51.34º. The commercially available MMF has a maximum NA of 0.5, which corresponds to an acceptance angle of 30º, which is smaller than θ_L thus resulting in large coupling losses.

Fig. 3-8 shows fibre-based coupling Rx arrangement where the incoming light from the lens is coupled directly onto the multi-mode fibre array placed along the focal plane of the lens. Light from the MMF array is coupled into the PDs using a collimator and a photonic lantern. The EGC technique is used for signal processing. Note that, Δq is large and would require more fibres for coupling light compared with the cascading lens, see Fig. 3-6.

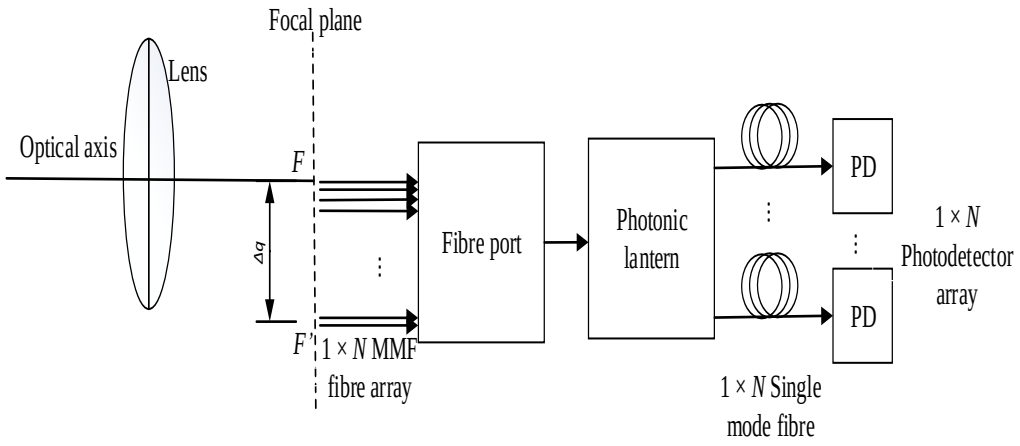

Fig. 3-8 Schematic block diagram of a single lens setup.

3.4 Results and Discussion

The proposed systems are numerically simulated using the parameters given in Table 3-1. Fig. 3-9 depicts the geometric loss h_g as a function of the transmission distance between the BS and the train for the first five fibre based Txs as shown in Fig. 3-2. From Fig. 3-9 it is observed that, h_g is the lowest and highest for the fibres 5 and 1, respectively with the attenuation difference of ~6 dB. Note, beams 1 and 5 have the lowest and highest divergence angles of 5 and 37.5 mrad, using (3.13) and the parameters shown in Table 3-1, the transmit power for each beam as a function of transmission range for the G2T under the fog condition with a visibility of 0.5 km is depicted in Fig. 3-10. The coupling losses between the lens and MMF is assumed to be 2 dB. It is assumed that the photonic lantern has a bundle of seven single mode fibres [64] connected to the PDs. The average multimode to single mode loss per fibre is 0.56 dB, which gives a total loss of ~4 dB for seven fibres. Therefore, the total loss for L_{Misc} is 6 dB. As shown in Fig. 3-10 the beams display minimum transmits power levels of 9.2, 9.69, 9.182, 5.6, and 4.3 mW are for Txs 1 to 5, at the transmission distances of 25, 37.5, 55, 75, and 95 m, respectively. The intersections on each beam depict the 2 m overlap between two beams as shown in Fig 3-2.

To mitigate the losses exhibited by the system, the maximum transmit power of each beam is considered as the transmit power required by each beam as shown in Table 3-1. Using commercially available beam splitters the optical power distributions for each fibre for the G2T communications are shown in Table 3-2. Note that, for an input power of 0 dBm at the EDFA the output power is 30 dBm, which corresponds to 1W. The total power required for fibres 1-5 is calculated to be 360 mW from Table 3-2. Similarly, for fibres 6-10, the optical power would be 360 mW. The cumulative power requirement for each BS is 606.8 mW, which is within the EDFA power limit.

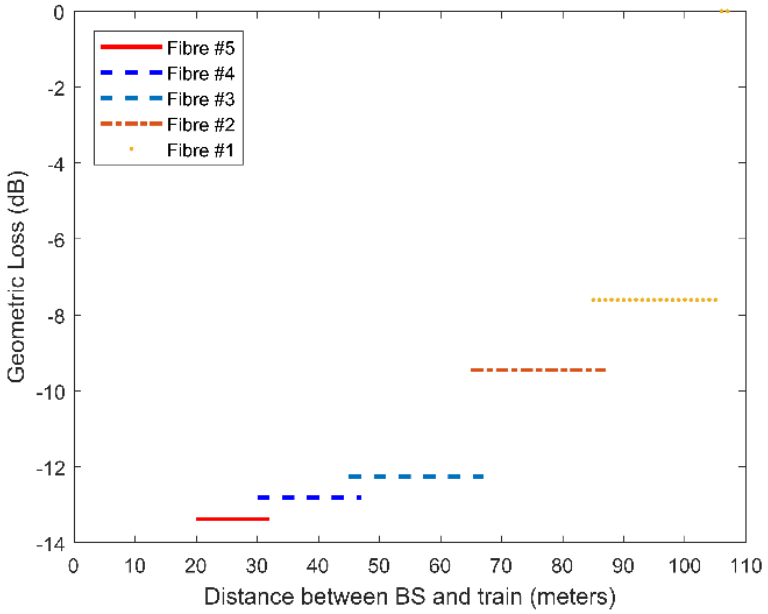

Fig. 3-9 The geometric loss versus the transmission distance for laser/fibre 1-5

Table 3-2 Power distribution for each fibre using commercially available splitters

TRANSMIT POWER				
Fiber number	Tilt angle (δ) (mrad)	Transmit power (mW)	Beam divergence (mrad)	Coverage length (m)
1, 10	24	54	5	20
2, 9	31	63	8	20
3, 8	45	63	15	20
4, 7	66.5	90	24	15
5, 6	100	90	37.5	10
BEAM SPLITTERS				
Splitting ratio		30:70 and 50:50		

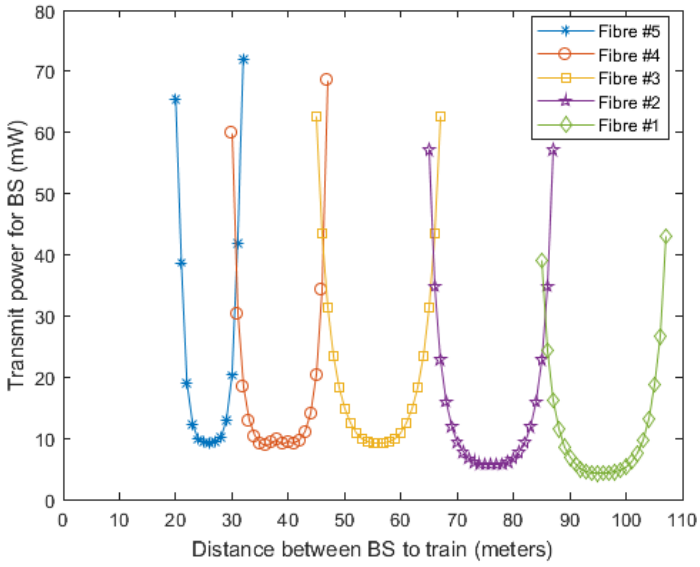

Fig. 3-10 The transmit power as a function of transmission distance for laser/fibre 1-5

The maximum geometric loss is contributed by fibres 1 and 10, which is -13.38 as depicted in Fig. 3-9. The average geometric loss contributed by fibres 1-5 is 11.10 dB. In contrast with single beam systems, the geometric loss is double the average geometric loss encountered by the sectorised BS approach as given in Table 3-3. As a result, the transmit power/laser for a single beam-based system with a coverage length of 55 m is more than twice that of the sectorised BS approach.

For moderate to strong turbulence the Gamma-Gamma turbulence model is a good fit for irradiance fluctuations encountered by the Rx's aperture [18]. For a point Rx (D = 0), C_n^2 = 9 × 10^{-13} $m^{-2/3}$ and a maximum link distance l_{link} of 100 m, the scintillation index is calculated to be 3.12 from (6), which categorises the turbulence to be moderate to strong turbulence. Since the Rx in this case averages the fluctuations resulting in reduced scintillation as compared to a point Rx, therefore the G2T link is considered as a lognormal fading channel. Using (3.8) simulations were carried to determine the BER performance of the link for weak turbulence range of σ_R^2 = 0.263 and C_n^2 = 9 × 10^{-13} $m^{-2/3}$, σ_R^2 = 0.1416 and C_n^2 = 5 × 10^{-13} $m^{-2/3}$ and σ_R^2 = 0.029 and C_n^2 = 1 × 10^{-13} $m^{-2/3}$ for the OOK-NRZ modulation format is depicted in Fig. 3-11. It is observed that, for all these cases the BER is below the FEC limit. The BER can be significantly improved by incorporating forward error correcting coding techniques [62]. Table 3-4 provides a comparison between the proposed system architecture and others reported in the literature.

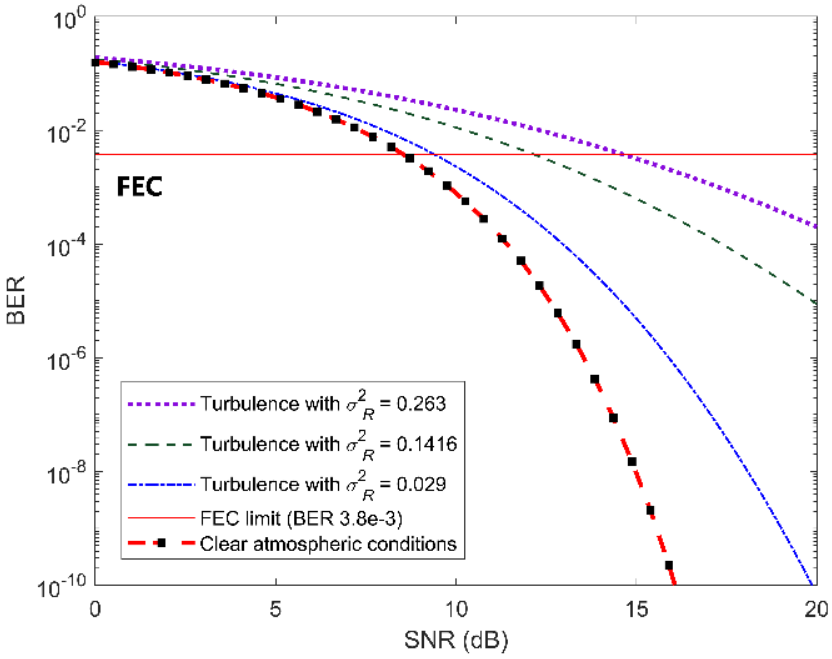

Fig. 3-11 Average BER as a function of SNR for σ_R^2 of 0.263, 0.1416 and 0.029

Table 3-3 Transmit power and geometric loss incurred for single beam systems

SINGLE BEAM SYSTEMS				
Coverage length per laser	Tilt angle (δ) (mrad)	Beam divergence (mrad)	Geometric loss (dB)	Transmit power (mW)
85	59.4	80.6	-22.7	1063
75	60.4	78.6	-22.3	964
65	61.6	76.1	-22.0	904
55	63.2	73.0	-21.4	783

Table 3-4 Comparison between different system architectures

System Architecture	Transmission data rate (Gbps)	Transmission wavelength (nm)	Distance between base stations (m)
RATE [16]	0.1	850	415
DRIVE [17]	1	850	887
Dual wavelength model [18]	1.25	850 and 1550	222
This work	**10**	**1550**	**210**

3.5 G2T Communications with Multiple Base Stations

In this section the concept of relayed FSO is presented in conjunction to sectorised base station concept discussed in previous sections to visualise G2T communication with multiple base stations. Section 1.2.3 highlighted that the solicitation, acknowledgement and binding messages contribute to the latency of the overall system. Minimising or eliminating these messages would further improve the handover. Consider the network architecture depicted in Fig. 3-13 which consists of of signal tapped from the backbone network via an access router (AR) serving a group of BSs on the ground connected to it. When a train passes from a BS to a successive BS connected to a different AR the transceiver on the train via a mobile router (MR) on board tries to establish a connection with the successive BS, which is termed as the link-layer handover. Note, MR sends a router solicitation message to the BS and the BS returns a router advertisement message to the MR, which signifies a successful link layer (L2) handover. The MR also sends a binding update message to the home agent, which in turn returns a binding acknowledgement message signifying the network layer (L3) handover at which point communications between the train and ground BS becomes available [54].

To mitigate L3 handover, a relayed FSO system is employed, which enables G2T communications and relays the same data to successive BSs. Two schemes are considered and analysed via numerical simulations which are all-optical amplify and forward (AOAF) and AF scheme with a 2R regenerator and OEO in terms of the bit error rate (BER) performance and communication distance attained.

3.5.1 Relayed FSO: System Architecture

The system architecture of the proposed link is described in Fig. 3-13, which comprises of a BS with a transceiver laser as a transmitter (Tx) and a relay node positioned along the rail trackside for a full duplex communication. Two receivers (Rxs) are mounted on the roof of the train to provide seamless connectivity. The BSs, which are placed 210 m apart as the coverage area Lcov for each BS is 210 m, transmit the received signal from the relays to the train [102]. The Tx1 is connected to an AR connected to the backbone fibre network. The laser is connected to the MR is installed on the train. The MR registers the home network prefix and care of address (CoA) with the home agent, which is connected to the backbone fibre network.

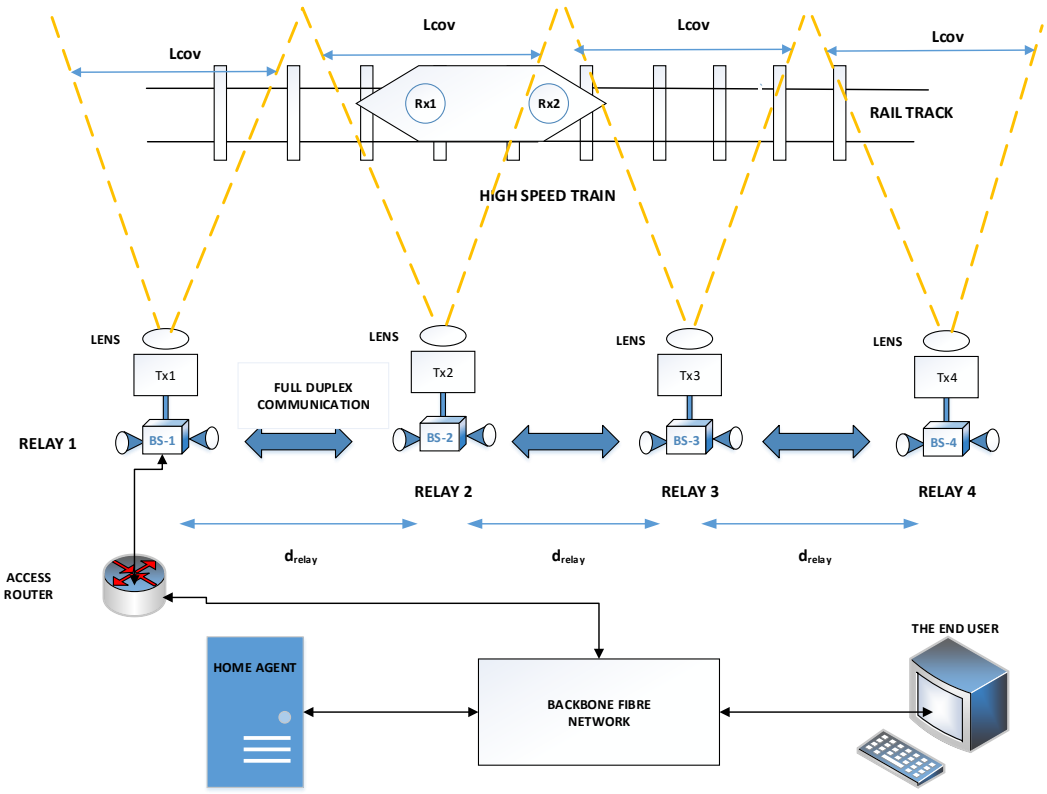

Fig. 3-12 System architecture for relay assisted ground-train communication

3.5.2 AOAF Scheme

Consider an AOAF system as depicted in Fig. 3.14 where an optical amplifier (Erbium doped fibre amplifier, EDFA) at each BS re-amplifies and re-transmits the received signal from the previous BS to the next BS. The received signal at each BS is given as [129]:

$$x_r^k(t) = hx_t^{k-1}(t) + n_b^k(t), \tag{3.18}$$

where $x_r^k(t)$ is the received signal at the *k*th BS, x_t^{k-1} is the transmitted signal at (*k*-1)th BS and n_b^k is the background noise and *h* is the channel gain contribution from turbulence and atmospheric losses. Transmitted signal from the *k*th relay is given by:

$$x_t^k(t) = \sqrt{G_k}x_r^k(t) + n_{\mathrm{ASE}}^k(t), \tag{3.19}$$

where, G_k is the amplifier gain, n_{ASE}^k amplified spontaneous emission (ASE) noise. Assuming that the signal, background noise, ASE noise and fading are all independent, the average optical signal to noise ratio (SNR) at the (*M*+1)th BS is given by [129]:

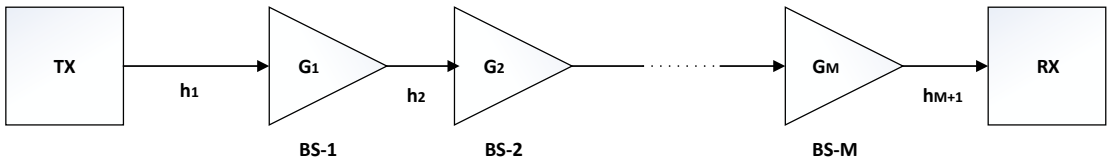

Fig. 3-13 The amplify and forward scheme.

$$\mathrm{SNR}^{M+1} = \frac{\left(\prod_{k=1}^{M} G_k h_k\right) h_{M+1} P_t}{\left(1 + \sum_{i=1}^{M} \prod_{k=i}^{M} G_k h_{k+1}\right) P_b + \left(h_{M+1} P_{\mathrm{ASE}}^{M} + \sum_{i=1}^{M-1} \prod_{k=i+1}^{M} G_k h_k h_{M+1} P_{\mathrm{ASE}}^{i}\right)}, \tag{3.20}$$

where, P_t is average transmit power from the BS, P_b is background radiation power, P_{ASE}^j is ASE noise for the *j*th amplifier at that BS. The background radiation can be computed as [129]:

$$\sigma_{bg}^2 = \frac{N_0}{2}, \tag{3.21}$$

where, N_0 is the noise power spectral density. Note that light from optical sources such as the sun, moon stars contribute to σ_{bg}^2 which is mentioned in equation 2.56. In this scenario, σ_{bg}^2 is modelled as an additive White Gaussian noise in space and time with zero mean and variance.

3.5.3 Optical 2R Regenerator

With reference to Fig. 3-15, the degraded optical pulse from a relay is fed to an EDFA, which amplifies the signal to a suitable level at the input of a highly non-linear fibre (HNLF). The amplified pulse is launched into HNLF where the pulse experiences spectral broadening due to SPM (self-phase modulation). A narrow-band optical band-pass filter (OBPF) is used as a pulse shaping element to carve out the desired signal at the output.

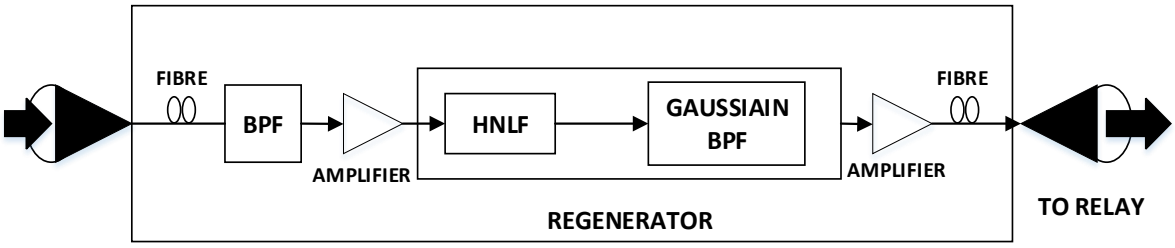

Fig. 3-14 Mamyshev 2R regenerator

The spectral broadening is given by [72]:

$$\Delta\omega_{\text{SPM}} = \Delta\omega_0 \left(\frac{2\pi}{\lambda}\right) n_2 I_p L, \tag{3.22}$$

where, $\Delta\omega_0$ is the initial bandwidth of the signal pulse, λ is the wavelength, n_2 and L are the refractive index and the length of the HNLF, respectively and I_p is the optical intensity of the pulse. Given that, the OBPF has a bandwidth of ω_f and is shifted by $\Delta\omega_{\text{shift}}$, the critical pulse intensity is given by [18]:

$$I_{cr} = \frac{2\Delta\omega_{\text{shift}}}{\Delta\omega_0\left(\frac{2\pi}{\lambda}\right)n_2 L}, \tag{3.23}$$

From 3.22, the extent of spectral broadening can be controlled and from 3.23, the minimum input pulse intensity can be calculated. Please note that, the SPM based 2R regenerator is compatible for the return to zero (RZ) modulation format and preferred due to its simple implementation. For the OOK-RZ data format the BER is given as [130]:

$$\text{BER}_{\text{RZ-OOK}} = \frac{1}{2}\text{erfc}\left(\frac{\sqrt{\text{SNR}}}{2}\right). \tag{3.24}$$

3.5.4 OEO Regenerator

Fig. 3-16 provides a schematic diagram of a OEO-based repeater with forward error correction (FEC) coding. The received optical signal is converted to an electrical signal using a photodiode followed by a clock recovery (for obtaining the timing information from the signal) and a decoder module. The decoder counts the parity bits from the decoder to monitor performance. The FEC block performs error correction on the signal prior to being used for intensity modulation of the laser source via the current driver module [130].

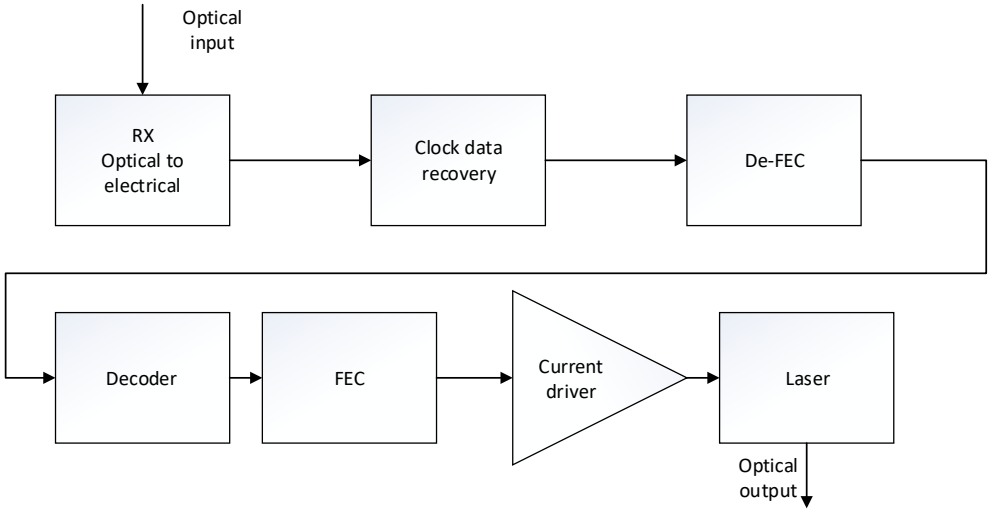

Fig. 3-15 OEO schematic diagram.

3.5.5 Numerical Simulations Results

In this section numerical simulation has been performed to evaluate the performance of amplify and forward (AF) relaying system and AF with the combination of 2R regenerator and an OEO regenerator. In all cases, the data rate considered is 10 Gbps with RZ-OOK, λ = 1550 nm, Latm is -17.5 dB/km with a visibility of 800 m and the inter relaying distance is 210 m [102]. The average transmit power P_{tx} is estimated from 3.9. The noise contribution from the background radiation is assessed from 3.21 and the amplifier noise contribution is estimated from the noise figure given in Table 3-1. Since the relaying distance is less than 1 km long, Rytov variance from 3.7 is 0.114 for $C_n^2 = 1\times10^{-13}$ m$^{-2/3}$, which falls under the weak turbulence regime therefore not considered in this work. For optical regenerating relays a bandpass filter with 80 GHz followed by HNLF with an attenuation of 0.88 dB/km and length of 500 m is considered. The optical bandpass filter has a central wavelength of 1551 nm and

a bandwidth of 3 nm [72]. For OEO regenerators Reed-Solomon FEC (RS(255,233)) is considered for its low latency, low complexity and low power consumption [132].

3.5.5.1 *AOAF with Relay*

Consider an AOAF, where the communication distance attained from Fig. 3-17 is 1022 m within the FEC limit of 3.8×10^{-3}. The gross communications distance for the stations-to-BS is taken as 840 m, which is 4 hops as the 5th hop's is above the FEC limit.

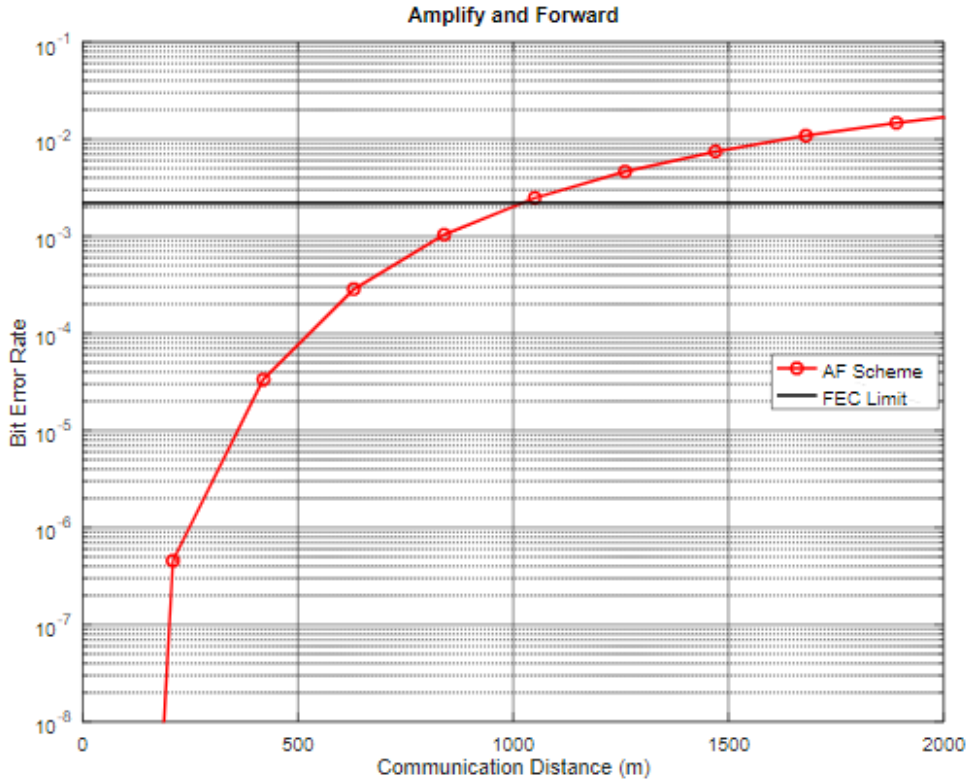

Fig. 3-16 The BER as function of the transmission distance for the AF relaying for stations-to-BS communications.

Accumulation of the background noise in the AF scheme limits the transmission range in BS-to-BS links. Note, for the 5th BS, the signal will need to be tapped from the backbone network via an AR. This would result in both the network and physical layers handover for the train passing from the 4th to the 5th BS.

3.5.5.2 *AF scheme with a 2R regenerator and OEO*

Consider an optical AF scheme with a 2R regenerator situated at the 3rd BS and with the OEO located at the 6th BS. The 2R regenerator placed in the 3rd BS will extend the link span from 4 hops (840 m) to 6 hops (1260 m) as shown in Fig. 3-18.

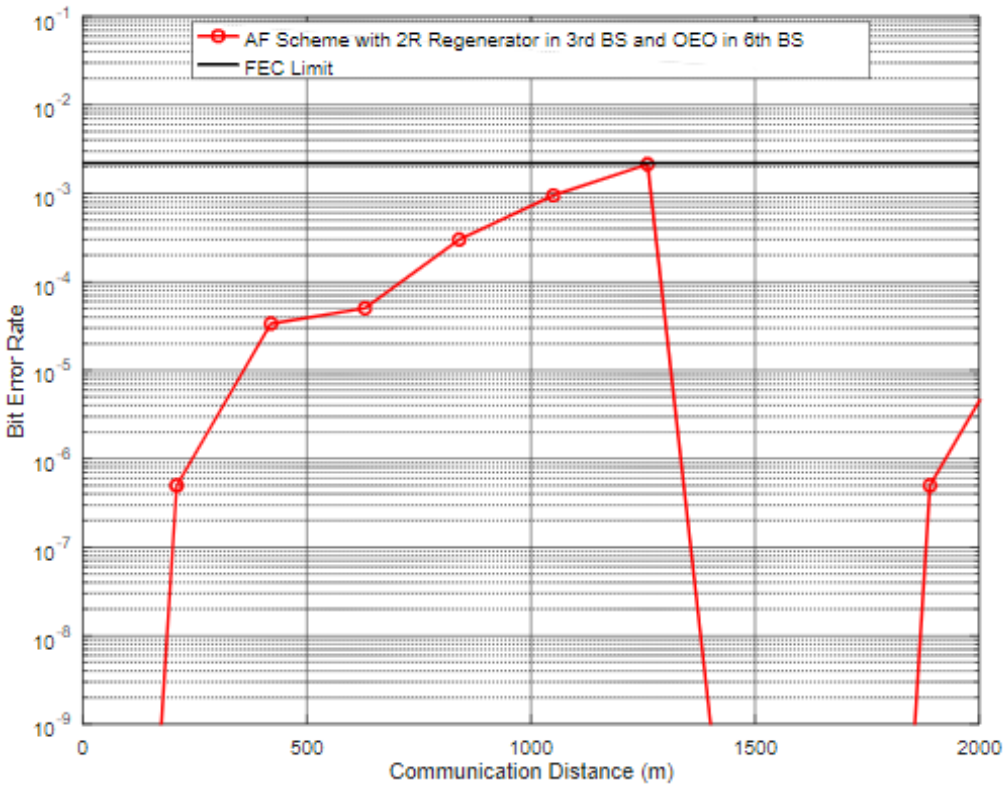

Fig. 3-18 The BER vs. transmission distance for the AF scheme with 2R regenerator at 3rd BS and OEO at 6th BS.

The OEO at the 6th BS employs error correction, thus resetting in error free transmission as in [133], which is then amplified and forwarded to the next BS. As compared with the AF scheme, the AF in tandem with the 2R regenerator and OEO requires no new AR to be installed as the scheme is contiguous, practically eliminating network layer handover.

3.5.6 Key Takeaways

Numerical results from the previous sections indicate that AF scheme with a 2R and OEO regenerator provides better performance than the all-optical AF scheme due to the fact that error correction can only be done at the electrical domain. However, cost of implementation needs to be factored in while considering installation of the G2T architecture discussed in this section. The cost of implementation is directly proportional to the number of OEO conversions required [129] which makes the OEO solution less attractive as compared to its RF counterparts. This may substantially increase the initial system installation even if deployed on a small scale. Also, only a small fraction of the network can be successfully reproduced in the lab which casts uncertainty on some of the "on-field" parameters which may not be accurately reproduced in the lab. Extra system margin needs to be allocated to mitigate these uncertainties. Furthermore, OEO nodes are not bit-rate transparent. These nodes are stuck to a particular bi-rate and cannot process signals at other rates. These nodes are not protocol transparent as well meaning that they are tied to handling signals of a particular protocol. Taking these factors into

consideration it would be prudent to implement collimated beam PAT communication system with a modified network protocol discussed in chapter 5.

3.6 Summary

In this chapter, a sectorised multi-laser coverage system was proposed to mitigate the geometric loss experienced by single beam systems. We have also proposed two Rx architectures for the deployment on the train. We have described duplex communication between the train and the BS. Power budget analysis was carried out under heavy fog conditions to determine the transmit power required for each fibre at the BS. As the ground-train communication system employs large apertures at the Rx, the fluctuations are averaged over the Rx resulting in reduced scintillation as compared to a point Rx. Due to the effect of aperture averaging, our analysis considers log-normal distribution as a good approximation for weak turbulence regimes. Numerical simulations were carried out to determine the ground-train communications performance under turbulence of varying strength. In all cases, the system BER was found to be below the FEC limit. At the FEC limit. the SNR penalties observed for σ_R^2 = 0.263, 0.1416, and 0.029 are 0.7, 3.28, and 5.83 dB, respectively. Two schemes were analysed in the presence of atmospheric attenuation (17 dB/km) namely AOAF and AF scheme with a 2R regenerator. The total communication distance attained by AOAF is 840 m due to noise accumulation at each hop which results in signal tapped from the backbone network via an access router causing network handover delay along with physical layer handover delay. AF scheme with a 2R regenerator and OEO provides contiguous communication distance without having to install any new access routers eliminating network handover delay.

Chapter 4: Turbulence Mitigation using Forward Error Correction

4.1 Introduction

In outdoor environments, one of the key issues in the intensity modulated/direct detection FSO communication system is the degradation of the links' performance due to the atmospheric conditions such as fog, snow, smoke, and turbulence. The latter, which is due to the inhomogeneity of the temperature and pressure in the atmosphere, results in local variations of the refractive index along the propagation path, leads to the intensity and phase fluctuations of the propagating optical bean, thus leading to fading and beam spreading, and ultimately the link failure [65]. Note that, deep fading can result in severe communication outages. Therefore, to address the limitations of FSO links, several mitigation techniques have been proposed in the literature, such as the aperture averaging [66-68], spatial diversity [69,70], relay assisted communications [71,72], adaptive optics [73], and coding [74]. The requirements of synchronisation, high processing complexity and costly implementation are some of the downsides of the proposed mitigation techniques as outlined in [75].

In FSO systems, the channel is assumed to be slowly time variant (i.e., slow fading), where the transmission parameters can be adjusted using the CSI. This is provided via a feedback link at the Tx to improve the quality of the link. In addition, to mitigate turbulence induced fading and, therefore, improve the links' BER performance, various error control coding schemes have been proposed and investigated. FSO links with space-time, repetition, and rate-less coding schemes have been reported in the literature [76-78]. A practical scheme of adaptive transmission has been considered to mitigate turbulence induced fading in FSO links to adjust parameters such as the transmit power, code rates and modulation schemes using the CSI received via the feedback path [75]. Variable and adaptive transmission schemes have been reported in literature [79-83]. In [74], a power allocation scheme in a WDM FSO link was proposed to mitigate atmospheric attenuation. In [80], an adaptive modulation and coding scheme for FSO was proposed where the CSI was estimated at the Rx and relaying back to the Tx via an RF feedback path. In [81], a rate adaptive on-off keying FSO link was practically demonstrated using an optimised punctured low density parity check (LDPC) code. In [82], a delay and quality of service aware adaptive modulation scheme was proposed for a coherent dual-channel optical wireless communication system under Gamma-Gamma (GG) turbulence. In [83], an adaptive transmission system for optical wireless communication using computer-vision techniques is proposed. The computer vision-based multi-domain cooperative adjustment (CV-MDCA) captures on-line images of the communication channel. Features from the processed images are extracted and compared with standard sample attributes to measure the channel quality index (CQI). The cooperative controller then adjusts various transmission parameters such as encoding, modulation, equalisation, power allocation and information format based on the CQI.

As part of linear codes, polar codes, which are defined using a generator matrix in a recursive manner, offer lower encoding and decoding complexity (i.e., $O(N\log_2(N))$, where N is the code length [84] and O is the big-O notation indicating the performance of the algorithm, and have been used in several applications including relay transmission, multiple access channels, quantum key distributions [84-85], etc. In the context of FSO communications, the performance of polar codes over the turbulence channel was analysed in [86]. The authors have proposed a CSI evaluation scheme that is utilised to calculate the LLR using a 2000-bit pilot sequence, which is the soft-input to the polar decoder. It was experimentally determined that, under weak turbulence, polar codes performed better than LDPC codes, and under moderate and strong turbulence using Monte-Carlo simulations, polar codes outperformed LDPC. In [88], the performance of a deep learning-based neural network is investigated under the turbulence regime. Under fixed turbulence conditions, the decoder performance is reported to be stable. In [88], the concept of the polar coded multiple input multiple output (MIMO) FSO communications system is introduced to combat turbulence induced fading. The MIMO-polar coded system using a successive cancellation list decoder (SCL) offered an improved net coding gain when compared with LDPC with and without spatially correlated fading scenarios.

For finite code lengths, LDPC and turbo codes perform better than polar codes, for which several decoding schemes [89, 90] have been proposed to improve the error correcting performance at the cost of increased complexity. In this chapter, we determine the optimum code-rate R for the scintillation indices σ_I^2 of 0.12, 0.2, and 0.31 for the SC decoder and compare its performance with the SCL decoder under weak turbulence in terms of the BER with the assumption that, the channel state information at the Rx is not known. We show that, for σ_I^2 of 0.12 and 0.2, the SCL decoder offers coding gains of 2.5 and 0.3 dB, respectively for the same R over SC decoder, and for σ_I^2 of 0.31, the SC decoder demonstrates improved performance with a coding gain of 2.5 dB for the same R over SCL decoder.

4.2 Channel Polarization Concept

Channel polarisation process involves implementing a transformation which generates N synthetic channels each of which transmit a single bit with a different reliability or probability of decoding correctly. If N approaches a large number some of these synthetic channel's probability of decoding reaches either 0 or a 1 resulting in channels of extreme capacities. Consider a channel W which takes X_1 and X_2 to provide an output Y_1 and Y_2. Consider U_1 and U_2 as inputs to X_1 and X_2 as follows [91]:

$$X_1 = \mathbf{U_1} \oplus \mathbf{U_2}\,, \tag{4.1}$$

$$X_2 = \mathbf{U_2}\,, \tag{4.2}$$

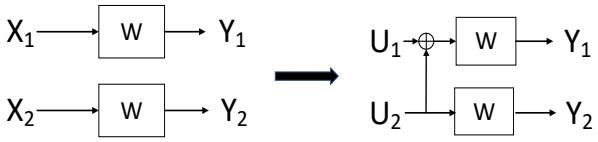

where, $\oplus$ is the XOR operator.

Consider *W* to be a binary erasure channel (BEC). BEC is defined as:

- X_N is decoded unsuccessfully with a probability of **p**. The bit is erased in this case.
- X_N is decoded successfully with a probability of **(1-p)**.

In the analysis of the above mentioned 2 bit channels, two possibilities arise namely:

1. Reconstruction of outputs with X_1 decoded successfully: $\mathbf{W^-: X_1 \rightarrow (Y_1, Y_2)}$.
2. Reconstruction of the outputs with X_2 decoded successfully: $\mathbf{W^+: X_2 \rightarrow (Y_1, Y_2)}$.

4.2.1 $\mathbf{W^-: X_1 \rightarrow (Y_1, Y_2)}$

The W^- channel attempts to reconstruct outputs from the input received on the U_1 channel. Following possibilities exist:

- Probability of Both X_1 and X_2 are decoded successfully: $\mathbf{(1-p)^2}$
- Probability of X_1 erased and X_2 decoded successfully: **p(1-p)**
- Probability of X_2 erased and X_1 decoded successfully: **p(1-p)**
- Both the bits erased: $\mathbf{p^2}$

The possibilities are succinctly captured in terms of U_1 and U_2 in equation 4.3

$$(Y_1, Y_2) = \begin{cases} (\mathbf{U_1} \oplus \mathbf{U_2}, \mathbf{U_2}) & (1-p)^2 \\ (\text{Erasure}, \mathbf{U_2}) & p(1-p) \\ (\mathbf{U_1} \oplus \mathbf{U_2}, \text{Erasure}) & p(1-p) \\ (\text{Erasure}, \text{Erasure}) & p^2 \end{cases}. \quad (4.3)$$

In this scenario, U_1 can only be extracted in the first scenario as U_2 is decoded successfully. All the other scenarios fail to extract U1, therefore the probability of U_1 decoded successfully is $(1\text{-}p)^2$. The probability of U_1 and U_2 decoded unsuccessfully is $\mathbf{p(1-p) + p(1-p) + p^2 = 2p\text{-}p^2}$. Assuming BEC erasure probability of 0.3, the success probability of W- channel is 0.49 and erasure probability is 0.51. In this

case W^- bit channel is a worse channel than the BEC channel. Therefore, a known value is sent across this channel, or this channel is "frozen" to a known value.

4.2.2 W^+: $X_2 \rightarrow (Y_1, Y_2)$

The W^- channel attempts to reconstruct outputs from the input received on the U_2 channel. Since the value on the W^- channel is clamped to a known value as the performance of the channel is worse than BEC, U_1 in this case is known to us. Following possibilities exist:

- Probability of Both X_1 and X_2 are decoded successfully: $\mathbf{(1-p)^2}$
- Probability of X_1 erased and X_2 decoded successfully: $\mathbf{p(1-p)}$
- Probability of X_2 erased and X_1 decoded successfully: $\mathbf{p(1-p)}$
- Both the bits erased: $\mathbf{p^2}$

The possibilities are summarised in equation 4.4 below:

$$(Y_1, Y_2, \mathrm{U}_1) = \begin{cases} (\mathbf{U_1} \oplus \mathbf{U_2}, \mathbf{U_2}, \mathbf{U_1}) & (1-p)^2 \\ (\mathrm{Erasure}, \mathbf{U_2}, \mathbf{U_1}) & p(1-p) \\ (\mathbf{U_1} \oplus \mathbf{U_2}, \mathrm{Erasure}, \mathbf{U_1}) & p(1-p) \\ (\mathrm{Erasure}, \mathrm{Erasure}, \mathbf{U_1}) & p^2 \end{cases}. \quad (4.4)$$

In this scenario, U_2 can be determined in the first two possibilities as X_2 was decoded successfully. In the third possibility, as X_1 is decoded successfully, U_2 can be determined from equation 4.1 as U_1 is known, therefore the probability of U_1 and U_2 decoded unsuccessfully is $\mathbf{p^2}$. The probability of U_1 and U_2 decoded successfully is $\mathbf{p(1-p) + p(1-p) + (1-p)^2 = 1-p^2}$. Assuming BEC erasure probability of 0.3, the success probability of W^+ channel is 0.91 and erasure probability is 0.09. This process can be extended to create *N* synthetic bit channels which would provide channels close to erasure probability of 0. Fig. 4-1 shows the polarisation of a BEC channel of erasure probability of 0.5 to achieve 1024 synthetic bit channels with their associated erasure probabilities. The plot depicts the result of 10-level polarisation in which the good bit-channels lie at the bottom of the plot and some bit-channels with erasure probability close to 1. In simple terms the polarisation technique takes in *N* independent copies of binary-input discrete memoryless channel to spit out *N* synthetic bit-channels. These channels transmit a single bit with different probability (see Fig. 4-1) of being decoded properly. If *N* is large (say 1024 bits long) the mutual information of the synthetic channels thus produced would be either close to 1 (noisy channel) or 0 (noiseless channel). The noisy channels are "frozen" which means that

no useful information is passed through the channel and the noiseless channels are chosen to pass data through them [93].

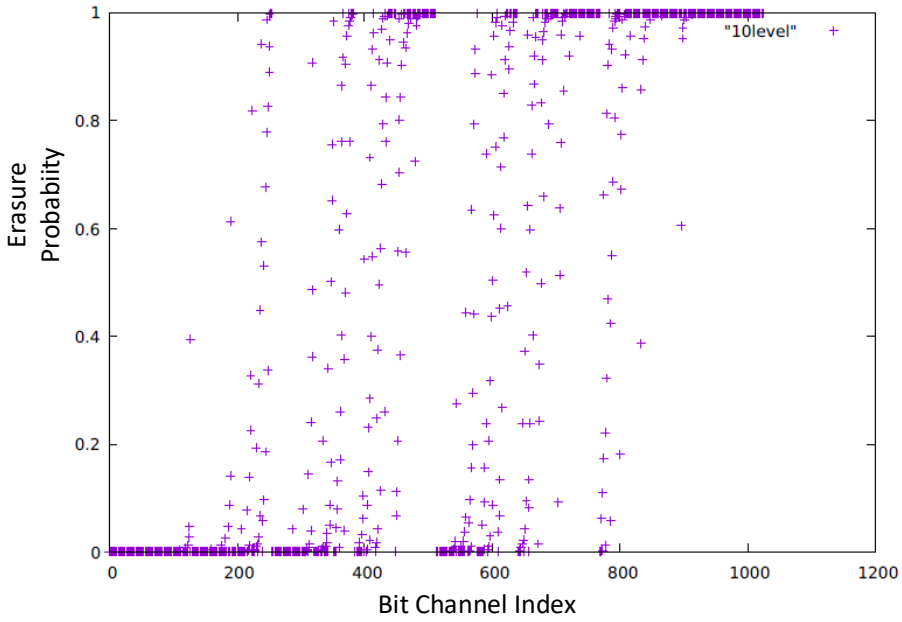

Fig. 4-1 Erasure probabiities for 1024 bit channels over BEC 1/2 channel.

4.3 Polar Code Encoding

Polar codes are capacity achieving codes introduced by Arikan [92]. It provides a low-complexity method to construct polarized channels, where a fraction of noiseless channels tends to the capacity of binary-input discrete memoryless channel (B-DMC). The channel polarization concept discussed in [92] consists of a transformation, which produces N synthetic bit-channels from N independent copies of B-DMC. The synthetic channels are polarized meaning that bits with different probability of decoding are transmitted. The design of (N, K) polar codes involves the generation of input vector $\mathbf{u} = [u_0, u_1, u_2, \ldots u_{N-1}]$ by assigning K information bits to the K most reliable channels. The remaining N-K bits form the frozen set and do not carry any information. The codeword $\mathbf{d} = [d_0, d_1, d_2, \ldots, d_{N-1}]$ is computed as [93]:

$$\mathbf{d} = \mathrm{u} \times \mathbf{G_N}, \tag{4.5}$$

where $\mathbf{G_N}$ is the $N \times N$ channel transformation matrix given by:

$$\mathbf{G_N} = \mathbf{G_2}^{\otimes n}, \tag{4.6}$$

where $\mathbf{G}_2 = \begin{bmatrix} 1 & 0 \\ 1 & 1 \end{bmatrix}$ is the transform kernel for 2-bit, $n = \log_2(N) = 1, 2, 3 \ldots$, N is the code length, and $\otimes$ is Kronecker product. Fig. 4-2(a) depicts the encoding mechanism of (8, 4) polar code, where the frozen bit set belongs to the bit positions 0, 1, 2, and 4 of **u**. The message bits are placed in bit positions 3, 5, 6, and 7 of **u**. Using (4.5) and (4.6), **u** is encoded to obtain the codeword **d**.

$$\begin{bmatrix} d_0 \\ d_1 \\ d_2 \\ d_3 \\ d_4 \\ d_5 \\ d_6 \\ d_7 \end{bmatrix} = \begin{bmatrix} 1 & 1 & 1 & 1 & 1 & 1 & 1 & 1 \\ 0 & 1 & 0 & 1 & 0 & 1 & 0 & 1 \\ 0 & 0 & 1 & 1 & 0 & 0 & 1 & 1 \\ 0 & 0 & 0 & 1 & 0 & 0 & 0 & 1 \\ 0 & 0 & 0 & 0 & 1 & 1 & 1 & 1 \\ 0 & 0 & 0 & 0 & 0 & 1 & 0 & 1 \\ 0 & 0 & 0 & 0 & 0 & 0 & 1 & 1 \\ 0 & 0 & 0 & 0 & 0 & 0 & 0 & 1 \end{bmatrix} \begin{bmatrix} u_0 \\ u_1 \\ u_2 \\ u_3 \\ u_4 \\ u_5 \\ u_6 \\ u_7 \end{bmatrix}. \tag{a}$$

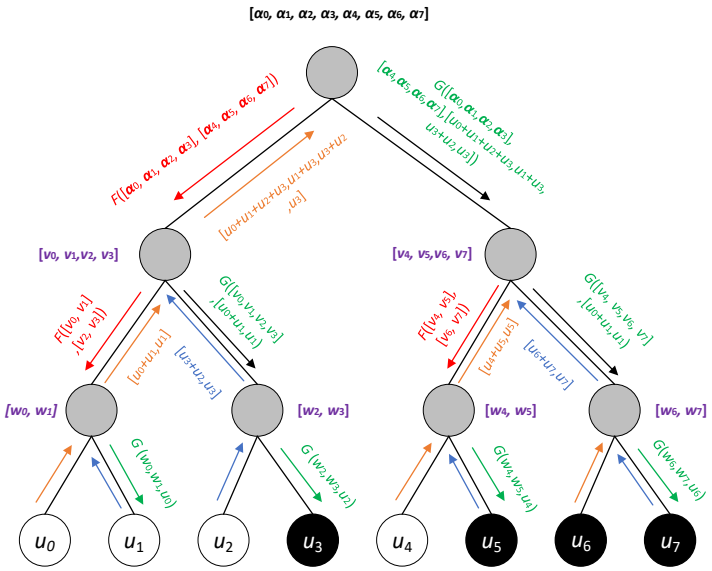

(b)

Fig. 4-2 (a) (8,4) polar encoding mechanism with frozen bits highlighted in blue, and (b) its corresponding decoder tree.

4.4 Polar Decoding

4.4.1 Successive Cancellation Decoder

The SC decoder, which is the most common in polar code, operates as a depth-first binary tree search., see Fig. 4-2(b), where each sub-tree is represented as a constituent node. The white and black nodes represent the information and frozen bits, respectively, whereas the grey nodes represent a concatenation of two constituent nodes. More specifically, the Rx observes **y** and estimates the elements of **u**. The decoder finds a sub-optimal solution by maximizing the likelihood via a greedy one-time-pass through the tree. The LLR α of each received codeword is passed down from the parent node to the child node, as shown in Fig. 4-2(b). Hard-decision estimated β are sent from the child nodes to the parent node. The left branch messages α_l are computed according to the *F* function using the min-sum approximation as given by [94]:

$$\begin{aligned}\alpha_l[i] = & F\left(\alpha[i], \alpha\left[i+\frac{N}{2}\right]\right) \\ & \approx \operatorname{sgn}(\alpha[i])\operatorname{sgn}\left(\alpha\left[i+\frac{N}{2}\right]\right)\min\left|\left(\alpha[i], \alpha\left[i+\frac{N}{2}\right]\right)\right|. \end{aligned} \tag{4.7}$$

The right branch messages α_r are calculated using the *G* function as follows:

$$\alpha_r[i] = G\left(\alpha[i], \alpha\left[i+\frac{N}{2}\right], \beta_l[i]\right) = \alpha_v\left[i+\frac{N}{2}\right] - (2\beta_l[i]-1)\alpha_v[i]. \tag{4.8}$$

For each codeword received, each node in the tree receives alpha and sends α_l (represented as in red arrows) to the successive node, receives β_l (represented by orange arrows), calculates and sends α_r (represented in blue) based on β_l. After receiving β_l and β_r, β is sent from the node to its parent node. β is computed as:

$$\beta[i] = \begin{cases} \beta_l[i] \oplus \beta_r[i], & \text{when } i < \frac{N}{2} \\ \beta_r\left[i-\frac{N}{2}\right], & \text{otherwise} \end{cases}, \tag{4.9}$$

where $\oplus$ refers to XOR operation and in this context is referred to as *combine* operation. When a leaf node is encountered, the estimated bit is given as:

$$\hat{u}[i] = \begin{cases} 0, & \text{if } i \in \mathcal{F} \text{ or } \alpha[i] \geq 0 \\ 1, & \text{otherwise} \end{cases}. \tag{4.10}$$

where $\mathcal{F}$ represents the frozen bit set. A SC list decoder was proposed in [95] as an improvement over the SC decoder in terms of error correction capability.

4.4.2 Successive Cancellation List Decoder

SCL decoding, which converts the greedy one-time-pass search of SC decoding into a breadth-first search, follows the same algorithm as SC decoding until the bit information estimation stage at the leaf nodes. For each estimate at the leaf node, both 0 and 1 are considered. This results in a list of $2L$ candidate codewords out of which L-codeword is removed based on the path metric, which is computed for each candidate codeword as [96]:

$$\mathrm{PM}_{i_l} = \begin{cases} \mathrm{PM}_{i-1_l}, & if\ \ \hat{u}_{i_l} = \frac{1}{2}\left(1 - \mathrm{sgn}(\alpha_{i_l})\right) \\ \mathrm{PM}_{i-1_l} + \ |\alpha_{i_l}| & \text{otherwise,} \end{cases} \tag{4.11}$$

where l is the path index and $\hat{u}_{i_l}$ is the estimated bit i in l. Note that, the L-path with the lowest PM will survive.

4.5 Log-Likelihood Ratio Computation for On-Off Keying

For OOK, the transmitted symbol is defined as:

$$x(t) = \begin{cases} 0, \ m(t) = 0 \\ 1, \ m(t) = 1 \end{cases}, \tag{4.12}$$

where m(t) is the message bits. From Baye's rule, we have:

$$P[x(t) = 0|\ y(t)] = \frac{P[y(t)|x(t) = 0]P[(x(t) = 0]}{P[y(t)]} \tag{4.13}$$

$$P[x(t) = 1|\ y(t)] = \frac{P[y(t)|x(t) = 1]P(x(t) = 1]}{P[y(t)]}. \tag{4.14}$$

For the AWGN channel, the received signal and the conditional probability are as given by, respectively [97]:

$$y(t) = \begin{cases} 1 + n(t), & \text{if } x(t) = 1 \\ n(t), & \text{if } x(t) = 0 \end{cases} \tag{4.15}$$

$$P[y(t)|x(t) = \tau] = \frac{1}{\sqrt{2\pi\sigma}} e^{\frac{-[y(t)-\mu_\tau]^2}{2{\sigma_\tau}^2}}, \tag{4.16}$$

where μ_τ and σ_τ are the mean and standard deviation for τ = 0, 1. From (4.13-16) α per bit is computed as:

$$\alpha = \ln\left[\frac{P[y(t)|x(t) = 0]}{P[y(t)|x(t) = 1]}\right] = \frac{1 - 2.y(t)}{2{\sigma_n}^2}. \tag{4.17}$$

From a practical standpoint, the calculation of the exact LLR following a stochastic model is quite complex [97]. Computation of LLRs could prove to be costly in terms of the computation complexity, hardware area and memory at the channel output [98,101]. In [99-101], computation of the approximate LLR methods were proposed. In this work, the LLRs for the FSO system is approximated as:

$$\alpha \approx 1 - 2 \cdot y(t). \tag{4.18}$$

Using Monte-Carlo simulations, the BER performance for the link with the SC decoder, given that the noise power is known at the Rx (i.e., true LLR values), and the SC decoder with the approximated LLR as per (4.18) for the AWGN channel is depicted in Fig. 4-3. It is observed that, the decoder performance using the LLR approximation is only slightly inferior to the SC decoder with the true LLR values of 0.2 dB measured at the BER of 10^{-5}, thus resulting in no significant deterioration in the BER performance.

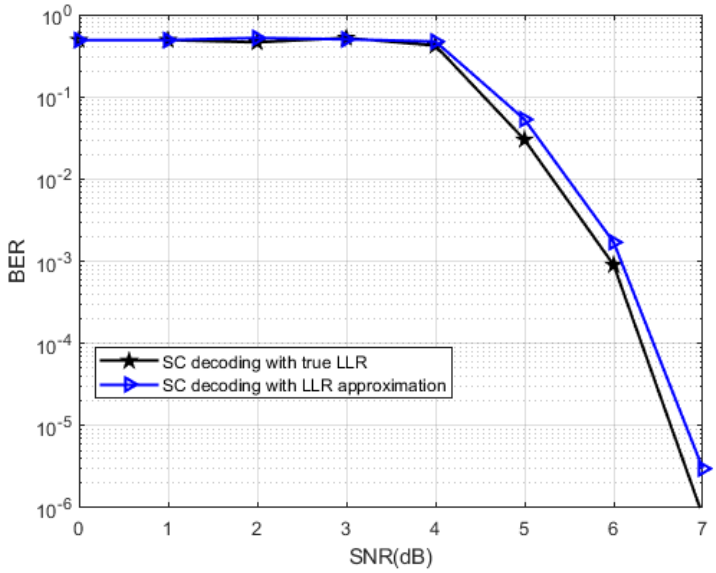

Fig. 4-3 BER performance of true LLR with approximated LLR using the SC decoder.

4.6 System Model

As shown in Fig. 4-3, a random message bit sequence ***m*** in the non-return to zero OOK format is applied to the polar code encoder to generate a fixed length codeword ***d*** with N of 1024-bits for intensity modulation of the optical source. The channel follows log-normal and GG distributions for $\sigma_I^2 \leq 0.3$ and > 0.3, respectively. Following transmission over the free space channel the codeword ***y*** is received at the optical Rx. Using (4.18) the LLR of received signal ***y*** is computed and decoded using the SC/SCL decoder to obtain $\boldsymbol{m}_{est}$. Although, narrow transmit beams are preferred in FSO links, for short-range FSO links, wide divergence angle light sources are highly desirable to ease the alignment requirement and therefore compensate for the pointing loss at the cost of increased geometric loss [5]. Typically, the beam divergence is in the range of 2-10 mrad for the non-tracking systems, which translates to a beam spot of 2-10 m for a 1 km link. In this work, we have assumed a beam with a wide divergence for ground-to-train communications as described in [102], which is practical, therefore offsetting the pointing loss at the cost of increased geometric loss [103]. However, for a point-to-point long range FSO link, misalignment must be considered.

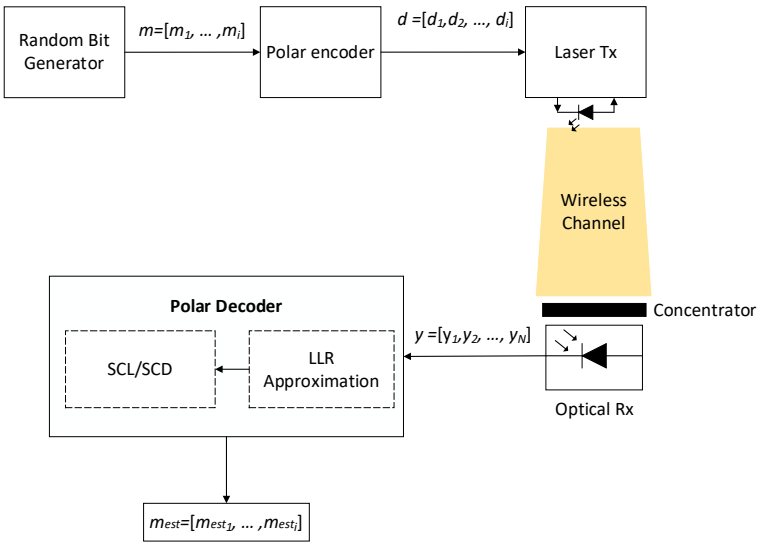

Fig. 4-4 A system block diagram for the proposed scheme

From a practical system's perspective, adaptive coding could be considered as a prudent approach to mitigate turbulence/scintillation experienced by the FSO link. The practical implementation of the proposed system can be carried out using purpose-built modules or FPGA, which will involve using the RF link for the feedback signal on channel state information. Alternatively, the adaptive coding part could be readily implemented using software defined radio (SDR), see Fig. 4-4. In the SDR-based Tx, the message bits are encoded using an adaptive Polar encoder, which adjusts the code rate based on the strength of the turbulence estimated by the CSI estimate block. The CSI is estimated by determining the variance (scintillation index) of the fluctuating optical intensity of a modulated red laser transmitted from the receiver side. The resulting signal from the adaptive encoder is fed to the USRP (Universal Software Radio Peripheral) Tx which is modulated onto an RF carrier. The RF carrier is directly modulated and transmitted across the FSO channel using a laser driver.

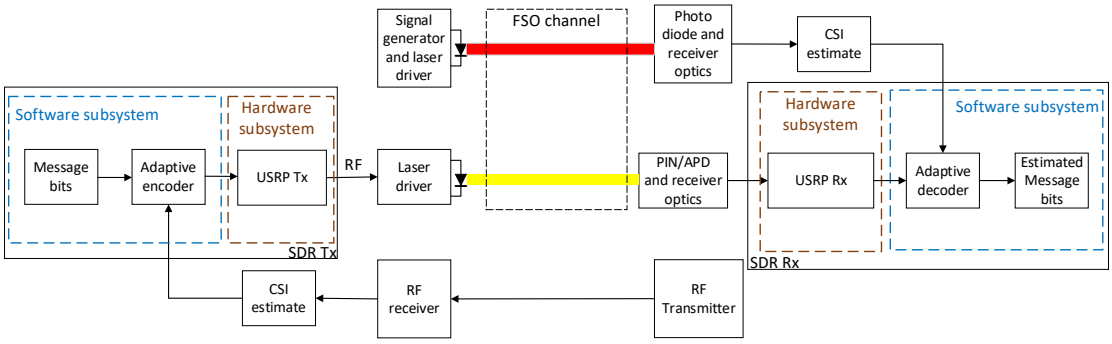

Fig. 4-5 System block diagram for adaptive coding using SDR.

4.7 Results and Discussion

The objective is to determine the optimum code rate for the weak turbulence regime, which maintains the BER at 10^{-9} with the 95% confidence limit for each scintillation index mentioned in Table 1. The amount the bits required with the 95% confidence limit is given by [104]:

$$N_{\text{bits}} = \frac{-\ln(1 - \text{Confidencelimit})}{\text{BER}}. \tag{4.15}$$

The OOK data stream, polar encoder, decoder, and the turbulence channel are implemented in C++ (see Appendix A). Using Monte-Carlo simulation, the optimum code rate under the weak and moderate turbulence regimes was determined utilizing the system parameters provided in Table 4-1, and the results of the simulation are described in Table 4-2.

Table 4-1 System parameters

PARAMETER	VALUE
Codeword length	1024
Iteration	$\frac{3 \times 10^6}{R}$
N_{bits}	3×10^9
BER confidence level	95%
Target BER	10^{-9}
Scintillation index σ_I^2	0.12, 0.2, 0.31

Table 4-2 Results of Monte-Carlo Simulation

σ_I^2	MESSAGE BITS TRANSMITTED	MSG BITS/FRAME	R
0.12	3×10^9	615	0.6
0.2	3×10^9	345	0.33
0.31	3×10^9	209	0.2

In each iteration, 1024-bit codewords are generated by the polar encoder as described in section 4.3 for a specific *R* and transmitted over a LN/GG turbulence channel for a range of scintillation indices provided in Table 4-1. The received bit stream is decoded and the BER is evaluated $\frac{3\times10^6}{R}$ times to estimate the BER with a 95% confidence level. To determine the optimum *R* for each scenario, an initial *R* of 0.5 was used. The simulation was terminated, and *R* was decremented by 0.1~0.05 once the simulation reached 100 errors. The decrement in *R* depends on the number of iterations needed to reach

100 errors. Note that, for each trial and the error scenario, a total of N encoded bits were generated. If no errors were detected, R was incremented by 0.05. Based on Monte-Carlo simulation results, a performance comparison between SC and SCL decoders are demonstrated for σ_I^2 = 0.12, 0.2, and 0.31 in Figs. 4-6 (a), (b), and (c), respectively. In all turbulence scenarios, SCL with cyclic redundancy check (CRC) is adopted with a list size of 4, a CRC length of 11 [89], and N of 1024. Also shown are the plots for the link with no coding and turbulence for reference. Under the turbulent condition, corruption of some bits allows for the message bits to be extracted from other uncorrupted bits. Because of this FEC works above a certain SNR level. This tendency is more pronounced in capacity achieving codes such as Polar codes. Error propagation problem is severe with the occurrence of multiple bit errors at lower SNR. At higher SNR, as the occurrence of bit errors are reduced and therefore the performance in terms of coding is improved, i.e., sharp fall in the BER plots for the links with coding, which is depicted in Fig. 5. In Fig. 4-6(a), for σ_I^2 = 0.1 the coding gain between uncoded OOK under turbulence with respect to SC decoder with R = 0.6 is 7 dB measured at the BER of 10^{-5}. The coding gain for the SC decoder with R = 0.7 is around 4 dB, which is 3 dB less than R = 0.6. SCL with R = 0.6 has improved performance with the coding gain of 6 dB, i.e., 2.5 dB improvement over the SC decoder for the same R measured at the BER of 10^{-5}.

For σ_I^2 = 0.2, see Fig. 4-6(b), the coding gain of 10 dB is observed between uncoded OOK under turbulence and the SC decoder for R = 0.33. The SC decoder with R = 0.5 show deteriorated performance compared with the case with R = 0.33 with a coding gain of 5 dB with respect to uncoded OOK under turbulence, 5 dB worse off than R = 0.33 as measured at the BER of 10^{-4}. The SCL decoder has an improved performance with a coding gain of 10.3 dB with respect to uncoded OOK under turbulence, 0.3 dB improvement over the SC decoder for the same R measured at BER of 10^{-6}.

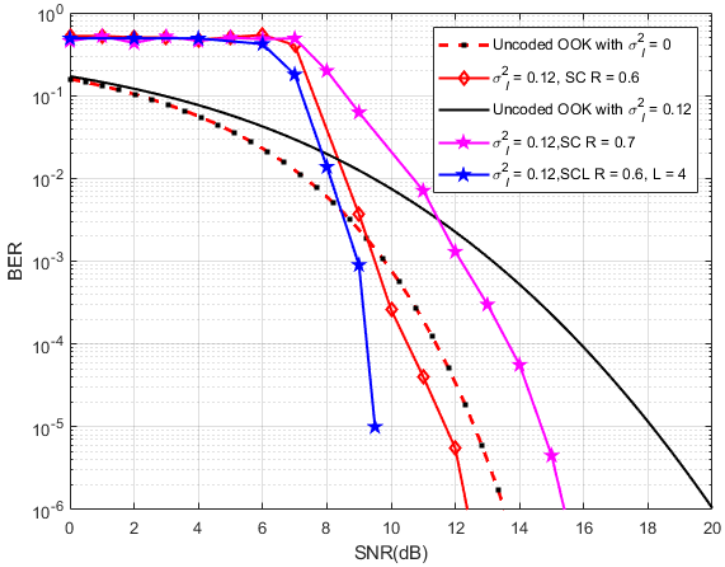

(a)

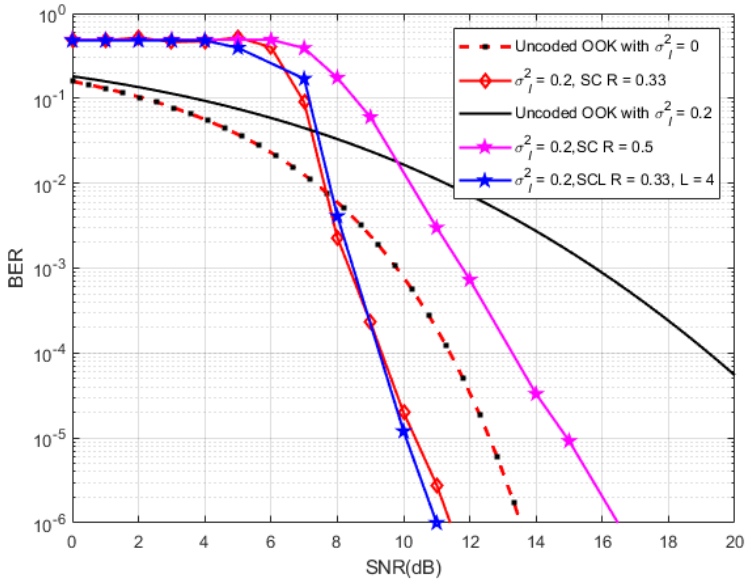

(b)

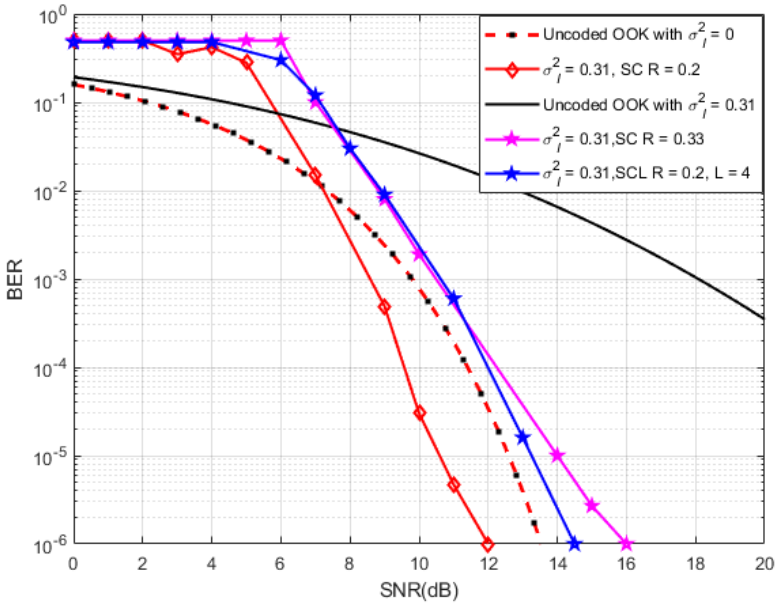

(c)

Fig. 4-6 BER performance as a function of the SNR for the link with SCL and SC decoders for σ_I^2: (a) 0.12, (b) 0.2, and (c) 0.31

For the case of σ_I^2 = 0.31 as shown in Fig. 4-6(c), the SC decoder with R = 0.2 has a coding gain of 13 dB with respect to the uncoded OOK under turbulence. The coding gain of 9 dB is observed for R of 0.3 with degradation of 4 dB compared with R = 0.2. Note, the SCL decoder offers lower performance compared with the SC decoder for the same R with a coding gain of 10 dB, i.e., 2.5 dB lower than the SC decoder.

4.8 Summary

This chapter investigated the robustness of polar codes in a FSO link under the weak turbulence regime assuming that the channel state information is not known at the receiver. The log-likelihood ratio for OOK modulation was derived and based on the derivation the optimum R required to attain a confidence limit of 95% for the BER of 10^{-9} for scintillation indices 0.12, 0.2, and 0.31 were carried out using Monte-Carlo simulations. Comparisons between the SC and SCL decoders were drawn in which for σ_I^2 of 0.1 and 0.2 the SCL decoder offered coding gains of 2.5 and 0.3 dB, respectively for the same R and for σ_I^2 of 0.3 the SC decoder demonstrated improved performance with a coding gain of 2.5 dB.

Chapter 5: Software Defined Network based Mobility Architecture for Ground to Train Communication

5.1 Introduction

One of the key challenges facing train-trackside communication is the handover rate and its management. The internet protocol (IP) was designed for the communication between static devices and therefore mobility protocols such as Mobile IPv4 (MIPV6), Mobile IPv6 (MIPV6), Proxy MIPv6, among many others, were developed to provide connectivity to mobile nodes [106]. Note that, the conventional mobility protocols do not guarantee the QoS during handovers, but rather focus on maintaining IP session connectivity [107]. SDN could provide an elegant solution for the handover management considering the QoS of the network. SDN is an emerging paradigm in which (i) the control plane is used for implementing the policy for handling network traffic; and (ii) the data plane, which forwards the packets based on the network policy, are decoupled thus allowing for an increased flexibility and simplification of network management [108]. In [109], an SDN-based network architecture for trains utilizing Wi-Fi as the backhaul connection and SDN for handover management was proposed. Simulation results indicate that for a throughput of 1 Mbps per user the average packet delays were 100ms and 1 s for the case of 50 and 100 users, respectively. In [110], a train-to-ground communication architecture based on the 5G wireless technology enabler SDN and multipath TCP was proposed. Simulations carried out in OpenNet, which is an open-source emulator running on top of mininet and ns-3, showed that the end-to-end latency of the system was within 60 ms with a reduced failover response time. In [111], an SDN-based flexible handover scheme was proposed considering the QoS requirements in terms of the loss and the delay sensitivity. The handover mechanism for different service flows was classified into 4 classes based on the QoS requirements. Simulation and analytical results showed efficient network management without any service degradation.

In this chapter, the following contributions to the existing state-of-the-art in the fields are introduced:

- An SDN-based mobility architecture is proposed for train-trackside FSO communication to provide seamless internet connectivity.
- A dedicated SDN testbed is designed and developed using the off-the-shelf components to evaluate the system performance in terms of the data throughput and the packet loss when a handover is initiated.
- The proposed SDN controller based FSO system is shown to offer seamless handover with the throughput of 250 Mbps.

The rest of the chapter is organized as follows: Sections 5.2 provide a description of SDN, OpenFlow protocol and Ryu Controller, section 5.3 provides a description of the experimental implementation of OpenFlow Protocol using Ryu controller, section 5.4 describes the SDN architecture placement of BSs, handover mechanism, and FSO link budget analysis of train-trackside communication. Section 5.5 describes the network architecture of train-to-trackside communication. Section 5.6 describes the experimental SDN testbed and system parameters considered for the experiment. along with the results of the experiments conducted.

5.2 Primer on Software-Defined Networking

The key concept of SDN is de-coupling of network control plane from the data forwarding plane, where a "controller" controls several network devices. The open networking [134] foundation endorses SDN as a cost-effective, manageable, and adaptable technology ideal for handling high bandwidth and dynamic nature of today's application demands. The key features of SDN are listed below [134]:

- **Programmability**: The control plane is directly programable removing the need to program and maintain vendor specific software. In simple terms, the software used to program the network device is vendor software agnostic which doesn't depend on any proprietary software.
- **Adaptable**: Network engineers can dynamically adapt to network traffic flow.
- Central Control: The Network intelligence is centrally controlled and managed; this gives a bird's eye view of the whole network.
- **Open standards-based protocol**: Provides a simple way to enforce network policies instead of configuring multiple vendor specific devices and protocol.

5.2.1 SDN Architecture

The SDN architecture depicted in Fig. 5-1 can be split into three planes namely, Data plane, Control Plane and Application plane.

- **Application Plane:** The application plane are programs in direct communication with the northbound interface (NBI) in accordance with the network requirements and expected network behaviour. This plane contains application logic with single or multiple NBI drivers.

- **Controller Plane:** The SDN Controller is a logically centralised unit responsible for (i) Interpret and transfer application requirements to the Datapaths and (ii) supply the application plane with switch statistics (which includes input/output packet details) and event information. Ryu is the preferred SDN Controller in this work.

- **SDN Datapath:** A Datapath connects the SDN controller to their Openflow switches/packet forwarding devices. Datapaths and creation of network bridges are implemented using Open vSwitch.

- **SDN Control to Data-Plane Interface (CDPI):** The SDN CDPI is the interface defined between an SDN Controller and an SDN Datapath, which provides at least (i) programmatic control of all forwarding operations, (ii) capabilities advertisement, (iii) statistics reporting, and (iv) event notification. One value of SDN lies in the expectation that the CDPI is implemented in an open, vendor-neutral and interoperable way. This interface is implemented using the OpenFlow protocol, which allows the communication between the Controller and the Datapaths and specifies how both should handle the information they share [134].

- **Northbound Interfaces:** NBIs provide an interface between application plane and the controller plane. REST API is the communication interface between the application and the controller plane in Ryu Controller.

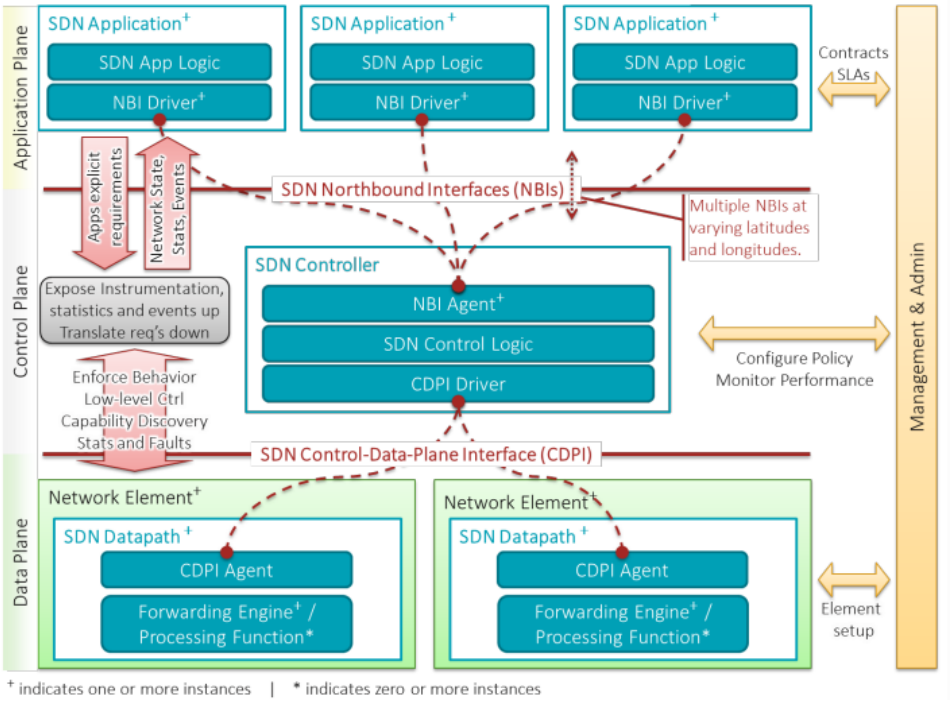

Fig. 5-1 SDN Architecture. Adapted from [134]

5.2.2 Openflow Protocol

OpenFlow protocol is a communication interface between the control and forwarding plane. The protocol enables access to control the forwarding plane network devices which includes but is not limited to routers and routers in physical (hardware) and virtual (hypervisor-based) platforms. The protocol is akin to CPU instructions which utilises basic primitives that an external software application can use to manipulate the devices in the forwarding plane.

OpenFlow protocol uses the concept of "**flows**" to distinguish traffic based on pre-defined "**match-rules**" that can be programmed using the SDN control software. This feature of OpenFlow provides granular control on network traffic responding to real-time changes at the application, user or session level which the current IP-based routing fails to provide as the network traffic between two endpoints must flow irrespective of different requirements.

At present OpenFlow is the only SDN protocol responsible for direct manipulation of network forwarding devices. OpenFlow-based switching can be applied to the current networks, both physical and virtual. Existing networks can support both OpenFlow and traditional forwarding mechanisms to ensure backwards compatibility. The key features of OpenFlow-protocol can be summarised as follows [134]:

- **Increased network reliability and security**: SDN makes it possible for IT to define high-level configuration and policy statements, which are then translated down to the infrastructure via OpenFlow. An OpenFlow-based SDN architecture eliminates the need to individually configure network devices each time an end point, service, or application is added or moved, or a policy changes, which reduces the likelihood of network failures due to configuration or policy inconsistencies. Because SDN controllers provide complete visibility and control over the network, they can ensure that access control, traffic engineering, quality of service, security, and other policies are enforced consistently across the wired and wireless network infrastructures, including branch offices, campuses, and data centres. Enterprises and carriers benefit from reduced operational expenses, more dynamic configuration capabilities, fewer errors, and consistent configuration and policy enforcement [134].

- More granular network control: OpenFlow‘s flow-based control model allows IT to apply policies at a very granular level, including the session, user, device, and application levels, in a highly abstracted, automated fashion. This control enables cloud operators to support multi-tenancy while maintaining traffic isolation, security, and elastic resource management when customers share the same infrastructure [134]**.**

5.2.3 OpenFlow Switch

In an SDN, switches act as forwarding devices with the SDN controller assuming responsibility of the control logic. OpenFlow is the communication protocol used to communicate between the controller and the networking device. An OpenFlow enabled switch contains a flow table and a group table as depicted in Fig. 5-2, and a communication channel to communicate with the controller. The "Flow tables" contain flow entries, where each entry consists of match fields, counters, and instructions for matching packets. The protocol can add, modify, or delete an entry from the flow tables in response to packets proactively. Matching is not restricted to the first flow table and may continue to additional flow tables. In the event of no matching packets, the packets are either dropped or a table miss entry flow would determine the path of the packets. Instructions in each flow entry contain actions. These actions may correspond to packet forwarding to a specified port or packet modification.

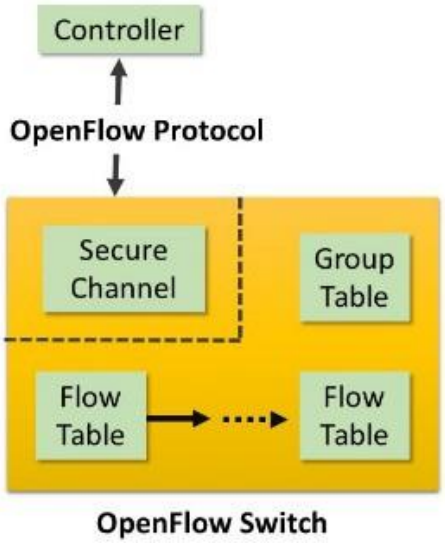

Fig. 5-2 OpenFlow Switch.

Instructions associated with each flow entry describe packet forwarding, packet modification or pipeline processing action. In pipeline processing the packets are further sent to succeeding tables with transfer of meta data as a medium of communication between tables [134].

5.2.4 OpenFlow Tables

A flow table comprises of flow entries. Each flow table contains [134]:

- **Match fields** to match against packets. These consist of the ingress port and packet headers, and optionally metadata specified by a previous table.
- **Priority** to indicate the matching precedence of the flow entry (higher numbers mean higher priority).
- **Counters** to update for matching packets.

- **Instructions** to modify the action set or pipeline processing.
- **Timeouts** to indicate the maximum amount of time or idle time before flow is expired by the switch. Each flow entry is configured with an *idle_timeout* and a *hard_timeout*. The *hard_timeout* causes the flow entry to be removed after the given number of seconds, regardless of how many packets it has matched. The *idle_timeout* causes the flow entry to be removed when it has matched no packets in the given number of seconds.
- **Cookie:** opaque data value chosen by the controller. May be used by the controller to filter flow statistics, flow modification and flow deletion, not used when processing packets. For example, the controller could choose to modify or delete all flows matching a certain cookie.

5.2.5 Matching

When a packet enters a OpenFlow switch, the switch looks up in the first table to identify instructions related to the packet. If there were no matches found, the switch then looks up in the same table for a "Table miss flow entry". If this flow doesn't exist, the packet is eventually dropped. In all other cases the packet is then processed according to the actions specified in the flow table. Matches can be performed on packet headers and/or on ingress ports. It is to be noted that the actions corresponding to the highest priority flow entry is executed. The counters associated with the flow entry is updated. Table 5-1 shows the match fields supported by OpenFlow 1.3 [134].

Table 5-1 OpenFlow Match Fields and Description

Match Field	Description
OXM_OF_ETH_DST	Ethernet destination MAC address.
OXM_OF_ETH_SRC	Ethernet source MAC address
OXM_OF_ETH_SRC	Ethernet type of the OpenFlow packet payload, after VLAN tags
OXM_OF_VLAN_VID	VLAN-ID from 802.1Q header. The CFI bit indicates the presence of a valid VLAN-ID, see below
OXM_OF_VLAN_PCP	VLAN-PCP from 802.1Q header.
OXM_OF_IP_DSCP	Diff Serv Code Point (DSCP). Part of the IPv4 ToS field or the IPv6 Traffic Class field.
OXM_OF_IP_ECN	ECN bits of the IP header. Part of the IPv4 ToS field or the IPv6 Traffic Class field.
OXM_OF_IP_PROTO	IPv4 or IPv6 protocol number
OXM_OF_IPV4_SRC	IPv4 source address. Can use subnet mask or arbitrary bitmask

OXM_OF_IPV4_DST	IPv4 destination address. Can use subnet mask or arbitrary bitmask
OXM_OF_TCP_SRC	TCP source port
OXM_OF_TCP_DST	TCP destination port
OXM_OF_UDP_SRC	UDP source port
OXM_OF_UDP_DST	UDP destination port
OXM_OF_SCTP_SRC	SCTP source port
OXM_OF_SCTP_DST	SCTP destination port
OXM_OF_ICMPV4_TYPE	ICMP type
OXM_OF_ICMPV4_CODE	ICMP code
OXM_OF_ARP_OP	ARP opcode
OXM_OF_ARP_SPA	Source IPv4 address in the ARP payload. Can use subnet mask or arbitrary bitmask
OXM_OF_ARP_TPA	Target IPv4 address in the ARP payload. Can use subnet mask or arbitrary bitmask
OXM_OF_ARP_SHA	Source Ethernet address in the ARP payload.
OXM_OF_ARP_THA	Target Ethernet address in the ARP payload.
OXM_OF_IPV6_SRC	IPv6 source address. Can use subnet mask or arbitrary bitmask
OXM_OF_IPV6_DST	IPv6 destination address. Can use subnet mask or arbitrary bitmask
OXM_OF_IPV6_FLABEL	IPv6 flow label.
OXM_OF_ICMPV6_TYPE	ICMPv6 type
OXM_OF_ICMPV6_CODE	ICMPv6 code
OXM_OF_IPV6_ND_TARGET	The target address in an IPv6 Neighbour Discovery message.
OXM_OF_IPV6_ND_SLL	The source link-layer address option in an IPv6 Neighbour Discovery message
OXM_OF_IPV6_ND_TLL	The target link-layer address option in an IPv6 Neighbour Discovery message.
OXM_OF_MPLS_LABEL	The LABEL in the first MPLS shim header
OXM_OF_MPLS_TC	The TC in the first MPLS shim header.
OXM_OF_MPLS_BOS	The BoS bit (Bottom of Stack bit) in the first MPLS shim header.
OXM_OF_PBB_ISID	The I-SID in the first PBB service instance tag.
OXM_OF_IPV6_EXTHDR	IPv6 Extension Header pseudo-field.

5.2.6 Table Miss Entry

Every flow table must support a table-miss flow entry to process table misses. The table-miss flow entry specifies how to process packets unmatched by other flow entries in the flow table, and may, for example, send packets to the controller, drop packets or direct packets to a subsequent table. The table-miss flow entry is identified by its match and its priority, it wildcards all match fields (all fields omitted) and has the lowest priority (0). If the table-miss flow entry does not exist, by default packets unmatched by flow entries are dropped (discarded). A switch configuration, for example using the OpenFlow Configuration Protocol, may override this default and specify another behaviour [134].

5.2.7 OpenFlow Protocol: Controller to Switch Messages

The OpenFlow channel connects the switch/networking device to the controller which configures and manages forwarding plane of the switch. The controller receives events from the switch and sends out packets from the switch. The OpenFlow switch protocol supports the following message types:

- **Controller-to-switch**: These messages are initiated by the controller to inspect and configure the switch.
- **Asynchronous messages:** These messages are updated to the controller by the switch. These messages contain information about network events and state changes occurring in the switch.
- **Symmetric messages**: Initiated by either the switch or the controller and sent without solicitation [134].

The following messages are exchanged between controller and switch:

- **Features:** This message initiated by the controller requests for identity and specification of the switch. The switch responds to this message by sending information about its capabilities. This communication happens upon the establishment of the OpenFlow channel.
- **Configuration:** The controller requests for configuration information from the switch. The switch responds to each individual query sent by the controller.
- **Modify State:** Modification of the flow table entries sent by the controller. Flow entries can be added, modified, or deleted.
- **Read-State:** Read-State messages collect configuration, network statistics and capabilities of the switch.
- **Packet-Out:** Forwarding of the packets accessed via the Packet-in messages to a specific port by the controller. This message should contain a list-actions to be applied in the sequence specified; if no actions are described then the packet is dropped.
- **Barrier**: Barrier request/reply messages are used by the controller to ensure message dependencies have been met or to receive notifications for completed operations [134].

- **Role-Request**: Role-Request messages are used by the controller to set the role of its OpenFlow channel, or query that role. This is mostly useful when the switch connects to multiple controllers [134].
- **Asynchronous-Configuration**: The Asynchronous-Configuration messages are used by the controller to set a filter on the asynchronous messages that it wants to receive on its OpenFlow channel, or to query that filter. This is mostly useful when the switch connects to multiple controllers and commonly performed upon establishment of the OpenFlow channel [134].

5.2.8 Asynchronous Messages

Asynchronous messages are sent by the switch to the controller without the controller explicitly requesting for information. These messages contain information related to packet arrival, switch state change or error. The four main asynchronous message types are [134]:

- **Packet-in:** Packets forwarded to the controller via the reserved CONTROLLER port due to either a table miss flow entry or a flow entry in the flow table.
- **Flow-Removed:** Communicate to the controller of removing a flow entry from the flow table.
- **Port-status:** Inform the controller of a change on a port. The switch is expected to send port-status messages to controllers as port configuration or port state changes. These events include change in port configuration events, for example if it was brought down directly by a user, and port state change events, for example if the link went down [134].
- **Error:** The switch can notify controllers of problems using error messages [134].

5.2.9 OpenFlow Channel Connections

The switch must be able to establish communication with a controller at a user-configurable (but otherwise fixed) IP address, using a user-specified port. If the switch knows the IP address of the controller, the switch initiates a standard TLS or TCP connection to the controller. Traffic to and from the OpenFlow channel is not run through the OpenFlow pipeline. Therefore, the switch must identify incoming traffic as local before checking it against the flow tables. When an OpenFlow connection is first established, each side of the connection must immediately send an OFPT_HELLO message with the version field set to the highest OpenFlow protocol version supported by the sender. Upon receipt of this message, the recipient may calculate the OpenFlow protocol version to be used as the smaller of the version number that it sent and the one that it received. If the negotiated version is supported by the recipient, then the connection proceeds. Otherwise, the recipient must reply with an OFPT_ERROR message with a ‘type’ field of OFPET_HELLO_FAILED, a code field of OFPHFC_COMPATIBLE, and optionally an ASCII string explaining the situation in data, and then terminate the connection. After the version has been negotiated, the controller issues a OFPT_FEATURES_REQUEST message which is answered with a OFPT_FEATURES_REPLY by the switch. This reply message contains the number

of tables and buffers (packets that can be buffered at once) supported by the switch and it's Datapath ID. Additionally, can contain a list of the capabilities of the switch, which can be:

- Flow statistics.
- Table statistics.
- Port statistics.
- Group statistics.
- Can reassemble IP fragments.
- Queue statistics.
- Switch will block looping ports.

This features message exchange is what is called OpenFlow Handshake. After the controller has received the message OFPT_FEATURES_REPLY, the controller usually queries the switch about its configuration parameters. The controller can set and query configuration parameters in the switch with the OFPT_SET_CONFIG and OFPT_GET_CONFIG_REQUEST messages, respectively. The switch responds to a configuration request with an OFPT_GET_CONFIG_REPLY message (but it does not reply to a request to set the configuration). Configuration messages carry the information inside a set of configuration flags. These flags indicate whether IP fragments should be treated normally, dropped, or reassembled. "Normal" handling of fragments means that an attempt should be made to pass the fragments through the OpenFlow tables [134].

5.2.10 Flow Table Modifications

Flow table modification messages can have the following types [134]:

- **Add:** Add a new flow (OFPFC_ADD). If the OFPFF_CHECK_OVERLAP flag is set, the switch must first check for any overlapping entries in the requested table. Two flow entries overlap if a single packet may match both, and both entries have the same priority. If an overlap conflict exists between an existing flow entry and the add request, the switch must refuse the addition and respond with an *ofp_error_msg* with OFPET_FLOW_MOD_FAILED type and OFPFMFC_OVERLAP code. For non-overlapping add requests, or those with no overlap checking, the switch must insert the flow entry in the requested table. If a flow entry with identical match fields and priority already resides in the requested table, then that entry, including its duration, must be cleared from the table, and the new flow entry added. If the OFPFF_RESET_COUNTS flag is set, the flow entry counters must be cleared, otherwise they should be copied from the replaced flow entry. No flow-removed message is generated for the flow entry eliminated as part of an add request; if the controller wants a flow-removed message it should explicitly send a delete request for the old flow entry prior to adding the new one.
- **Modify:** For modify requests (OFPFC_MODIFY or OFPFC_MODIFY_STRICT), if a matching entry exists in the table, the instructions field of this entry is updated with the value

from the request, whereas its cookie, *idle_timeout*, *hard_timeout*, flags, counters, and duration fields are left unchanged. If the OFPFF_RESET_COUNTS flag is set, the flow entry counters must be cleared. For modify requests, if no flow entry currently residing in the requested table matches the request, no error is recorded, and no flow table modification occurs.

- **Delete:** For delete requests (OFPFC_DELETE or OFPFC_DELETE_STRICT), if a matching entry exists in the table, it must be deleted, and if the entry has the OFPFF_SEND_FLOW_REM flag set, it should generate a flow removed message. For delete requests, if no flow entry currently residing in the requested table matches the request, no error is recorded, and no flow table modification occurs.

5.2.11 Brief Introduction to Open vSwitch

Open vSwitch (OVS) is virtualisation software used to create production quality switch platform that supports forwarding functionality manipulated by programmatic extensions. In this scenario we have used OVS to convert a Raspberry-Pi to an OpenFlow-Switch.

Open vSwitch is well suited to function as a virtual switch in VM environments. In addition to exposing standard control and visibility interfaces to the virtual networking layer, it was designed to support distribution across multiple physical servers. Open vSwitch supports multiple Linux-based virtualization technologies including Xen/XenServer, KVM, and VirtualBox. The bulk of the code is written in platform-independent C and is easily ported to other environments. The current release of Open vSwitch, as stated in their GitHub repository at https://github.com/openvswitch/ovs, supports the following features [134]:

- Standard 802.1Q VLAN model with trunk and access ports.
- NIC bonding with or without LACP on upstream switch.
- NetFlow, sFlow(R), and mirroring for increased visibility.
- QoS (Quality of Service) configuration, plus policing.
- Geneve, GRE, GRE over IPSEC, VXLAN, and LISP tunnelling.
- 802.1ag connectivity fault management.
- OpenFlow 1.3 plus numerous extensions.
- Transactional configuration database with C and Python bindings.
- High-performance forwarding using a Linux kernel module.

5.3 OpenFlow Protocol Implementation Using Ryu Controller

In this section, an FSO-SDN testbed was created using off-the-shelf components and a basic network monitor developed using Ryu controller.

5.3.1 Basics of SDN Development

A typical SDN architecture is composed of (i) applications– Communicating for resource requests or network-based information; (ii) controllers – For routing a data packet utilizing the information from (i) using a NBI API and with the networking devices using the southbound API; and (iii) networking devices – For receiving information from (ii).

In an SDN, switches act as forwarding devices with the SDN controller assuming responsibility of the control logic. OpenFlow is the communication protocol used to communicate between the controller and the networking device. An OpenFlow enabled switch contains a flow table and a group table as described in 5.2.3, and a communication channel to communicate with the controller as described in 5.2.9. The “Flow tables” contain flow entries, where each entry consists of match fields, counters, and instructions for matching packets. The protocol can add, modify, or delete an entry from the flow tables in response to packets or proactively. Matching is not restricted to the first flow table and may continue to additional flow tables. In the event of no matching packets, the packets are either dropped or a table miss entry flow would determine the path of the packets. Instructions in each flow entry contain actions. These actions may correspond to packet forwarding to a specified port or packet modification.

5.3.2 Experimental Testbed

The SDN testbed consists of 3 Raspberry Pi4, which act as OpenFlow switches (OF1, OF2 and OF3) as depicted in Fig. 5-3. OF3 apart from being an OpenFlow switch also acts as an SDN controller. The Raspberry-Pis is interconnected with each other using a USB 3.0 connection to the Ethernet adapter. The OpenFlow switches transmit packets through an established FSO link using small form factor (SFP) transceiver modules plugged into the media converters, which are connected to OF1 and the laptop. Each TP-Link SFP media converter (Model: MC220L) can support up to 1000 Mbps in Full-Duplex mode for TX and RX ports respectively. A SFP Laser (Model: SFP1G-ZX-55) is inserted in the media converter, which has a transmit power of 5 dBm while the receiver sensitivity is <-24 dBm.

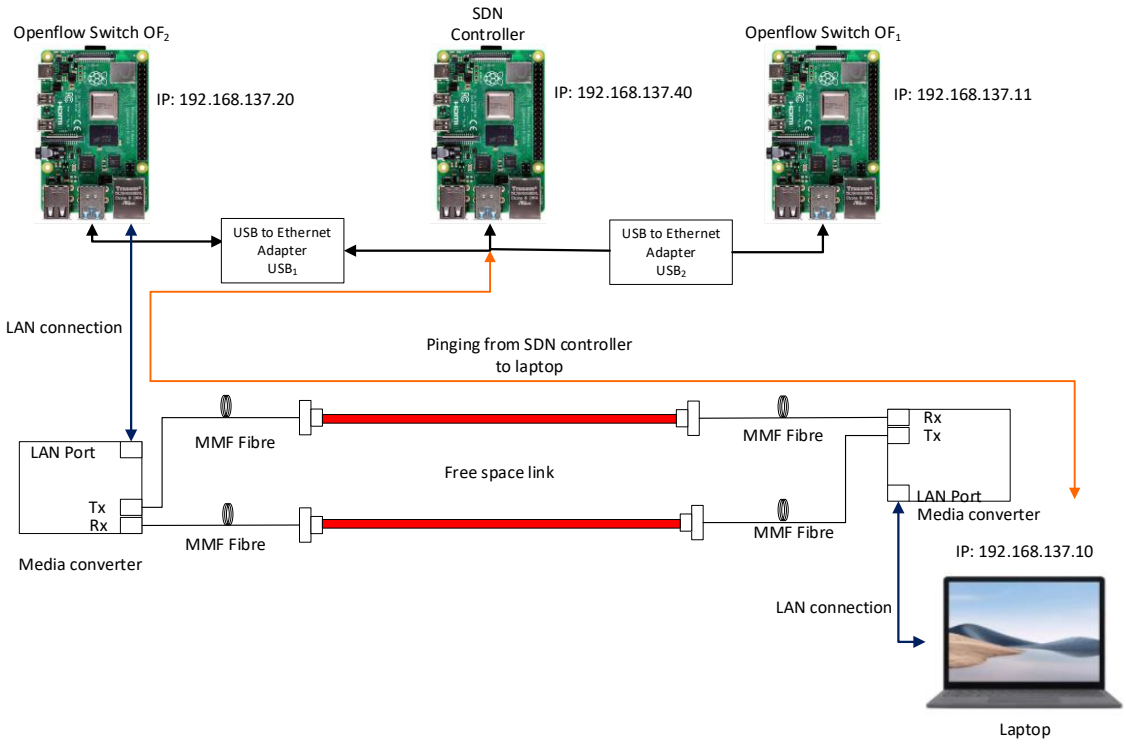

Fig. 5-3 SDN Testbed Schematic Diagram.

5.3.3 Network Monitor

The fso_traffic_monitor.py application inherits simple_traffic_monitor_13.py application provided by Ryu in which *the_flow_stats_reply_handler* method is overridden to monitor status of the FSO link. The application periodically (i.e., every second) collects information from the switches to record the number of packets transferred to a device's destination belonging to a particular data path ID. The experiment was run for a duration of 2 minutes.

A data path ID uniquely identifies a switch. A detailed description of the MAC address and data path of all the network devices and connected adapters and laptop is provided in Table 5-2. The laptop is pinged from OF1. When the link is obstructed, the application prints a warning to check the connection of the FSO link so that the link is up. This is accomplished by comparing the received and transmitted packets from the statistics collected from OF1 and OF2 with the data paths 11 and 22, respectively, see Fig. 5-3 (a). Upon detecting a mismatch, a warning message of "connection check" is printed on the screen. Note that, the received packet stops immediately once the obstruction is removed, and the link is up thus, resulting in the warning message being removed from the screen as shown in Fig. 5-3 (d). This is accomplished by comparing the received packets before and after the link are obstructed.

Table 5-2 Network Specifications of the SDN Testbed

Device name	Data path ID	MAC address	IP address
OF1	11	e4:5f:015f:04:85	192.168.137.40
OF2	22	e4:5f:015f:04:13	192.168.137.20
OF3	33	e4:5f:015f:04:bf	192.168.137.11
USB1	-	00:0a:cd:3e:1e:73	-
USB2	-	00:0a:cd:3e:1e:9d	-
Laptop	-	98:40:bb:37:17:b7	192.168.137.10

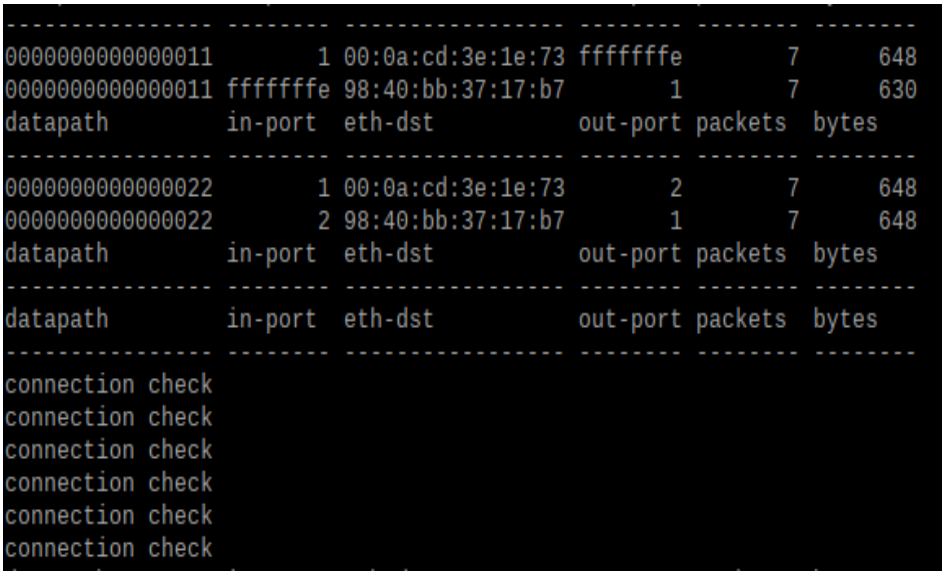

(a)

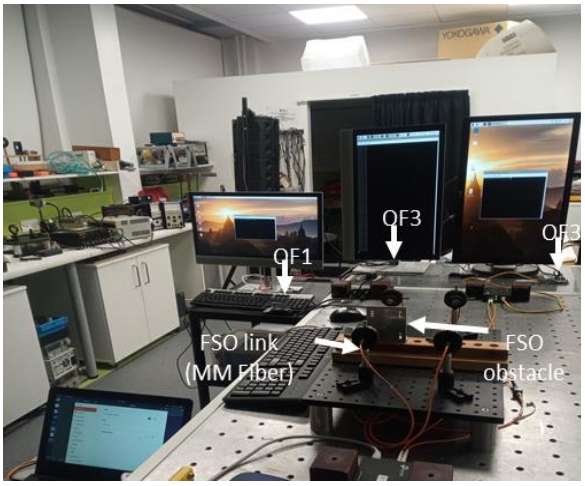

(b)

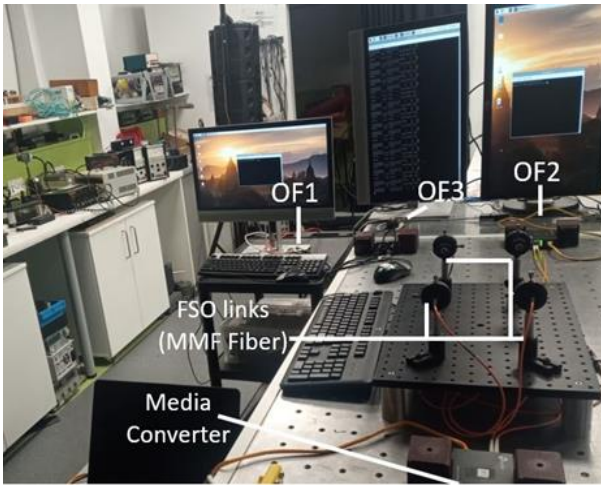

(c)

```
connection check
connection check
connection check
datapath         in-port  eth-dst           out-port packets  bytes
---------------- -------- ----------------- -------- -------- --------
0000000000000022        1 00:0a:cd:3e:1e:73        2       10      942
0000000000000022        2 98:40:bb:37:17:b7        1       12     1138
datapath         in-port  eth-dst           out-port packets  bytes
---------------- -------- ----------------- -------- -------- --------
0000000000000011        1 00:0a:cd:3e:1e:73 fffffffe       11     1040
0000000000000011 fffffffe 98:40:bb:37:17:b7        1       13     1218
datapath         in-port  eth-dst           out-port packets  bytes
---------------- -------- ----------------- -------- -------- --------
```

(d)

Fig. 5-4 Traffic monitoring system with and without obstruction:(a) SDN controller terminal output with obstruction (b) experimental setup with obstruction (c) setup without obstruction (d) terminal output without obstruction.

5.4 The Train-Trackside Communication Architecture

To provide high-speed internet services in trains, a dedicated trackside infrastructure consisting of multiple BSs connected using optical fibre cables is required. Analytical FSO models discussed earlier [56,57,58] employ a wide-angle optical beam to improve the coverage area and eliminate the need for pointing, acquisition, and tracking (PAT) systems. The problem regarding this approach is that the train and BSs would either require a bigger aperture to collect enough light or to increase the transmit power

of the transceivers placed at both BSs and on the train. As a result, we assume that the train-trackside communication is accomplished using PAT and beacon signalling. In [55], the authors identified some key problems regarding the communication approach in [54], which are as follows: (*i*) since the PAT system incorporates a wide-angle quadrant photodetector (QPD) for coarse tracking and a telescopic QPD for accurate tracking, multiple beacon signals from different BSs impinge on the QPD make it challenging to distinguish the position of the successive BS; and (*ii*) the handover time wasn't fast enough to provide a voice-over IP service, which demands a handover delay < 50 ms. To mitigate the first problem, BSs can be in a staggered manner as shown in Fig. 5-3. This allows for the QPD to distinguish the position of the beacon signal from the successive BSs. The backhauls for BSs are provided by the trackside cabling system using Duotrack® [112]. The Duotrack® cable is directly attached to the track using clamps, which can provide copper cable- and optical fiber- type services using a single cable line. Duotrack® cabling system can be deployed on both sides of the track, which is connected to the BS on the ground. The train utilizes two laser-based transceivers enabled with the PAT system onboard, which is connected to a mobile router (MR). The connection between the BSs and the train is established by tracking and pointing the laser beam in the direction of the beacon signal., see the link between the train and the BS2 in Fig. 5-3. Note, while the train is still connected to the BS2 it establishes a new connection to the BS3 by tracking its beacon signal. On establishing the connection with the BS3, the link with the BS2 is disconnected, thereby ensuring a seamless handover between BS2 and BS3. At any time during the train journey only a single communication link is maintained between the train and a BS.

The average speed of high-speed trains in the UK is about 210 km/hr [113]. Taking inspiration from Evo-Rail architecture [114], the spacing between two successive BSs is about 400 m as depicted in Fig. 5-3. Note that, the handover procedure is not initiated until the beacon signal from the successive BS is detected by the PAT system on the train. In this scenario, it is assumed that the beacon signal can be detected at a distance of 460 m from a BS. This means that the handover is initiated at 60 m away from the BS2. The transmit power requirement for a duplex communication link between the train and the BS can be determined by means of the link budget analysis, which is given by [115]:

$$P_{\mathrm{rx}}(\mathrm{dBm}) = P_{\mathrm{tx}} - lL_{\mathrm{atm}} - h_g - L_{\mathrm{Misc}} - L_M, \tag{5.1}$$

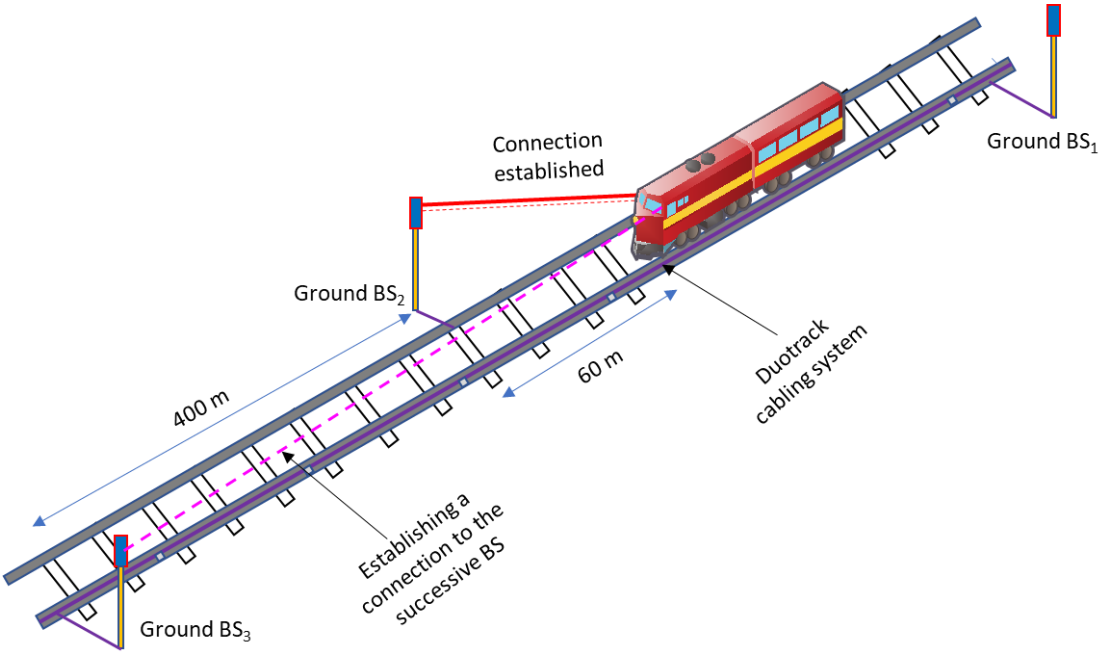

Fig. 5-5 The train-trackside communication system architecture.

where P_{rx} is the received optical power in dBm, l is the link length in km or the distance between the BS and the train at the time of handover, L_M is the link margin of the system, h_g is the geometric loss in dB, L_{Misc} is loss due to optics and fibre coupling losses in dB, P_{tx} is the transmit power in dBm, and L_{atm} is the atmospheric losses. To estimate P_{tx} from 5.1, first we need to determine P_{rx}, which is given by [116]:

$$P_{\mathrm{rx}}(\mathrm{dBm}) = \mathrm{NEP} + 5 \times \log(\mathrm{BW}) + \mathrm{SNR}_{\mathrm{Req}}, \tag{5.2}$$

where, NEP is the noise equivalent power of the receiver, which is commonly defined as the input signal power that results in an SNR of 1 dB for a bandwidth of 1 Hz. A lower NEP indicates a lower noise floor and a more sensitive detector. BW is the bandwidth of the signal and SNR_{Req} is the required signal to noise ratio requirement at the receiver for demodulation. OOK is the most reported modulation scheme for FSO systems due to its simplicity and is also adopted here. Table 5-3 summarizes the system parameters considered for calculating P_{tx} based on 5.1 and 5.2.

Table 5-3 System parameters for the link-budget analysis

Parameter	Value
NEP Data rate	-80 dBm/√Hz [117] 1 Gbps
BW	2 GHz
Bit error rate	10^{-3}
SNR_{Req}	11 dB
P_{rx} d_{rx}, d_{tx} θ_{div}	-22.5 dBm 0.8 m 0.5 mrad
h_g	-11.7 dB
V	500 m
L_{atm}	-34 dB/km
L_M	5 dB
l	460 m
P_{tx}	11.84 dBm
λ	1550 nm

5.5 Network Architecture

In the conventional IP protocol, IP addresses are statically assigned to the devices since they do not change locations. Mobile IP was envisioned to provide mobility support to devices [118]. In terms of train-trackside communications depicted in Fig. 5-6(a), when the train leaves its home network and tries to establish a connection with a foreign network, the mobile router (MR) on the train either acquires an agent advertisement message from the foreign agent (FA) to determine the MR's current point of attachment and care-of-address or could solicit messages to discover an agent on the network. The MR, FA and HA exchange registration messages associating the MR's home address with its care-of-address at the HA to enable datagram forwarding to its current location in the network. Assuming that in this case the MR uses foreign care-of-address, the registration process includes the following steps [119]:

1. The MR sends a request to the FA to start the registration process
2. The FA relays the registration request to the HA
3. The HA responds to the FA by either granting or denying the request
4. The FA relays the information passed on by HA to the MR.

The HA would intercept, and forward datagrams entitled to the FA after the MR has registered with the FA. The FA then forwards the datagrams to MR using the L2 technology [120]. Although mobile IP provides an elegant addressing solution with mobility support, it increases the network-layer handover time. The network-layer handover time increases with the moving speed of the mobile device as discussed in [121]. Fig. 5-6(b) describes the SDN-based mobility network design in which both HA and FA are replaced with Openflow (OF)- enabled switches controlled centrally by an SDN controller (SDNC). SDNC exerts direct control over the forwarding planes of the Openflow switches OF1 and OF2 using the Openflow protocol. While MR attempts to handover from the BS3 to the BS4, the controller installs flow entries (FE) onto OF1 and OF2 to enable packets being forwarded from the OF1 and OF2. This network design ensures that the latency created by exchanging registration messages as described is removed and the network latency is now dependent on the FE installation on the Openflow-enabled network device.

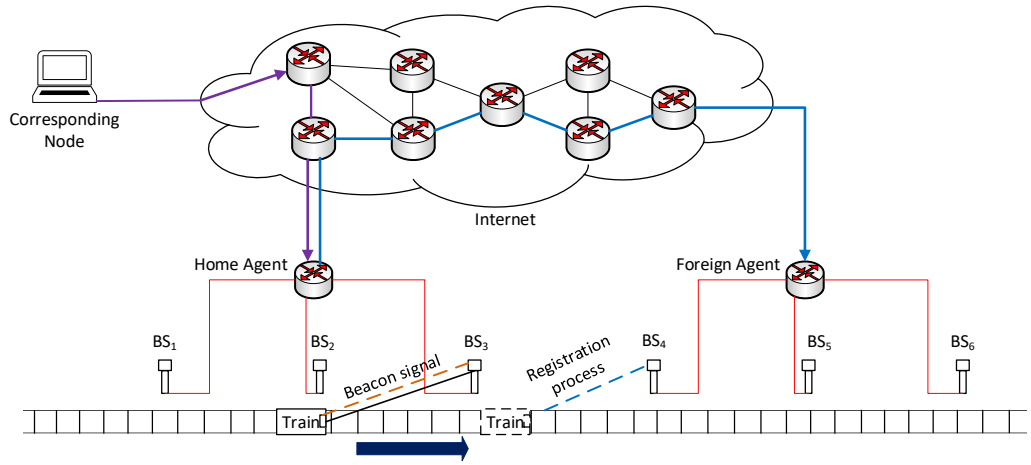

(a)

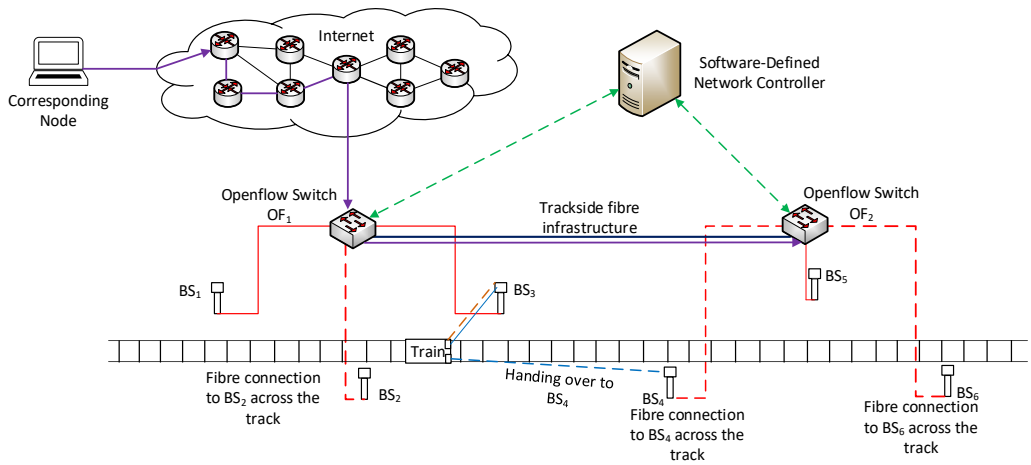

(b)

Fig. 5-6 Network architecture of train-trackside communications with: (a) mobile-IP operation with a foreign agent care-of address, and (b) SDN controller using Openflow.

5.6 Results and Discussions

5.6.1 Experimental Setup

The network topology described in Fig. 5-6 is implemented by developing a dedicated SDN FSO experimental testbed with an SDN-controller and designing a SDN network application using the Ryu SDN framework (see Appendix B). The testbed comprises of three Raspberry Pi4 microcontrollers functioning as an Openflow enabled switches namely OF1, OF2, and OFC as shown in Fig. 5-7. This is accomplished by converting the Raspberry Pi4 into a multilayer virtual switch using Open Vswitch (OvS). Unlike other virtual switches, OvS is open-source and multiplatform [122]. OF1, OFC, and OF2 are connected by a USB 3.0- to- ethernet adapter. OF2 is connected to the laptop through a short range FSO link (i.e., < 1m) using small form factor (SFP) transceiver modules plugged into the media converters, and a Netgear gigabit switch (GS105). Each TP-Link SFP media converter (Model: MC220L) can support up to 1 Gbps in a Full-Duplex mode for the Tx and Rx ports, respectively. A SFP Laser (Model: SFP1G-ZX-55) is inserted in the media converter, which has a transmit power of 5 dBm while the receiver sensitivity is < -24 dBm. OFC is connected to the laptop through the Gigabit switch using a LAN cable. Additional technical descriptions of the components deployed on the testbed are described in Table 5-4.

5.6.2 Ryu-Controller

In this work, we have chosen the Ryu open-source controller. Ryu is a framework for SDN that runs on components and provides well-defined application programming interfaces (APIs), which allow developers to build powerful network management and control applications. Several protocols can be used by Ryu to manage network devices, including Openflow, Netconf, and OF-conFigure. As a result of adopting these types of components, organizations can customize deployments to meet their specific needs; and developers can modify existing components or design their own to ensure that the underlying network can meet their applications' changing requirements. Ryu's code was written entirely in Python and is available under Apache 2.0 license [122]. Aiming to manage switches and routers, system administrators write applications and Openflow or other protocols can be used to interact with the forwarding plane (switches and routers) to control how traffic flows through the network. Several Openflow switches, such as Open vSwitch and products from Centec, Hewlett Packard, IBM, and NEC, have been tested and certified to work with this software [123].

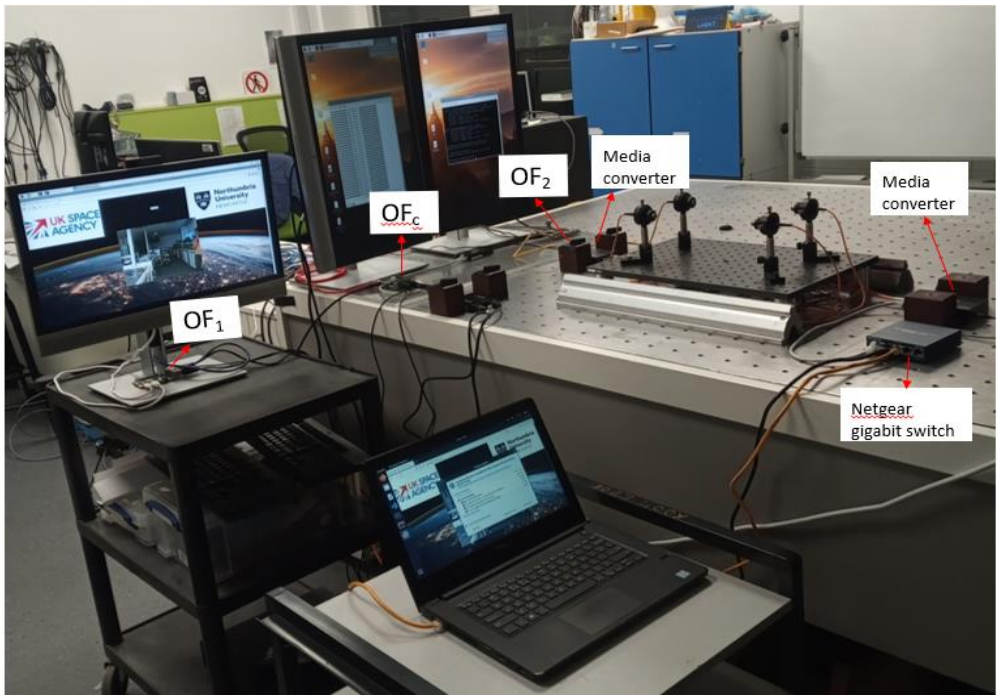

Fig. 5-7 The SDN test-bed

Table 5-4 Component description.

Components	Technical Description	
Raspberry Pi4	Quad core Cortex-A72 (ARM v8) 64-bit SoC @ 1.5GHz	
Media converters	1 × Gigabit small form factor (SFP) port.	
Fiber patch cables	FC-UPC/FC-UPC 62.5/125 µm multimode fiber	
USB 3.0 to ethernet adapter	10/100/1000 Mbps support	
SFP transmitter	Tx Power	5 dBm
	Tx Laser	DFB
	Wavelength	1550 nm
SFP receiver	Rx Sensitivity	< -24 dBm

5.6.3 Handover Mechanism

The handover mechanism described in Section 3 is emulated by (*i*) considering OFC as SDNC and the BS 1, and OF2 as the BS 2; (*ii*) the connection between OFc and OF1 with optical fibre interconnection between two BSs; (*iii*) OF1 as the server; and (*iv*) the laptop representing a user onboard

the train. Initially, OFc and the switch have established a wired LAN connection indicating that the train is connected to the BS 1. A handover is initiated when the FSO link is turned on, thus indicating that the train has established a physical link with the succeeding base station (OF2 in this case). The objective of the SDN testbed is to maintain connectivity of the client (laptop) and the server (OF1) while establishing the handover between OFC and OF2. As shown in Fig. 5-8(a) the communication between the client and the server is established via OFC. Note that, during this period the FSO link is disconnected. When the FSO link is established between OF2, and the laptop, see Fig. 5-8(b), packets from the server are routed through OF2 to the laptop while disabling the connection between the BS 1 and the laptop, thus signalling the completion of the handover between BSs 1 and 2.

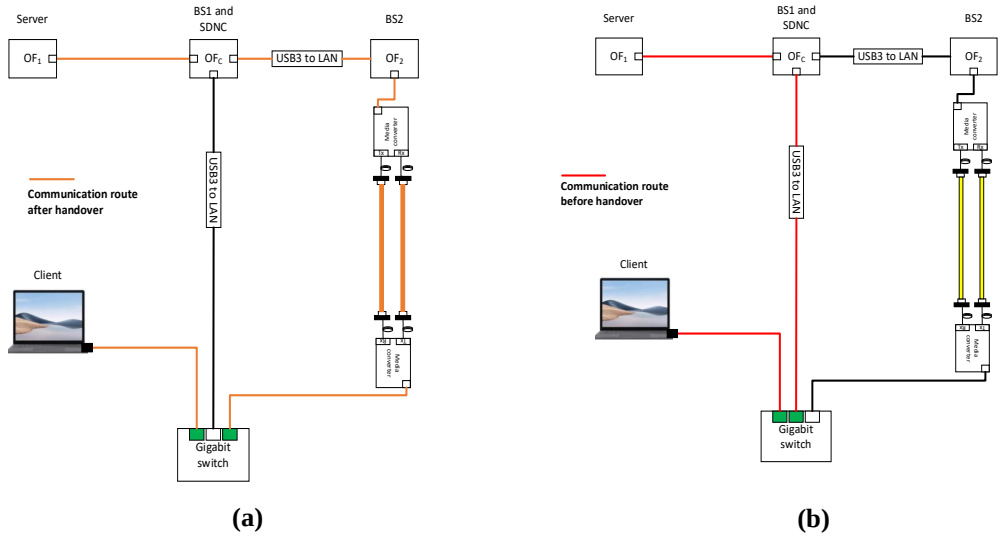

Fig. 5-8 Communication link: (a) before handover, and (b) after handover.

5.6.4 Testing and Implementation

In this section, we evaluate the performance of the handover scheme in terms of the throughput and the packet loss. Note, in this work we have adopted the throughput, which is defined in [124] as:

$$T_h = \frac{B_{rx-t_i+j} - B_{rx-t_i}}{t_{i+j} - t_i}, \tag{5.3}$$

where $B_{rx\text{-}t\_i+j}$ and $B_{rx\text{-}t\_i}$ are the received bytes at times t_{i+j} and t_i, respectively. A network application using Ryu framework is applied in the testbed, which on receiving a router solicitation message from the mobile node triggers a Packet In message. This in turn installs flows with higher priority than the existing flows in the flow table onto OFC and OF1 to initiate the handover of traffic flow from the correspondent node to the laptop through the BSs 1 and 2 to the laptop. Following installation of new flow entries, a port modification message is sent to OFC to disable the communication link to the laptop as described in Fig. 5-9.

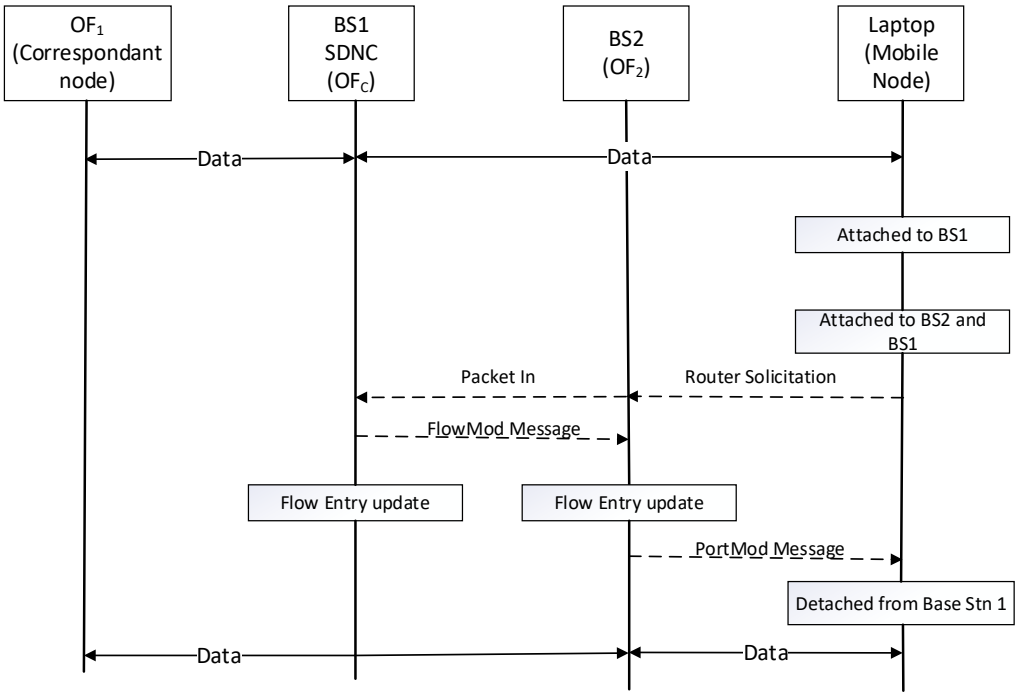

Fig. 5-9 The handover flow chart

Note, (*i*) OF1 sends 586 MB of data at a data rate of 250 Mbps to the laptop using iPerf3; (*ii*) iPerf3 is a tool for active measurement of the maximum achievable bandwidth on IP networks; and (*iii*) the throughput and the packet loss information are measured during the handover procedure. The experiment was performed five times to determine the average packet loss and the throughput. Note that, in [124] the maximum packet loss experienced by the proposed system was 3% while transferring 7.5 Mbytes of the UDP traffic from the client to the server with no mention of the data rate and the system throughput. In [124] and [125], practical implementations of SDN using raspberry Pis were provided. In [125], the handover delay was 72 msec and with the throughput dropping to 400 kbps from 1 Mbps during the handover procedure with no information on the packet loss. Fig. 5-10 depicts the measured data throughput of the SDN testbed with the peak value of 250 Mbps.

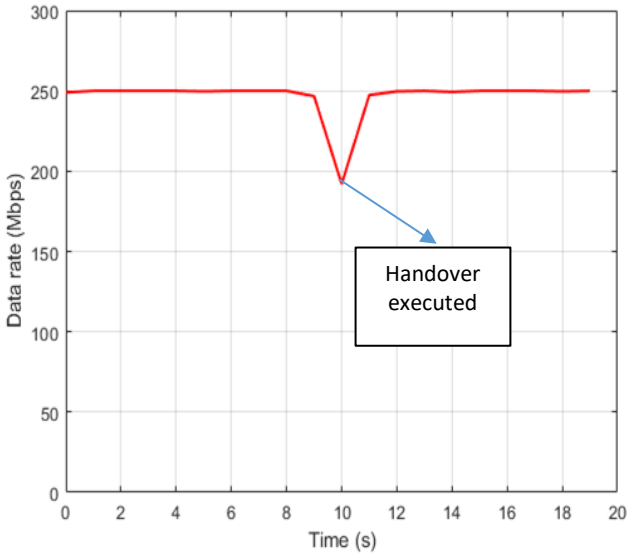

Fig. 5-10 The system yhroughput

However, during the handover process at time t = 10 s the average throughput is dropped to 192 Mbps, which is still reasonably high, whereas the corresponding average packet loss is 25% as shown in Fig. 5-11.

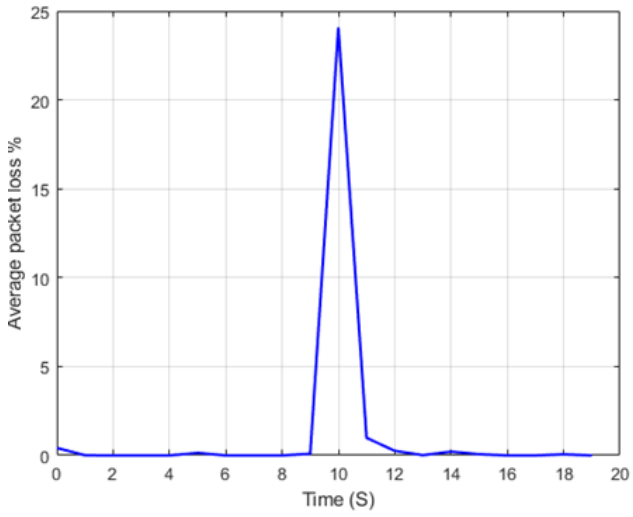

Fig. 5-11 The average packet loss

Fig. 5-12 shows that an average of 30 Mbytes of data is being transferred before and after the handover. Note that, during the handover the average data being transferred is dropped to 24 Mbytes.

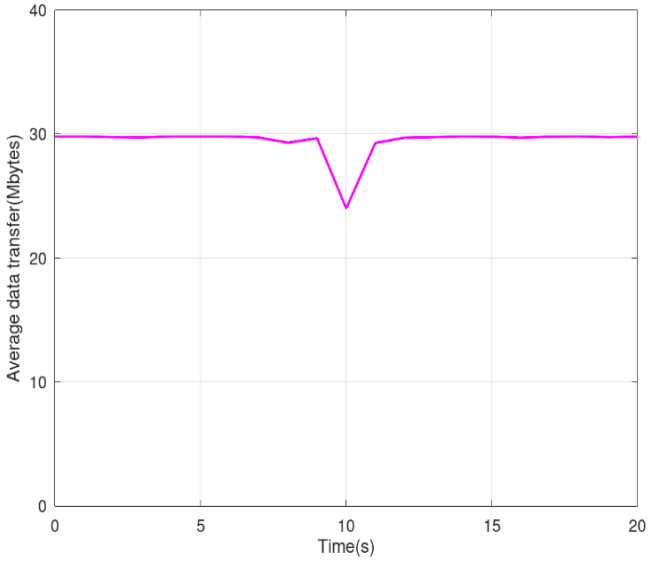

Fig. 5-12 The average data transfer.

5.7 Summary

This chapter provided a primer on SDN and described an implementation of OpenFlow protocol by developing a network application using Ryu controller. The chapter also described a train-trackside communications architecture and the handover mechanism using SDN for the FSO-based transmission system. A dedicated experimental testbed was designed and built using the cost-effective off-the-shelf components to evaluate the performance of the network with handover in terms of the average throughput and the packet loss during the handover operation. The results showed that the proposed scheme offered seamless handover with an average data transfer and throughput of 256 Mbps, respectively dropping down to 196 Mbps during the handover time, thereby, demonstrating that the link is still established between the train and the BS.

Compared with the sectorised base station architecture discussed in chapter 3, the SDN architecture provides greater flexibility in terms of network management, cost of installation is less as the architecture doesn't implement OEOs and EDFAs, more system margin as the system implements collimated beams instead of highly divergent beams. Although, the architecture discussed in this chapter relies on a single SDN controller which presents a single point of failure, redundancy, in such cases are the key to mitigating such issues. Installing more than one controller solves the problem of single point of failure.

Chapter 6: Conclusion and Recommendations for Future Work

6.1 Conclusion

In this thesis we have carried out research to propose a coverage model for ground to train communication discussed in chapter 3, analysed the performance of polar codes under the effect of weak turbulence by determining the optimum code-rate to achieve a BER of 10^{-9} covered in chapter 4 and developed a dedicated SDN based mobility architecture for handover management for ground to train communication described in chapter 5.

To fulfil the objectives of the research laid out in section 1.3, literature review in the fundamentals of FSO communication is presented in chapter 2. In this chapter a brief history and introduction to optical wireless communication is provided specifically highlighting key features of FSO. The Tx, channel and receiver form the fundamental building blocks to any communication system was discussed with respect to FSO. In the Tx section the beam propagation models, laser safety, standards pertaining to laser safety, and atmospheric transmission windows were discussed. In beam propagation models, Gaussian beam propagation was described. The laser safety standards listed the major laser safety standards organisations of which this thesis adopts the IEC standards to classify lasers depending on their AEL. The atmospheric transmission windows section highlighted the wavelength ranges which have fairly low attenuation due to gas absorption present in the atmosphere. The Atmospheric channel deals with absorption and scattering effects due gas molecules and aerosols present in the air which contribute to the attenuation of the FSO link. Further to this Rayleigh and Mie scattering are explained. Section 2.4 introduces to the concept of atmospheric turbulence and describes the pdf and S.I of log-normal turbulence in the weak turbulence regime. The moderate-to-strong turbulence regimes are represented by the gamma-gamma turbulence model. Section 2.5 describes the receiver block of the FSO system. In this section the photodetection technique is illustrated and a brief description of the two most common photodetectors namely, PIN and APD are provided. Photodetection noise sources namely, photon fluctuation, dark noise, NEP, thermal and intensity noise are explained.

In chapter 3, sectorised base station coverage model is proposed which employs multi-beam system to mitigate geometric loss experienced by single wide beam systems. This chapter further proposes two receiver architectures for deployment on the train and have also described the duplex communication between the ground and the train. Power budget analysis was carried out under heavy fog conditions to determine the transmit power required for each beam at the BS. In this system the receivers employed on the train are large, the fluctuations due to turbulence is averaged over the receiver resulting in reduced scintillation and therefore log-normal turbulence regime is considered as a good

fit. Analytical simulations were carried out to determine the ground to train communication performance under weak turbulence. The results from this chapter have resulted in a publication at IET optoelectronics journal. This concept was further extended to multiple base stations and provided a network architecture to minimise handover latency. Two schemes, namely, AOAF, and AF with 2R regenerator with OEO was compared using numerical simulations. The simulations indicated that AOAF scheme, due to accumulation of noise from the previous base stations and performed poorly against the AF with 2R regenerator with OEO due to the fact that the latter option utilises FEC features for error correction as error correction can be done only on the electrical domain. The key takeaway from the discussion is that cost of implementation needs to be factored in while considering installation of the G2T architecture discussed in this section. The cost of implementation is directly proportional to the number of OEO conversions required which makes the OEO solution less attractive as compared to its RF counterparts. This may substantially increase the initial system installation even if deployed on a small scale. Also, only a small fraction of the network can be successfully reproduced in the lab which casts uncertainty on some of the "on-field" parameters which may not be accurately reproduced in the lab. Extra system margin needs to be allocated to mitigate these uncertainties.

In Chapter 4 turbulence mitigation using polar codes is proposed. In this chapter the concept of channel polarisation and using this concept explains polar encoding and decoding for successive cancellation decoder and successive cancellation list decoder. The log-likelihood ratio for on-off keying was derived. From a practical perspective the calculation of exact using stochastic processes was deemed to be complex in terms of computation and hardware. as was therefore approximated. For a BER of 10^{-9} with 95% confidence limit, and OOK as the modulation scheme Monte-Carlo simulations were performed under weak turbulence regime to determine the optimum code rate for various scintillation indices for the SC decoder. The results of this chapter were published in IET optoelectronics journal.

In chapter 5 provides a brief description of the concept of SDN, discusses about the OpenFlow protocol and OVS. This discussion is followed by a description of the FSO-SDN testbed design leveraging off-the-shelf components and development of a network monitor application using Ryu Controller. Furthermore, the concept of SDN is employed for handover management in G2T communications. A network architecture is developed and described using SDN. This concept is then emulated using the SDN testbed. The results showed that the proposed scheme offered seamless handover with an average data transfer and throughput of 256 Mbps, respectively dropping down to 196 Mbps during the handover time, thereby, demonstrating that the link is still established between the train and the BS. The results of this chapter have been submitted to IET Networks journal.

6.2 Recommendations for Future Work

This thesis has contributed to coverage and optimisation of base station deployment, turbulence mitigation using FEC and design and deployment of network protocol for ground to train communication and has uncovered new avenues to improve upon the current research. The following list provides ideas to take this research forward:

- The coverage model proposed in Chapter 3 takes into consideration the weak turbulence regime and uses log-normal turbulence. Analytical turbulence modelling for ground to train communications to predict the accuracy against the log-normal could prove to be significant in designing practical systems. The analytical model can be improved by considering wind-tunnel/atmospheric chamber experimental data.
- The pointing accuracy due to train vibrations also needs to be considered while designing a practical system. The receiver architectures proposed in Chapter 3 could be analytically evaluated using Zeemax software in terms of received power coupling losses. Using the data from Zeemax, a suitable optical coupler could be designed.
- The optimum code rate for other forward error correcting codes such as Reed-Solomon, LDPC and turbo codes could be determined. Other turbulence mitigation techniques such as relay assisted FSO and aperture averaging in tandem with FEC could be implemented to determine the performance of the FSO link under turbulence.
- Software-defined radio could be used to create waveforms of different scintillation indices as the atmospheric chamber in the Optical communications research group lab is only capable of generating weak turbulence.
- The SDN testbed could be improved be including three BS instead of two as described in Chapter 5. Latency measurements could provide insight into the real-time performance of SDN network protocol.
- The SDN protocol designed in Chapter 5 could be extended to indoor environments to provide seamless connections while the user is moving. An experimental testbed could be set-up using indoor lighting could be an interesting idea for creating a product.

References

[1] Cisco annual internet Report - Cisco Annual Internet Report (2018–2023) White Paper (2022) Cisco. Cisco. Available at: https://www.cisco.com/c/en/us/solutions/collateral/executive-perspectives/annual-internet-report/white-paper-c11-741490.html#Trends (Accessed: October 31, 2022).

[2] "Welcome to CrossCountry", CrossCountry Trains, 2022. [Online]. Available: https://www.crosscountrytrains.co.uk/on-board-with-crosscountry/wifi-on-board. [Accessed: 26- Jan- 2022].

[3] "Advice to Government on improving rail passenger access to data services", Ofcom, 2022. [Online]. Available: https://www.ofcom.org.uk/spectrum/information/rail-passenger-data-access. [Accessed: 26- Jan- 2022].

[4] K. Wu, W. Ni, T. Su, R. P. Liu and Y. J. Guo, "Recent Breakthroughs on Angle-of-Arrival Estimation for Millimeter-Wave High-Speed Railway Communication," in IEEE Communications Magazine, vol. 57, no. 9, pp. 57-63, September 2019, doi: 10.1109/MCOM.001.1800966.

[5] Z. Ghassemlooy, W. Popoola and S. Rajbhandari, Optical Wireless Communications. Milton: CRC Press LLC, 2019

[6] F R Gfeller and U Bapst, Wireless in-house data communication via diffuse infrared radiation, Proceedings of the IEEE, 67, 1474–1486, 1979

[7] J R Barry, Wireless Infrared Communications, Boston: Kluwer Academic Publishers, 1994

[8] L. Mohon, “Laser Communications Relay Demonstration (LCRD),” NASA, 14-Jul-2015. [Online]. Available: https://www.nasa.gov/mission_pages/tdm/lcrd/index.html. [Accessed: 31-Oct-2022]

[9] M. Z. Chowdhury, M. T. Hossan, A. Islam and Y. M. Jang, "A Comparative Survey of Optical Wireless Technologies: Architectures and Applications," in IEEE Access, vol. 6, pp. 9819-9840, 2018, doi: 10.1109/ACCESS.2018.2792419

[10] M. A. Khalighi and M. Uysal, “Survey on free space optical communication: A communication theory perspective,” IEEE Communications Surveys & Tutorials, vol. 16, no. 4, pp. 2231–2258, 2014.

[11] M. R. Feldman, S. C. Esener, C. C. Guest, and S. H. Lee, “Comparison between electrical and optical interconnect based on power and speed consideration,” Applied. Optics, vol. 27, no. 9, pp. 1742–1751, Sept. 1998.

[12] D. A. B. Miller, “Rationale and challenges for optical interconnects to electronic chips,” Proceedings of the IEEE, vol. 88, no. 6, pp. 728–749, June 2000.

[13] C. Kachris and I. Tomkos, “A survey on optical interconnects for data centers,” IEEE Communications Surveys & Tutorials, vol. 14, no. 4, pp. 1021–1036, Oct. 2012.

[14] M. A. Taubenblatt, “Optical interconnects for high-performance computing,” IEEE/OSA Journal of Lightwave Technology, vol. 30, no. 4, pp. 448–457, Feb. 2012.

[15] F. Hanson and S. Radic, “High bandwidth underwater optical communication,” Applied Optics, vol. 47, no. 2, pp. 277–283, Jan. 2008.

[16] C. Gabriel, M. A. Khalighi, S. Bourennane, P. L´eon, and V. Rigaud, “Monte-carlo-based channel characterization for underwater optical communication systems,” IEEE/OSA Journal of Optical Communications and Networking, vol. 5, no. 1, pp. 1–12, Jan. 2013.

[17] Scott Bloom, Eric Korevaar, John Schuster, and Heinz Willebrand, "Understanding the performance of free-space optics [Invited]," J. Opt. Netw.2, 178-200, 2003.

[18] A. Prokeš, "Modeling of atmospheric turbulence effect on terrestrial FSO link", Radioengineering, vol. 18, no. 1, pp. 42-47, Jan. 2009

[19] R. M. Gagliardi and S. Karp, Optical Communications, 2nd ed. New York: John Wiley, 1995.

[20] “Recommendation ITU-R P.1817-1 - propagation data required for the ...” [Online]. Available: https://www.itu.int/dms_pubrec/itu-r/rec/p/R-REC-P.1817-1-201202-I!!PDF-E.pdf. [Accessed: 31-Oct-2022].

[21] W K Pratt, Laser Communication Systems, 1st ed New York: John Wiley & Sons, Inc , 1969

[22] X. Zhu and J. M. Kahn, "Free-space optical communication through atmospheric turbulence channels," IEEE Transactions on Communications, vol. 50, pp. 1293-1300, Aug. 2002

[23] L. C. Andrews, R. L. Phillips, and C. Y. Hopen, Laser beam scintillation with applications. Bellingham: SPIE, 2001

[24] AFGL, "AFGL Atmospheric Constituent Profiles (0–120 km), ," AFGL-TR-86-0110, Air Force Geophysics Laboratory, Hanscom Air Force Base, Massachusetts, 1986

[25] G. R. Osche, Optical Detection Theory for Laser Applications. New Jersey: Wiley, 2002.

[26] S. Karp, R. M. Gagliardi, S. E. Moran, and L. B. Stotts, Optical Channels: fibers, clouds, water and the atmosphere. New York: Plenum Press, 1988.

[27] V. I. Tatarski, Wave propagation in a turbulent medium. (Translated by R.A. Silverman) New York: McGraw-Hill 1961.

[28] A. Ishimaru, "The beam wave case and remote sensing," in Topics in Applied Physics: Laser Beam Propagation in the Atmosphere. vol. 25 p.134 New York: Springer-Verlag, 1978.

[29] H. Hodara, "Laser wave propagation through the atmosphere," Proceedings of the IEEE, vol. 54, pp. 368-375, March 1966.

[30] S. F. Clifford, "The classical theory of wave propagation in a turbulent medium," in Laser Beam Propagation in the Atmosphere, J. W. Strobehn, Ed.: Springer-Verlag, 1978.

[31] J W Goodman, Statistical Optics New York: John Wiley, 1985

[32] M Uysal, S M Navidpour and J T Li, Error rate performance of coded free-space optical links over strong turbulence channels, IEEE Communication Letters, 8, 635–637, 2004

[33] W. O. Popoola, Z. Ghassemlooy, and E. Leitgeb, "Free-space optical communication using subcarrier modulation in gamma-gamma atmospheric turbulence," 9th International Conference on Transparent Optical Networks (ICTON '07) vol. 3, pp. 156-160, July 2007.

[34] G Keiser, Optical Fiber Communications, 3rd ed New York: McGraw-Hill, 2000

[35] K Shiba, T Nakata, T Takeuchi, T Sasaki and K Makita, 10 Gbit/s asymmetric waveguide.

[36] S Betti, G De Marchis and E Iannone, Coherent Optical Communication Systems, 1st ed Toronto, Canada: John Wiley & Sons Inc , 1995

[37] "Amplified photodetector, biased, AC coupled, 1000-1650nm, InGaAs, 10 GHz," 818-BB-35A Amplified Photodetector. [Online]. Available: https://www.newport.com/p/818-BB-35A. [Accessed: 31-Oct-2022]

[38] D. R. Paschotta, "Noise-equivalent power," to, 03-Mar-2021. [Online]. Available: https://www.rp-photonics.com/noise_equivalent_power.html. [Accessed: 31-Oct-2022]

[39] United Nations Framework Convention on Climate Change (UNFCCC): 'Kyoto Protocol to the United Nations framework convention on climate change'. 1998, Available at http://unfccc.int/essential_background/kyoto_protocol/items/1678.php, accessed June 2019

[40] Borken-Kleefeld, J., Berntsen, T., Fuglestvedt, J.: 'Specific climate impact of passenger and freight transport', Environ. Sci. Technol., 2010, 44, pp. 5700–5706

[41] Available at https://www.saveatrain.com/blog/why-choosing-to-travel-bytrain-is-environmentally-friendly/, accessed June 2019

[42] Terada, M., Teraoka, F.: 'Providing a high-speed train with a broadband and fault tolerant IPv4/6 NEMO environment'. 2012 IEEE Globecom Workshops, Anaheim, CA, 2012, pp. 1052–1056

[43] Verstrepen, L.: 'Making a well-founded choice of the wireless technology for train-to-wayside data services'. 2010 9th Conf. of Telecommunication, Media and Internet, Ghent, 2010, pp. 1–7, doi: 10.1109/CTTE.2010.5557701

[44] Müller, M.K., Taranetz, M., Rupp, M.: 'Providing current and future cellular services to high speed trains', IEEE Commun. Mag., 2015, 53, (10), pp. 96– 101

[45] Zhou, Y., Pan, Z., Hu, J., et al.: 'Broadband wireless communications on high-speed trains'. 2011 20th Annual Wireless and Optical Communications Conf. (WOCC), Newark, NJ, 2011, pp. 1–6

[46] ACCORDE: ‘ACORDE – broadband railway internet access on high-speed trains via satellite links. Press release. Accorde’ (Santander, Spain, 2008). Available at http://www.railway-technology.com/contractors/signal/acorde/

[47] Paudel, R., Tang, X., Ghassemlooy, Z.: ‘Laboratory demonstration of FSO ground-to-train communications with multiple base stations’. 2016 10th Int. Symp. on Communication Systems, Networks and Digital Signal Processing (CSNDSP), Prague, 2016, pp. 1–6

[48] Welcome to CrossCountry: 2019. Available at https://www.crosscountrytrains.co.uk/on-board-with-crosscountry/wifi-on-board

[49] Chung, H.: ‘From architecture to field trial: a millimeter wave based MHN system for HST communications toward 5G’. 2017 European Conf. on Networks and Communications (EuCNC), Oulu, 2017, pp. 1–5, doi: 10.1109/ EuCNC.2017.7980752

[50] Kanno, A., Dat, P.T., Umezawa, T., et al.: ‘Field trial of 1.5-gbps 97-GHz train communication system based on linear cell radio over fiber network for 240-km/h high-speed train’. 2019 Optical Fiber Communications Conf. and Exhibition (OFC), San Diego, CA, USA, 2019, pp. 1–3

[51] Dat, P.T., Kanno, A., Inagaki, K., et al.: ‘High-speed and uninterrupted communication for high-speed trains by ultrafast WDM fiber-wireless backhaul system’, J. Lightw. Technol., 2019, 37, (1), pp. 205–217

[52] Abadi, M.M., Ghassemlooy, Z., Mohan, N., et al.: ‘Implementation and evaluation of a gigabit Ethernet FSO link for ‘the last metre and last mile access network’’. 2019 IEEE Int. Conf. on Communications Workshops (ICC Workshops), Shanghai, China, 2019, pp. 1–6

[53] Ghassemlooy, Z., Popoola, W., Rajbhandari, S.: ‘Optical wireless communications: system and channel modelling with MATLAB’ (CRC Press, Boca Raton, FL, USA, 2013)

[54] Urabe, H., Haruyama, S., Shogenji, T., et al.: ‘High data rate ground-to-train frees space optical communication system’, Opt. Eng., Spec. Sect. Free-Space Laser Commun., 2012, 51, (3), pp. 031 204–031 204-9

[55] Mori, K., Terada, M., Nakamura, K., et al.: ‘Fast handover mechanism for high data rate ground-to-train free-space optical communication system’. 2014 IEEE Globecom Workshops (GC Wkshps), Austin, TX, 2014, pp. 499–504

[56] Fan, Q., Taheri, M., Ansari, N., et al.: ‘Reducing the impact of handovers in ground-to-train free space optical communications’, IEEE Trans. Veh.Technol., 2018, 67, (2), pp. 1292–1301

[57] Fan, Q., Ansari, N., Feng, J., et al.: ‘Reducing the number of FSO base stations with dual transceivers for next-generation ground-to-train communications’, IEEE Trans. Veh. Technol., 2018, 67, (11), pp. 11143–11153

[58] Fathi-Kazerooni, S., Kaymak, Y., Rojas-Cessa, R., et al.: 'Optimal positioning of ground base stations in free-space optical communications for high-speed trains', IEEE Trans. Intell. Transp. Syst., June 2018, 19, (6), pp. 1940–1949, doi: 10.1109/TITS.2017.2741999

[59] Leitgeb, E., Muhammad, S.S., Chlestil, C., et al.: 'Reliability of FSO links in next generation optical networks'. Proc. of 2005 7th Int. Conf. Transparent Optical Networks, 2005, Barcelona, Catalonia, 2005, Vol. 1, pp. 394–401

[60] Rajbhandari, S., Ghassemlooy, Z., Haigh, P.A., et al.: 'Experimental error performance of modulation schemes under a controlled laboratory turbulence FSO channel', J. Lightw. Technol., 2015, 33, (1), pp. 244–250

[61] Khalighi, M.A., Aitamer, N., Schwartz, N., et al.: 'Turbulence mitigation by aperture averaging in wireless optical systems'. 2009 10th Int. Conf. on Telecommunications, Zagreb, 2009, pp. 59–66

[62] Navidpour, S.M., Uysal, M., Kavehrad, M.: 'BER performance of free-space optical transmission with spatial diversity', IEEE Trans. Wirel. Commun.,2007, 6, (8), pp. 2813–2819

[63] Kruse, P.W., McGlauchlin, L.D., McQuistan, R.B.: 'Elements of infrared technology: generation, transmission, and detection' (Wiley, New York, NY, USA, 1962)

[64] Noordegraaf, D., Skovgaard, P., Nielsen, M., et al.: 'Efficient multi-mode to single-mode coupling in a photonic lantern', Opt. Express, 2009, 17, (3), p.1988, doi:10.1364/oe.17.001988

[65] Uysal, M., et al.: Optical wireless communications, pp. 107–122. Springer, Switzerland (2016)

[66] Cheng, M., Guo, L., Zhang, Y.: Scintillation and aperture averaging for Gaussian beams through non-Kolmogorov maritime atmospheric turbulence channels. Opt. Express. 23(25), 32606–32621 (2015). https:// doi.org/10.1364/OE.23.032606

[67] Perlot, N., Fritzsche, D.: Aperture averaging: theory and measurements. In: Free-Space Laser Communication Technologies XVI, vol. 5338, pp. 233–242. International Society for Optics and Photonics (2004)

[68] Shen, H., Yu, L., Fan, C.: Temporal spectrum of atmospheric scintillation and the effects of aperture averaging and time averaging. Opt Commun. 330, 160–164 (2014)

[69] Tsiftsis, T.A., et al.: FSO Links with spatial diversity over strong atmospheric turbulence channels. In: 2008 IEEE International Conference on Communications, 19-23 May, pp. 5379–5384 (2008). https://doi.org/10.1109/ICC.2008.1008

[70] Yang, G., et al.: Contrasting space-time schemes for MIMO FSO systems with non-coherent modulation. In 2012 International Workshop on Optical Wireless Communications (IWOW), pp. 1–3. IEEE (2012)

[71] Nor, N.A.M., et al.: Experimental investigation of all-optical relay-assisted 10 Gb/s FSO link over the atmospheric turbulence channel. J.Lightwave Technol. 35(1), 45–53 (2016)

[72] Nor, N.A.M., et al.: Experimental analysis of a triple-hop relay-assisted FSO system with turbulence. Opt. Switch Netw. 33, 194–198 (2019)

[73] Zhao, Z., Lyke, S.D., Roggemann, M.C.: Adaptive optical communication through turbulent atmospheric channels. In: 2008 IEEE International Conference on Communications, pp. 5432–5436. IEEE (2008)

[74] Song, X., Cheng, J.: Subcarrier intensity modulated MIMO optical communications in atmospheric turbulence. J. Opt. Commun. Netw.5(9), 1001–1009 (2013)

[75] Pernice, R., et al.: Error mitigation using RaptorQ codes in an experimental indoor free space optical link under the influence of turbulence. IET Commun. 9(14), 1800–1806 (2015)

[76] Safi, H., et al.: Adaptive channel coding and power control for practical FSO communication systems under channel estimation error. IEEE Trans. Veh. Technol. 68(8), 7566–7577 (2019)

[77] Garcia-Zambrana, A.: Error rate performance for STBC in free-space optical communications through strong atmospheric turbulence. IEEE Commun. Lett. 11(5), 390–392 (2007)

[78] García-Zambrana, A., Castillo-Vázquez, C., Castillo-Vázquez, B.: Rate-adaptive FSO links over atmospheric turbulence channels by jointly using repetition coding and silence periods. Opt. Express. 18(24), 25422–25440 (2010)

[79] Zhou, H., Mao, S., Agrawal, P.: Optical power allocation for adaptive transmissions in wavelength-division multiplexing free space optical networks. Digit. Commun. Netw. 1(3), 171–180 (2015)

[80] Djordjevic, I.B.: Adaptive modulation and coding for free-space optical channels. J. Opt. Commun. Netw. 2(5), 221–229 (2010)

[81] Liu, L., Safari, M., Hranilovic, S.: Rate-adaptive FSO communication via rate-compatible punctured LDPC codes. In: 2013 IEEE International Conference on Communications (ICC), pp. 3948–3952. IEEE (2013)

[82] Hassan, M.Z., et al.: Delay-QoS-aware adaptive modulation and power allocation for dual-channel coherent OWC. J. Opt. Commun. Netw.10(3), 138–151 (2018)

[83] Huang, Z., et al.: Computer-vision–based intelligent adaptive transmission for optical wireless communication. Opt. Express. 27(6), 7979–7987 (2019)

[84] Blasco-Serrano, R., et al.: Polar codes for compress-and-forward in binary relay channels. In: 2010 Conference Record of the Forty Fourth Asilomar Conference on Signals, Systems and Computers, pp. 1743–1747. IEEE (2010)

[85] Jouguet, P., Kunz-Jacques, S.: High performance error correction for quantum key distribution using polar codes. (2012). arXiv preprint arXiv:1204.5882

[86] Fang, J., et al.: Performance investigation of the polar coded FSO communication system over turbulence channel. Appl. Opt. 57(25), 7378–7384 (2018)

[87] Fang, J., et al.: Neural network decoder of polar codes with tanh-based modified LLR over FSO turbulence channel. Opt. Express. 28(2), 1679–1689 (2020)

[88] Fang, J., et al.: Polar-coded MIMO FSO communication system over gamma-gamma turbulence channel with spatially correlated fading. J.Opt. Commun. Netw. 10(11), 915–923 (2018)

[89] Tal, I., Vardy, A.: How to construct polar codes. IEEE Trans. Inf. Theor.59(10), 6562–6582 (2013)

[90] Lin, J., Yan, Z.: An efficient list decoder architecture for polar codes. IEEE Trans .Very Large Scale Integr. Syst. 23(11), 2508–2518 (2015)

[91] EventHelix, "Polar codes," Medium, 29-Apr-2019. [Online]. Available: https://medium.com/5g-nr/polar-codes-703336e9f26b. [Accessed: 31-Oct-2022]

[92] Arikan, E.: Channel polarization: a method for constructing capacity-achieving codes for symmetric binary-input memoryless channels. IEEE Trans. Inf. Theor. 55(7), 3051–3073 (2009)

[93] Bioglio, V., Condo, C., Land, I.: Design of polar codes in 5G new radio. IEEE Commun. Surv. Tutor. 23(1), 29–40 (2020)

[94] Sarkis, G., et al.: Fast list decoders for polar codes. IEEE J. Sel. Area Commun. 34(2), 318–328 (2015)

[95] Tal, I., Vardy, A.: List decoding of polar codes. IEEE Trans. Inf. Theor.61(5), 2213–2226 (2015)

[96] Condo, C., et al.: Design and implementation of a polar codes blind detection scheme. IEEE Trans. Circuits Syst. II. 66(6), 943–947 (2019). https://doi.org/10.1109/TCSII.2018.2872653

[97] Le, D.-D., et al.: Log-likelihood ratio calculation using 3-bit soft-decision for error correction in visible light communication systems. IEICE Trans. Fund. Electron. Commun. Comput. Sci. 101(12), 2210–2212 (2018)

[98] Olivatto, V.B., Lopes, R.R., de Lima, E.R.: Simplified method for log-likelihood ratio approximation in high-order modulations based on the Voronoi decomposition. IEEE Trans. Broadcast. 63(3), 583–589 (2017)

[99] Olivatto, V.B., Lopes, R.R., de Lima, E.R.: Simplified LLR calculation for DVB-S2 LDPC decoder. In: 2015 IEEE International Conference on Communication, Networks and Satellite (COMNESTAT), pp. 26–31. IEEE (2015)

[100] Park, J.W., et al.: Simplified soft-decision demapping algorithm for DVB-S2. In: 2009 International SoC Design Conference (ISOCC), pp. 444–447. IEEE (2009)

[101] Yazdani, R., Ardakani, M.: Efficient LLR calculation for non-binary modulations over fading channels. IEEE Trans. Commun. 59(5), 1236–1241 (2011)

[102] Mohan, N., et al.: Sectorised base stations for FSO ground-to-train communications. IET Optoelectron. 14(5), 312–318 (2020)

[103] Kaur, P., Jain, V.K., Kar, S.: Performance of free space optical links in presence of turbulence, pointing errors and adverse weather conditions. Opt. Quant. Electron. 48(1), 65 (2016)

[104] How Do I Measure the Bit Error Rate (BER) to a Given Confidence Level on the J-BERT M8020A and the M8040A High-Performance BERT? – Technical Support Knowledge Center Open, Edadocs.software.keysight.com, 2021. [Online]. https://edadocs.software.keysight.com/kkbopen/how-do-i-measure-the-bit-error-rate-ber-to-a-given-confidence-level-on-the-j-bert-m8020a-and-the-m8040a-high-performancebert-588276182.html. [Accessed: 26 April 2021]

[105] "Younger people demand improved internet connectivity on return to railways | RailStaff", Railstaff.co.uk, 2022. [Online]. Available: https://www.railstaff.co.uk/2021/10/05/younger-people-demand-improved-internet-connectivity-on-return-to-railways/. [Accessed: 26- Jan- 2022].

[106] K. Kong, W. Lee, Y. Han, M. Shin and H. You, "Mobility management for all-IP mobile networks: mobile IPv6 vs. proxy mobile IPv6," in IEEE Wireless Communications, vol. 15, no. 2, pp. 36-45, April 2008, doi: 10.1109/MWC.2008.4492976.

[107] J. Lee, Z. Yan and I. You, "Enhancing QoS of Mobile Devices by a New Handover Process in PMIPv6 Networks", Wireless Personal Communications, vol. 61, no. 4, pp. 591-602, 2011. Available: 10.1007/s11277-011-0422-4.

[108] D. Kreutz, F. M. V. Ramos, P. E. Veríssimo, C. E. Rothenberg, S. Azodolmolky and S. Uhlig, "Software-Defined Networking: A Comprehensive Survey," in Proceedings of the IEEE, vol. 103, no. 1, pp. 14-76, Jan. 2015, doi: 10.1109/JPROC.2014.2371999.

[109] A. Sen, K. M. Sivalingam and B. K. J. Narayanan, "Persistent WiFi connectivity during Train journey: An SDN based approach," 2019 IFIP/IEEE Symposium on Integrated Network and Service Management (IM), 2019, pp. 634-638.

[110] D. Franco, M. Aguado, and N. Toledo, “An Adaptable Train-to-Ground Communication Architecture Based on the 5G Technological Enabler SDN,” Electronics, vol. 8, no. 6, p. 660, Jun. 2019 [Online]. Available: http://dx.doi.org/10.3390/electronics8060660.

[111] Y. Kyung and T.-K. Kim, “QoS-Aware Flexible Handover Management in Software-Defined Mobile Networks,” Applied Sciences, vol. 10, no. 12, p. 4264, Jun. 2020 [Online]. Available: http://dx.doi.org/10.3390/app10124264

[112] "Publication List", Nexans.com, 2022. [Online]. Available: https://www.nexans.com/newsroom/publications.html?category=eb4ebaf0-476c-4294-815f-f28d9ec16ca1. [Accessed: 26- Jan- 2022].

[113] A. Speed, "Average Train Speed | Onaverage.co.uk", Onaverage.co.uk, 2022. [Online]. Available: https://www.onaverage.co.uk/speed-averages/58-average-train-speed#:~:text=The%20average%20speed%20at%20which,%2Fh)%20for%20Maglev%20trains. [Accessed: 01- Feb- 2022].

[114] "Evo rail", Evo-rail.com, 2022. [Online]. Available: https://www.evo-rail.com/. [Accessed: 26- Jan- 2022].

[115] W. Popoola, "Subcarrier Intensity Modulated Free-Space Optical Communication Systems", Nrl.northumbria.ac.uk, 2009. [Online]. Available: https://nrl.northumbria.ac.uk/id/eprint/1939/1/popoola.wasiu_phd.pdf. [Accessed: 04- Feb- 2022].

[116] B. Suh, H. Lee, S. Kim and S. Jeon, "A D-Band Multiplier-Based OOK Transceiver With Supplementary Transistor Modeling in 65-nm Bulk CMOS Technology," in IEEE Access,

[117] "Thorlabs - RXM10BF Multimode Ultrafast Receiver, 750 - 1650 nm, 40 kHz - 10 GHz, FC/PC", Thorlabs.com, 2022. [Online]. Available: https://www.thorlabs.com/thorproduct.cfm?partnumber=RXM10BF. [Accessed: 05- Feb- 2022].

[118] "RFC 3344 - IP Mobility Support for IPv4", Datatracker.ietf.org, 2022. [Online]. Available: https://datatracker.ietf.org/doc/html/rfc3344. [Accessed: 11- Apr- 2022].

[119] "Chapter 1 Overview of Mobile IP (Mobile IP Administration Guide)", Docs.oracle.com, 2022. [Online]. Available: https://docs.oracle.com/cd/E19455-01/806-6542/6jffqf5sb/index.html. [Accessed: 11- Apr- 2022].

[120] "The TCP/IP Guide - Mobile IP Addressing: Home and "Care-Of" Addresses", Tcpipguide.com, 2022. [Online]. Available: http://www.tcpipguide.com/free/t_MobileIPAddressingHomeandCareOfAddresses.htm. [Accessed: 11- Apr- 2022].

[121] M. T. Dabiri, S. M. S. Sadough and M. A. Khalighi, "Blind Signal Detection Under Synchronization Errors for FSO Links With High Mobility," in IEEE Transactions on Communications, vol. 67, no. 10, pp. 7006-7015, Oct. 2019

[122] "Getting Started — Ryu 4.34 documentation", Ryu.readthedocs.io, 2022. [Online]. Available: https://ryu.readthedocs.io/en/latest/getting_started.html#what-s-ryu. [Accessed: 12- Apr- 2022

[123] S. Studios, “What Is a Ryu Controller?,” Sdx Central, 23 June 2016. [Online]. Available: https://www.sdxcentral.com/networking/sdn/definitions/what-is-ryu-controller/. [Accessed November 2021].

[124] J. Lam, S. Lee, H. Lee and Y. Eko Oktian, "Design, implementation, and performance evaluation of identity-based cryptography in ONOS", International Journal of Network Management, vol. 28, no. 1, p. e1990, 2017. Available: 10.1002/nem.1990.

[125] J. W. Lim, T. Mahboob and M. Y. Chung, "An Efficient Multihoming Scheme to Support Seamless Handover in SDN-based Network Mobility," 2021 IEEE International IOT, Electronics and Mechatronics Conference (IEMTRONICS), 2021, pp. 1-6, doi: 10.1109/IEMTRONICS52119.2021.9422553.

[126] R. M. Manning, "Beam wave considerations for optical link budget calculations", 2016.

[127] RECOMMENDATION ITU-R S.1590 "Technical and operational characteristics of satellites operating in the range 20-375 THz" https://www.itu.int/dms_pubrec/itu-r/rec/s/R-REC-S.1590-0-200209-I!!PDF-E.pdf (accessed May 18, 2023

[128] RECOMMENDATION ITU-R P.1814 "Prediction methods required for the design of terrestrial free-space optical links, https://www.itu.int/dms_pubrec/itu-r/rec/p/R-REC-P.1814-0-200708-I!!PDF-E.pdf (accessed May 19, 2023).

[129] S. Kazemlou, "All-Optical Multihop Free-Space Optical Communication Systems", PhD, McMaster University, 2010.

[130] T. Y. Elganimi, "Studying the BER performance, power- and bandwidth- efficiency for FSO communication systems under various modulation schemes," 2013 IEEE Jordan Conference on Applied Electrical Engineering and Computing Technologies (AEECT), Amman, 2013, pp. 1-6.

[131] Frankel M, Livas J, inventors; Ciena Corp, assignee. Simplified signal regenerator structure. United States patent application US 11/090,047. 2006 Jun 15.

[132] Ieee802.org, 2020. [Online]. Available: http://www.ieee802.org/3/ca/public/meeting_archive/2017/03/vanveen_3ca_1a_0317.pdf. [Accessed: 26- Feb- 2020].

[133] Ciaramella E. Wavelength conversion and all-optical regeneration: achievements and open issues. Journal of Lightwave Technology. 2011 Nov 24;30(4):572-82.

[134] Software-defined networking using openflow: Protocols, applications and ..., https://hepia.infolibre.ch/Virtualisation-Reseaux/2014_SDN_with_OpenFlow_Protocols_Applications_and_Architectural_Design_Choices.pdf (accessed Jun. 30, 2023).

Appendix A: Polar Encoder and Decoder

A.1 Polar Encoder

```
#include <iostream>
#include <string>
#include <vector>
#include <cmath>
#include <algorithm>
#include <time.h>
using namespace std;

vector<int> rand_msg_bits(int K){
    vector<int> result(K);
    srand((unsigned)time(NULL));
    for (int i = 0; i<K; i++){
        if ((float)rand()/RAND_MAX > 0.5){
            result[i] =1;
        }
        else{
            result[i] = 0;
        }
    }
    return result;
}

vector <int> Data_bits(vector<int>& reliability_seq, int N, int K){
    vector<int> result, data_bits;
    for (vector<int>::const_iterator iter = reliability_seq.begin(); iter
!= reliability_seq.end(); iter++){
        if ((*iter)<=N-1){
            result.push_back(*iter);
        }
    }
    for (vector<int>::size_type i = N-K; i!= result.size(); i++){
        data_bits.push_back(result[i]);
    }
    return data_bits;
}

vector<float> Mod_2_addition(vector<float>& data_1, vector<float>& data_2)
{
    vector<float> result;
    for (vector<float>::size_type i = 0; i !=data_1.size(); i++){
        result.push_back((data_2[i]+data_1[i])-
2*floor((data_2[i]+data_1[i])/2));      //(x+a) - y * floor (x / y)
        }
    return result;
}

vector<float> insert_vector(vector<float>& data_1, vector<float>& data_2){

        data_1.insert(data_1.end(), data_2.begin(), data_2.end());
        return data_1;

}

vector<float> slicing(vector<float>& arr,
```

```
                    int X, int Y)
{

    // Starting and Ending iterators
    auto start = arr.begin() + X;
    auto end = arr.begin() + Y + 1;

    // To store the sliced vector
    vector<float> result(Y - X + 1);

    // Copy vector using copy function()
    copy(start, end, result.begin());

    // Return the final sliced vector
    return result;
}

void insert_row(vector<float>& data, vector<float>& newRow, int loc) {

        for ( int i = 0 ;i != newRow.size(); i++){
           data[loc+i] = newRow[i];

        }

}

int main(){
    vector <int> reliability_seq = {0, 1, 2, 4, 8, 16, 32, 3, 5, 64, 9, 6,
17, 10, 18, 128, 12, 33, 65, 20, 256, 34, 24, 36, 7, 129, 66, 512, 11, 40,
68, 130,
    19, 13, 48, 14, 72, 257, 21, 132, 35, 258, 26, 513, 80, 37, 25, 22,
136, 260, 264, 38, 514, 96, 67, 41, 144, 28, 69, 42,
    516, 49, 74, 272, 160, 520, 288, 528, 192, 544, 70, 44, 131, 81, 50,
73, 15, 320, 133, 52, 23, 134, 384, 76, 137, 82, 56, 27,
    97, 39, 259, 84, 138, 145, 261, 29, 43, 98, 515, 88, 140, 30, 146, 71,
262, 265, 161, 576, 45, 100, 640, 51, 148, 46, 75, 266, 273, 517, 104, 162,
    53, 193, 152, 77, 164, 768, 268, 274, 518, 54, 83, 57, 521, 112, 135,
78, 289, 194, 85, 276, 522, 58, 168, 139, 99, 86, 60, 280, 89, 290, 529,
524,
    196, 141, 101, 147, 176, 142, 530, 321, 31, 200, 90, 545, 292, 322,
532, 263, 149, 102, 105, 304, 296, 163, 92, 47, 267, 385, 546, 324, 208,
386, 150, 153,
    165, 106, 55, 328, 536, 577, 548, 113, 154, 79, 269, 108, 578, 224,
166, 519, 552, 195, 270, 641, 523, 275, 580, 291, 59, 169, 560, 114, 277,
156, 87, 197,
    116, 170, 61, 531, 525, 642, 281, 278, 526, 177, 293, 388, 91, 584,
769, 198, 172, 120, 201, 336, 62, 282, 143, 103, 178, 294, 93, 644, 202,
592, 323, 392,
    297, 770, 107, 180, 151, 209, 284, 648, 94, 204, 298, 400, 608, 352,
325, 533, 155, 210, 305, 547, 300, 109, 184, 534, 537, 115, 167, 225, 326,
306, 772, 157,
    656, 329, 110, 117, 212, 171, 776, 330, 226, 549, 538, 387, 308, 216,
416, 271, 279, 158, 337, 550, 672, 118, 332, 579, 540, 389, 173, 121, 553,
199, 784, 179,
    228, 338, 312, 704, 390, 174, 554, 581, 393, 283, 122, 448, 353, 561,
203, 63, 340, 394, 527, 582, 556, 181, 295, 285, 232, 124, 205, 182, 643,
562, 286, 585,
    299, 354, 211, 401, 185, 396, 344, 586, 645, 593, 535, 240, 206, 95,
327, 564, 800, 402, 356, 307, 301, 417, 213, 568, 832, 588, 186, 646, 404,
227, 896, 594,
```

```
    418, 302, 649, 771, 360, 539, 111, 331, 214, 309, 188, 449, 217, 408,
609, 596, 551, 650, 229, 159, 420, 310, 541, 773, 610, 657, 333, 119 ,600,
339, 218, 368 ,
    652, 230, 391, 313, 450, 542, 334 ,233, 555, 774, 175, 123, 658, 612,
341, 777, 220, 314, 424, 395, 673, 583, 355 ,287, 183,234, 125 ,557 ,660,
616 ,342 ,316 ,
    241, 778, 563, 345, 452, 397, 403, 207, 674, 558, 785, 432, 357, 187,
236, 664, 624, 587, 780, 705, 126, 242, 565, 398, 346, 456, 358, 405 ,303,
569 ,244 ,595 ,
    189, 566, 676, 361, 706, 589, 215, 786, 647, 348, 419, 406, 464, 680,
801, 362, 590, 409, 570, 788, 597, 572, 219, 311, 708, 598, 601, 651 ,421,
792 ,802 ,611 ,
    602, 410, 231, 688, 653, 248, 369, 190, 364, 654, 659, 335, 480, 315,
221, 370, 613, 422, 425, 451, 614, 543, 235, 412, 343, 372, 775, 317 ,222,
426 ,453 ,237 ,
    559, 833, 804, 712, 834, 661, 808, 779, 617, 604, 433, 720, 816, 836,
347, 897, 243, 662, 454, 318, 675, 618, 898, 781, 376, 428, 665, 736 ,567,
840 ,625 ,238 ,
    359, 457, 399, 787, 591, 678, 434, 677, 349, 245, 458, 666, 620, 363,
127, 191, 782, 407, 436, 626, 571, 465, 681, 246, 707, 350, 599, 668 ,790,
460 ,249 ,682 ,
    573, 411, 803, 789, 709, 365, 440, 628, 689, 374, 423, 466, 793, 250,
371, 481, 574, 413, 603, 366, 468, 655, 900, 805, 615, 684, 710, 429 ,794,
252 ,373 ,605 ,
    848, 690, 713, 632, 482, 806, 427, 904, 414, 223, 663, 692, 835, 619,
472, 455, 796, 809, 714, 721, 837, 716, 864, 810, 606, 912, 722, 696 ,377,
435 ,817 ,319,
    621, 812, 484, 430, 838, 667, 488, 239, 378, 459, 622, 627, 437, 380,
818, 461, 496, 669, 679, 724, 841, 629, 351, 467, 438, 737, 251, 462, 442,
441 ,469 ,247,
    683, 842, 738, 899, 670, 783, 849, 820, 728, 928, 791, 367, 901, 630,
685, 844 ,633, 711, 253, 691, 824, 902, 686, 740, 850, 375, 444, 470, 483,
415 ,485 ,905,
    795, 473, 634, 744, 852, 960, 865 ,693 ,797 ,906 ,715, 807, 474, 636,
694, 254, 717, 575, 913, 798, 811, 379, 697, 431, 607, 489, 866, 723, 486,
908, 718, 813,
    476, 856, 839, 725, 698, 914, 752, 868, 819, 814, 439, 929, 490, 623
,671 ,739 ,916 ,463 ,843 ,381 ,497 ,930 ,821 ,726 ,961 ,872 ,492 ,631 ,729
,700 ,443, 741,
    845, 920, 382, 822, 851, 730, 498, 880 ,742, 445, 471, 635 ,932 ,687
,903 ,825 ,500 ,846, 745, 826, 732, 446, 962, 936, 475, 853, 867, 637, 907,
487, 695, 746,
    828, 753, 854, 857, 504, 799, 255, 964, 909, 719, 477, 915, 638, 748
,944 ,869 ,491 ,699 ,754 ,858 ,478 ,968 ,383 ,910 ,815 ,976 ,870 ,917 ,727
,493 ,873 ,701,
    931, 756, 860, 499, 731, 823, 922, 874, 918, 502, 933, 743, 760, 881,
494, 702 ,921 ,501 ,876 ,847, 992, 447, 733, 827, 934, 882, 937, 963, 747,
505, 855 ,924,
    734, 829, 965, 938, 884, 506, 749, 945, 966, 755, 859, 940, 830, 911,
871, 639, 888, 479, 946, 750, 969, 508, 861, 757, 970, 919, 875, 862, 758,
948, 977 ,923,
    972, 761, 877, 952, 495, 703, 935, 978, 883, 762, 503, 925 ,878 ,735,
993, 885, 939, 994, 980, 926 ,764 ,941, 967, 886, 831 ,947, 507, 889, 984,
751, 942, 996,
    971 ,890 ,509 ,949 ,973 ,1000 ,892, 950, 863, 759, 1008, 510, 979, 953,
763, 974, 954, 879, 981, 982, 927, 995, 765, 956 ,887, 985, 997, 986, 943,
891, 998, 766,
    511, 988, 1001, 951, 1002, 893, 975, 894, 1009, 955, 1004, 1010, 957,
983, 958, 987, 1012, 999, 1016, 767, 989, 1003, 990, 1005, 959 ,1011 ,1013,
895, 1006, 1014, 1017, 1018,
    991, 1020, 1007, 1015, 1019, 1021, 1022, 1023};
```

```
    int N = 16; int K = 8; int m =1;
    int n = log2(N);
    vector<float> N_bit(16,0);
    vector<int> data_bits(8);
    vector<int> msg_bits(8);
    vector<float> a,b, result_mod_2,insert_vector_res;

    msg_bits = {0,0,1,1,1,0,0,1};
    data_bits = Data_bits(reliability_seq,N,K);
   for (vector<float>::size_type k = 0; k != data_bits.size(); k++){
       N_bit[data_bits[k]] = msg_bits[k];
   }

   for (int j = 0; j < n; j++){
       for (int l = 0; l< N-1; l = l+2*m){
            a = slicing(N_bit,l,l+m-1);
            b = slicing(N_bit, l+m,l+2*m-1);
            result_mod_2 = Mod_2_addition(a,b);
            result_mod_2.insert(result_mod_2.end(), b.begin(), b.end());
            insert_row(N_bit,result_mod_2,l);
       }
       m = m * 2;

   }
   for (vector<float>::size_type q = 0; q!=N_bit.size(); q++){
       cout<< N_bit[q]<< endl;
   }
}
```

A.2 Polar Decoder

```
#include <iostream>
#include <string>
#include <vector>
#include <cmath>
#include <algorithm>
using namespace std;

vector<float> Mod_2_addition(vector<float>& data_1, vector<float>& data_2)
{
    vector<float> result;
    for (vector<float>::size_type i = 0; i !=data_1.size(); i++){
        result.push_back((data_2[i]+data_1[i])-
2*floor((data_2[i]+data_1[i])/2));
        }
    return result;
}

vector<float> insert_vector(vector<float>& data_1, vector<float>& data_2){
    data_1.insert(data_1.end(), data_2.begin(), data_2.end());
    return data_1;
}

vector<float> f_func(vector<float>& data_1, vector<float>& data_2) {
```

```
    vector<float> result;
    for (vector<float>::size_type i = 0; i !=data_1.size(); i++){
        result.push_back((1-2*(data_1[i]<0))*(1-
2*(data_2[i]<0))*min(abs(data_1[i]),abs(data_2[i])));
        }
    return result;
}

vector<float> g_func(vector<float>& data_1, vector<float>& data_2,
vector<float>& data_3) {
    vector<float> result;
    for (vector<float>::size_type i = 0; i !=data_1.size(); i++){
        result.push_back(data_2[i]+data_1[i]*(1-2*data_3[i]));
        }
    return result;
}

void insert_row_loc(vector<vector<float>>& data, vector<float>& newRow, int
position, int loc) {
    vector<float> tempvec;
    tempvec = data[position];
        for ( int i = 0 ;i != newRow.size(); i++){
            tempvec.insert(tempvec.begin()+loc+i, newRow[i]);
        }
        data[position] = tempvec;
}

vector<float> slicing_2D(vector<vector<float>>& res,
                    int X, int Y, int depth)
{

    // Starting and Ending iterators
    vector<float> arr = res[depth];
    auto start = arr.begin() + X;
    auto end = arr.begin() + Y + 1;

    // To store the sliced vector
    vector<float> result(Y - X + 1);

    // Copy vector using copy function()
    copy(start, end, result.begin());

    // Return the final sliced vector
    return result;


}

 void insert_row(vector<vector<float>>& data, vector<float>& newRow, int
position) {
        for (int loc = 0; loc != newRow.size(); loc++){
            data[position][loc] = newRow[loc];
        }
}

vector <int> frozen_bits(vector<int>& reliability_seq, int N, int K){
    vector<int> result, frozen_bits;
    for (vector<int>::const_iterator iter = reliability_seq.begin(); iter
!= reliability_seq.end(); iter++){
        if ((*iter)<=N-1){
            result.push_back(*iter);
```

```
        }
    }
    for (vector<int>::size_type i = 0; i!= result.size()-K; i++){
        frozen_bits.push_back(result[i]);
    }
    return frozen_bits;
}

vector <int> Data_bits(vector<int>& reliability_seq, int N, int K){
    vector<int> result, data_bits;
    for (vector<int>::const_iterator iter = reliability_seq.begin(); iter
!= reliability_seq.end(); iter++){
        if ((*iter)<=N-1){
            result.push_back(*iter);
        }
    }
    for (vector<int>::size_type i = N-K; i!= result.size(); i++){
        data_bits.push_back(result[i]);
    }
    return data_bits;
}

vector<float> slicing(vector<float>& arr,
                      int X, int Y)
{

    // Starting and Ending iterators
    auto start = arr.begin() + X;
    auto end = arr.begin() + Y + 1;

    // To store the sliced vector
    vector<float> result(Y - X + 1);

    // Copy vector using copy function()
    copy(start, end, result.begin());

    // Return the final sliced vector
    return result;
}


int main(){

   vector <int> reliability_seq = {0, 1, 2, 4, 8, 16, 32, 3, 5, 64, 9, 6,
17, 10, 18, 128, 12, 33, 65, 20, 256, 34, 24, 36, 7, 129, 66, 512, 11, 40,
68, 130,
    19, 13, 48, 14, 72, 257, 21, 132, 35, 258, 26, 513, 80, 37, 25, 22,
136, 260, 264, 38, 514, 96, 67, 41, 144, 28, 69, 42,
    516, 49, 74, 272, 160, 520, 288, 528, 192, 544, 70, 44, 131, 81, 50,
73, 15, 320, 133, 52, 23, 134, 384, 76, 137, 82, 56, 27,
    97, 39, 259, 84, 138, 145, 261, 29, 43, 98, 515, 88, 140, 30, 146, 71,
262, 265, 161, 576, 45, 100, 640, 51, 148, 46, 75, 266, 273, 517, 104, 162,
    53, 193, 152, 77, 164, 768, 268, 274, 518, 54, 83, 57, 521, 112, 135,
78, 289, 194, 85, 276, 522, 58, 168, 139, 99, 86, 60, 280, 89, 290, 529,
524,
    196, 141, 101, 147, 176, 142, 530, 321, 31, 200, 90, 545, 292, 322,
532, 263, 149, 102, 105, 304, 296, 163, 92, 47, 267, 385, 546, 324, 208,
386, 150, 153,
    165, 106, 55, 328, 536, 577, 548, 113, 154, 79, 269, 108, 578, 224,
166, 519, 552, 195, 270, 641, 523, 275, 580, 291, 59, 169, 560, 114, 277,
156, 87, 197,
```

116, 170, 61, 531, 525, 642, 281, 278, 526, 177, 293, 388, 91, 584,
769, 198, 172, 120, 201, 336, 62, 282, 143, 103, 178, 294, 93, 644, 202,
592, 323, 392,
297, 770, 107, 180, 151, 209, 284, 648, 94, 204, 298, 400, 608, 352,
325, 533, 155, 210, 305, 547, 300, 109, 184, 534, 537, 115, 167, 225, 326,
306, 772, 157,
656, 329, 110, 117, 212, 171, 776, 330, 226, 549, 538, 387, 308, 216,
416, 271, 279, 158, 337, 550, 672, 118, 332, 579, 540, 389, 173, 121, 553,
199, 784, 179,
228, 338, 312, 704, 390, 174, 554, 581, 393, 283, 122, 448, 353, 561,
203, 63, 340, 394, 527, 582, 556, 181, 295, 285, 232, 124, 205, 182, 643,
562, 286, 585,
299, 354, 211, 401, 185, 396, 344, 586, 645, 593, 535, 240, 206, 95,
327, 564, 800, 402, 356, 307, 301, 417, 213, 568, 832, 588, 186, 646, 404,
227, 896, 594,
418, 302, 649, 771, 360, 539, 111, 331, 214, 309, 188, 449, 217, 408,
609, 596, 551, 650, 229, 159, 420, 310, 541, 773, 610, 657, 333, 119 ,600,
339, 218, 368 ,
652, 230, 391, 313, 450, 542, 334 ,233, 555, 774, 175, 123, 658, 612,
341, 777, 220, 314, 424, 395, 673, 583, 355 ,287, 183,234, 125 ,557 ,660,
616 ,342 ,316 ,
241, 778, 563, 345, 452, 397, 403, 207, 674, 558, 785, 432, 357, 187,
236, 664, 624, 587, 780, 705, 126, 242, 565, 398, 346, 456, 358, 405 ,303,
569 ,244 ,595 ,
189, 566, 676, 361, 706, 589, 215, 786, 647, 348, 419, 406, 464, 680,
801, 362, 590, 409, 570, 788, 597, 572, 219, 311, 708, 598, 601, 651 ,421,
792 ,802 ,611 ,
602, 410, 231, 688, 653, 248, 369, 190, 364, 654, 659, 335, 480, 315,
221, 370, 613, 422, 425, 451, 614, 543, 235, 412, 343, 372, 775, 317 ,222,
426 ,453 ,237 ,
559, 833, 804, 712, 834, 661, 808, 779, 617, 604, 433, 720, 816, 836,
347, 897, 243, 662, 454, 318, 675, 618, 898, 781, 376, 428, 665, 736 ,567,
840 ,625 ,238 ,
359, 457, 399, 787, 591, 678, 434, 677, 349, 245, 458, 666, 620, 363,
127, 191, 782, 407, 436, 626, 571, 465, 681, 246, 707, 350, 599, 668 ,790,
460 ,249 ,682 ,
573, 411, 803, 789, 709, 365, 440, 628, 689, 374, 423, 466, 793, 250,
371, 481, 574, 413, 603, 366, 468, 655, 900, 805, 615, 684, 710, 429 ,794,
252 ,373 ,605 ,
848, 690, 713, 632, 482, 806, 427, 904, 414, 223, 663, 692, 835, 619,
472, 455, 796, 809, 714, 721, 837, 716, 864, 810, 606, 912, 722, 696 ,377,
435 ,817 ,319,
621, 812, 484, 430, 838, 667, 488, 239, 378, 459, 622, 627, 437, 380,
818, 461, 496, 669, 679, 724, 841, 629, 351, 467, 438, 737, 251, 462, 442,
441 ,469 ,247,
683, 842, 738, 899, 670, 783, 849, 820, 728, 928, 791, 367, 901, 630,
685, 844 ,633, 711, 253, 691, 824, 902, 686, 740, 850, 375, 444, 470, 483,
415 ,485 ,905,
795, 473, 634, 744, 852, 960, 865 ,693 ,797 ,906 ,715, 807, 474, 636,
694, 254, 717, 575, 913, 798, 811, 379, 697, 431, 607, 489, 866, 723, 486,
908, 718, 813,
476, 856, 839, 725, 698, 914, 752, 868, 819, 814, 439, 929, 490, 623
,671 ,739 ,916 ,463 ,843 ,381 ,497 ,930 ,821 ,726 ,961 ,872 ,492 ,631 ,729
,700 ,443, 741,
845, 920, 382, 822, 851, 730, 498, 880 ,742, 445, 471, 635 ,932 ,687
,903 ,825 ,500 ,846, 745, 826, 732, 446, 962, 936, 475, 853, 867, 637, 907,
487, 695, 746,
828, 753, 854, 857, 504, 799, 255, 964, 909, 719, 477, 915, 638, 748
,944 ,869 ,491 ,699 ,754 ,858 ,478 ,968 ,383 ,910 ,815 ,976 ,870 ,917 ,727
,493 ,873 ,701,

```
    931, 756, 860, 499, 731, 823, 922, 874, 918, 502, 933, 743, 760, 881,
494, 702 ,921 ,501 ,876 ,847, 992, 447, 733, 827, 934, 882, 937, 963, 747,
505, 855 ,924,
    734, 829, 965, 938, 884, 506, 749, 945, 966, 755, 859, 940, 830, 911,
871, 639, 888, 479, 946, 750, 969, 508, 861, 757, 970, 919, 875, 862, 758,
948, 977 ,923,
    972, 761, 877, 952, 495, 703, 935, 978, 883, 762, 503, 925 ,878 ,735,
993, 885, 939, 994, 980, 926 ,764 ,941, 967, 886, 831 ,947, 507, 889, 984,
751, 942, 996,
    971 ,890 ,509 ,949 ,973 ,1000 ,892, 950, 863, 759, 1008, 510, 979, 953,
763, 974, 954, 879, 981, 982, 927, 995, 765, 956 ,887, 985, 997, 986, 943,
891, 998, 766,
    511, 988, 1001, 951, 1002, 893, 975, 894, 1009, 955, 1004, 1010, 957,
983, 958, 987, 1012, 999, 1016, 767, 989, 1003, 990, 1005, 959 ,1011 ,1013,
895, 1006, 1014, 1017, 1018,
    991, 1020, 1007, 1015, 1019, 1021, 1022, 1023};

   // declaration
   int N = 16; int npos=0; int K = 8; int n = log2(N); int temp =0;
   int Left_temp =0; int Left_node = 0; int Left_depth = 0;
   int Cen_temp =0; int Cen_node = 0; int Cen_depth = 0;
   int Right_node = 0;
   int node = 0; int depth = 0; int done = 0;
   vector<int>::iterator iter;
   vector<int> ns(2*N-2);
   vector<int> frozen, data_bit;
   vector<float> received_bits = {-1.4,0.94,-1.76, -0.5, -1.68, -1.73, -
0.89, -0.24, 0.25, -1.48, 1.628, 1.329, 0.87095, 1.25, 0.84, 0.08 };
   vector<float> LLRn ;
   vector<float> a,b, Lvec,Rvec;
   vector<vector<float>> LLR (n+1, vector<float> (N));
   vector<vector<float>> ucap (n+1, vector<float> (N));
   vector<float> ucapn, ucapl, ucapr, mod_2_addition_res,
Insert_vector_res,msg_cap,Final_op(K);


   fill(ns.begin(),ns.end(),0);
   insert_row(LLR,received_bits,0); // incoming beliefs
   frozen = frozen_bits(reliability_seq, N, K);

   while (done == 0){
       if (depth == n){
           iter = find(frozen.begin(), frozen.end(),node);
           if (iter != frozen.end()){
               ucap[n][node] = 0;
           }
           else{
               if (LLR[n][node]>=0){
                   ucap[n][node]=0;
               }
               else{
                   ucap[n][node]=1;
               }
           }
           if (node == N-1){
               done = 1;
           }
           else{
               node = floor(node/2); depth = depth -1;
           }
       }
```

```
        else{

            npos = pow(2,depth)-1+node ;
            if (ns[npos]==0){
                temp = pow(2,n-depth);
                LLRn =  slicing_2D(LLR,temp*node,temp*(node+1)-1,depth);
                a = slicing(LLRn,0,temp/2 -1);
                b = slicing(LLRn, temp/2, temp-1);
                node = node*2; depth = depth +1; temp = temp/2;
                Lvec = f_func(a,b);
                insert_row_loc(LLR,Lvec,depth,temp*node);
                ns[npos] = 1;
            }
            else{
                if (ns[npos] == 1){
                    temp = pow(2,n-depth);
                    LLRn =  slicing_2D(LLR,temp*node,temp*(node+1)-1,depth);
                    a = slicing(LLRn,0,temp/2 -1);
                    b = slicing(LLRn, temp/2, temp-1);
                    Left_node = node*2; Left_depth = depth +1; Left_temp =
temp/2;
                    ucapn = slicing_2D(ucap,Left_temp*Left_node,
Left_temp*(Left_node+1)-1, Left_depth);
                    node = node*2+1; depth = depth +1; temp = temp/2;
                    Rvec = g_func(a,b,ucapn);
                    insert_row_loc(LLR,Rvec,depth,temp*node);
                    ns[npos]=2;
                }
                else{
                    temp = pow(2,n-depth);
                    Left_node = 2*node; Right_node = 2*node +1; Cen_depth =
depth +1;
                    Cen_temp = temp/2;
                    ucapl = slicing_2D(ucap,Cen_temp*Left_node,
Cen_temp*(Left_node+1)-1, Cen_depth);
                    ucapr = slicing_2D(ucap,Cen_temp*Right_node,
Cen_temp*(Right_node+1)-1, Cen_depth);
                    mod_2_addition_res = Mod_2_addition(ucapl,ucapr);
                    Insert_vector_res =
insert_vector(mod_2_addition_res,ucapr);
                    insert_row_loc(ucap, Insert_vector_res,
depth,temp*node);
                    node = floor(node/2); depth = depth -1;
                }
            }


        }
    }
    //final estimated codeword here;
    msg_cap = ucap[n];
    data_bit = Data_bits(reliability_seq,N,K);
    for (vector<float>::size_type k = 0; k != data_bit.size(); k++){
        Final_op[k] = msg_cap[data_bit[k]];
        cout<< Final_op[k]<<endl;
    }
}
```

Appendix B: Ryu-Controller Handover Mechanism

```
from ryu.base import app_manager
from ryu.controller import ofp_event
from ryu.controller.handler import CONFIG_DISPATCHER, MAIN_DISPATCHER
from ryu.controller.handler import set_ev_cls
from ryu.ofproto import ofproto_v1_4
from ryu.lib.packet import packet
from ryu.lib.packet import ethernet
from ryu.lib.packet import ether_types
from utils import *
from ryu.controller import dpset

class Handover(app_manager.RyuApp):
    OFP_VERSIONS = [ofproto_v1_4.OFP_VERSION]
    _CONTEXTS = {
                'dpset': dpset.DPSet,
            }

    def __init__(self, *args, **kwargs):
        super(SimpleSwitch14, self).__init__(*args, **kwargs)
        self.mac_to_port = {}
        self.dpset = kwargs['dpset']
        self.dp = []
        self.dat_path = []
        self.dpid = None
        self.change = 0
        self.actions = []

    @set_ev_cls(ofp_event.EventOFPSwitchFeatures, CONFIG_DISPATCHER)
    def switch_features_handler(self, ev):
        datapath = ev.msg.datapath
        ofproto = datapath.ofproto
        parser = datapath.ofproto_parser

        # install table-miss flow entry
        #
        # We specify NO BUFFER to max_len of the output action due to
        # OVS bug. At this moment, if we specify a lesser number, e.g.,
        # 128, OVS will send Packet-In with invalid buffer_id and
        # truncated packet data. In that case, we cannot output packets
        # correctly.  The bug has been fixed in OVS v2.1.0.
        match = parser.OFPMatch()
        actions = [parser.OFPActionOutput(ofproto.OFPP_CONTROLLER,
                                          ofproto.OFPCML_NO_BUFFER)]
        self.add_flow(datapath, 0, match, actions)

    def add_flow(self, datapath, priority, match, actions):
        ofproto = datapath.ofproto
        parser = datapath.ofproto_parser

        inst = [parser.OFPInstructionActions(ofproto.OFPIT_APPLY_ACTIONS,
                                             actions)]

        mod = parser.OFPFlowMod(datapath=datapath, priority=priority,
                                match=match, instructions=inst)
        datapath.send_msg(mod)
```

```
    @set_ev_cls(ofp_event.EventOFPPacketIn, MAIN_DISPATCHER)
    def _packet_in_handler(self, ev):
        msg = ev.msg
        datapath = msg.datapath
        ofproto = datapath.ofproto
        parser = datapath.ofproto_parser
        in_port = msg.match['in_port']
        self.dp = self.dpset.get_all()
        pkt = packet.Packet(msg.data)
        eth = pkt.get_protocols(ethernet.ethernet)[0]

        if eth.ethertype == ether_types.ETH_TYPE_LLDP:
            # ignore lldp packet
            return
        dst = eth.dst
        src = eth.src

        self.dpid = datapath.id
        self.mac_to_port.setdefault(self.dpid, {})

        self.logger.info("packet in %s %s %s", self.dp, self.dat_path, dst)
        if (self.dp[0][0] == 17) and (len(self.dp)==3) and
(len(self.dat_path)!=2):
            self.dat_path.append(self.dp[0][1])
            self.dat_path.append(self.dp[1][1])
        elif (len(self.dp)==3) and (len(self.dat_path)!=2):
            self.dat_path.append(self.dp[1][1])
            self.dat_path.append(self.dp[0][1])
        else:
            pass

        # learn a mac address to avoid FLOOD next time.
        if self.change == 0:

self.logger.info("&&&&&&&&&&&&&&&&&&&&&&&&&&&&&&&&&&&&&&&&&&&&&&&&&&&&&&&&
&&&&&&&&")
            self.mac_to_port[self.dpid][src] = in_port

            if dst in self.mac_to_port[self.dpid]:
                out_port = self.mac_to_port[self.dpid][dst]
            else:
                out_port = ofproto.OFPP_FLOOD
            if self.dpid == 17:
                self.actions = [parser.OFPActionOutput(out_port)]
            else:
                self.actions = [parser.OFPActionOutput(out_port)]

            # install a flow to avoid packet_in next time
            if out_port != ofproto.OFPP_FLOOD:
                match = parser.OFPMatch(in_port=in_port, eth_dst=dst,
eth_src=src)
                self.add_flow(datapath, 1, match, self.actions)

        elif (self.change == 1):

self.logger.info("
_____________________")

            match1 = parser.OFPMatch(in_port=3,
eth_dst='98:40:bb:37:17:b7', eth_src='e4:5f:01:5f:03:bf')
```

```
            match2 = parser.OFPMatch(in_port=1,
eth_src='98:40:bb:37:17:b7', eth_dst='e4:5f:01:5f:03:bf')


#_____________________________RPi2_____________________________________________
_____________________

            match3 = parser.OFPMatch(in_port=1,
eth_dst='98:40:bb:37:17:b7', eth_src='e4:5f:01:5f:03:bf')
            match4 = parser.OFPMatch(in_port=2,
eth_src='98:40:bb:37:17:b7', eth_dst='e4:5f:01:5f:03:bf')


            actions1 = [parser.OFPActionOutput(1)]
            actions2 = [parser.OFPActionOutput(2)]
            actions3 = [parser.OFPActionOutput(3)]


            self.add_flow(self.dat_path[0], 300, match1, actions1)
            self.add_flow(self.dat_path[0], 300, match2, actions3)
            self.add_flow(self.dat_path[1], 300, match3, actions2)
            self.add_flow(self.dat_path[1], 300, match4, actions1)

        else:
            return

        data = None
        if msg.buffer_id == ofproto.OFP_NO_BUFFER:
            data = msg.data

        out = parser.OFPPacketOut(datapath=datapath,
buffer_id=msg.buffer_id,
                                  in_port=in_port, actions=self.actions,
data=data)
        datapath.send_msg(out)

    @set_ev_cls(ofp_event.EventOFPPortStatus, MAIN_DISPATCHER)
    def _port_status_handler(self, ev):
        msg = ev.msg
        reason = msg.reason
        port_no = msg.desc.port_no

        ofproto = msg.datapath.ofproto
        if reason == ofproto.OFPPR_ADD:
            self.logger.info("connection established %s", port_no)
        elif reason == ofproto.OFPPR_DELETE:
            self.logger.info("disconnected %s", port_no)
        elif (reason == ofproto.OFPPR_MODIFY):
            if (port_no == 2): #here it is
                self.logger.info("port modified %s", port_no)
                self.change =1
            else:
                self.logger.info("PORT")
        else:
            self.logger.info("Illeagal port state %s %s", port_no, reason)
```